Universitat Autònoma de Barcelona

FUNCTIONALIZED ADSORBENT MATERIALS USING SUPERCRITICAL CO_2

Ph.D. program in Materials Science

A dissertation submitted in partial fulfillment of the requirements
for the degree of
DOCTOR OF PHILOSOPHY

In the Deparment of Physics at the
UNIVERSITAT AUTONMA DE BARCELONA

Pedro López-Aranguren Oliver

MATGAS ICMAB

Summary

Historically, porous silica (SiO_2) is one of the most used adsorbents for a wide variety of processes in the industry. However, the fast grown on the demand of new nanotechnology based materials and sustainable green processes have made necessary the development of adsorbents with improved physico-chemical properties. One of the most applied options to modify porous silica is the incorporation on the surface of organic functional molecules, giving place to hybrid materials, in which the properties of both components are combined. In this doctoral thesis, supercritical carbon dioxide ($scCO_2$) has been used as the solvent to carry out the functionalization processes. Carbon dioxide is a sustainable solvent and its use has been preferred in front of toxic organic liquid solvents, often applied in the traditional methods of synthesis. Amorphous silica matrices with structural ordered pores (MCM-41, 4 nm) and disordered pores (silica gel, 4-9 nm) were selected for the functionalization processes. Besides, the properties conferred by functionalization to microporous crystaline zeolites have been preliminary studied. The modifying agents applied in this thesis were either alkyl (octyltriethoxysialane) or amino (methylaminopropyltrimethoxisilane) silane and aziridine. The later compound is a monomer which polymerizes in presence of CO_2, leading to hyperbranched polyethyleneimine (PEI) with multiple amino groups formed into the silica pores. This novel method only requires compressed CO_2 as the reagent and the catalyst of the polymerization reaction of aziridine, which usually requires the use of organic solvents, a solid catalyst, high temperatures and long processing times. The functionalization of porous silica with aminosilane in $scCO_2$ is more complex than the case of alkysilanes due to the high reactivity between amino groups and CO_2 to form unsoluble carabamate species. However, in this study a protocol was designed to partially inhibit carabamate formation by controlling the pressure and temperature of the reaction media. The obtained materials were characterized using solid state characterization tools: low temperature N_2 and CO_2 adsorption, thermal analysis, infrared spectroscopy and X-Ray diffraction. Moreover, modeling and simulation

methods were used as complementary tools that allowed the study of this complex systems with a high level of detail. The alkyl chain of the alkylsilane induced to the porous system a hydrophobic behavior, hence, obtaining materials candidates for oil adsorption. The functionalization with organic molecules containing the amino group allowed the preparation of materials for the adsorption and separation of CO_2 from diluted gases (CO_2 sequestration). The CO_2 adsorption properties of the synthesized aminosilicas were evaluated combining experimental adsorption tools with molecular simulations. The characterization of these materials was based on the evaluation of the overall CO_2 adsorption capacity and the influence of the temperature, the selectivity of the CO_2 adsorption in gas mixtures, the stability in the cyclic adsorption/desorption process and the kinetics, which were determined by performing both microbalance and CO_2 adsorption isotherms at different temperatures.

Table of contents

Symbols

d_s	Deposited silane ($g_s\ g^{-1}$)
g_s	Grafted molecules (g)
k	Boltzmann's constant
M_w	Molecular weight
n	Molecule density in lattice gas
p	Density of particles in porous matrix
P	Pressure (Pa)
P_c	Critical pressure (Pa)
P_r	Reduced pressure
P/P_0	Relative pressure
P_d	Pore diameter (nm)
S_a	Surface area ($m^2\ g^{-1}$)
T	Temperature (ºC)
T_g	Glass transition temperature (ºC)
T_c	Critical temperature (ºC)
T_r	Reduced temperature
V_p	Pore volume ($cm^3\ g^{-1}$)
V_{mp}	Micropore volume
z	Lattice coordination number

Greek letters

Φ	Scaling factor
ρ_{OH}	Hydroxyl density (OH nm^{-2})
ρ_{graft}	Grafting density (molec nm^{-2})
β	1/kT
μ	Chemical potential
Γ	Fluid-solid coupling parameter in lattice gas
$\mathfrak{J}$	Nearest neighbor coupling parameter
ρ	Density

Subscripts

c	Critical property

Superscripts

‘	Dimensionless property

Abbreviations and acronyms

BET	Brunauer-Emmett-Teller
BJH	Barret Joyner and Halenda
CC	Clean Cat
CDCB	Couple-Decoupled Configurational Bias
CNT	Carbon Nanotube
COF	Covalent Organic Framework
EA	Elemental Analysis
Et	Ethanol
Eth	Diethyl ether
FTIR	Fourier Transform Infrared
GAS	Gas Anti-Solvent
GMC	Grand Canonical Monte Carlo
GWP	Global Warming Potential
HTSCD	High Temperature Supercritical Drying
IR	Infrared
KF	Karl-Fischer
LTSCD	Low Temperature Supercritical Drying
MALDI Tof	Matrix-Assisted Laser Desorption/Ionization
MCM	Mobil Composition of Matter (type of mesoporous silica)

Me	Methanol
MIP	Mercury Intrusion Porosimetry
MMS	Mesoporous molecular Sieve
MOF	Metal Organic Framework
MWCN	Multi Walled Carbon Nanotube
OMS	Ordered Mesoporous Silica
PEI	Polyethyleneimine
PCA	Precipitation with a Compressed Antisolvent
PGSS	Particles from Gas Saturated Solutions
PID	Proportional Integral Derivative Controller
RESS	Rapid Expansion of Supercritical Solutions
SAS	Supercriticial Anti-solvent
SB	Silica Blue
SBA	Santa Barbara Amorphous (type of mesoporous silica)
$ScCO_2$	Supercritical Carbon Dioxide
SCF	Supercritical Fluid
SG_{40}	Silica Gel 40
SWCN	Single Walled Carbon Nanotube
TEM	Transmision Electronic Microscopy
TEOS	Tetraethyl orthosilicate
TGA	Thermogravimetric Analysis

TMOS	Tetramethylorthosilicate
XRD	X-ray diffraction
ZSM	Zeolite Socony Mobil
ZY	Zeolite Y

INTRODUCTION

The focus of this thesis is the synthesis and characterization of organic-inorganic porous materials for adsorption applications. For this purpose, porous silica were used as the inorganic host substrates to be modified with organic functional molecules using a new procedure for the functionalization. The impregnation of organic functional groups into porous systems leads to a final products with interesting properties that can be used in diverse processes, such as catalysis [1], adsorption [2, 3], separation [4], drug delivery [5] and to develop sensors [6].

Common routes to graft organic functional groups on the internal surface of porous silica are based on the use of organic solvents that are highly pollutant. Thus, one of the main goals of this thesis, based on the search of new and alternative synthesis processes, is the use of supercritical CO_2 ($scCO_2$) as a green technology to prepare functionalized porous sorbents. Since the discovery of supercritical fluids in 1822 by Baron Charles Cagniard, this technology has been used to replace some conventional solvents applied in the manufacturing of different materials by $scCO_2$. For instance, the extraction of caffeine from coffee [7], one of the most consumed beverages in the world, or the recent use of $scCO_2$ to extract trichloroanisole from cork stoppers [8], a non desired molecule in the wine industry, gives us an idea of the importance of the use of supercritical CO_2 as an industrial solvent.

In this thesis, supercritical CO_2 has been used as the solvent media to modify porous silica with alkylsilanes in order to prepare hydrophobic sorbents; and with aminosilanes and aminopolymers to develop materials for CO_2 adsorption applications. The use of solid sorbents for CO_2 adsorption and separation processes arises as a potential solution to mitigate the rapid increase of the CO_2 concentration in the atmosphere, negatively influencing the global climate change [9]. In order to slow this increase, great efforts are being done to reduce the anthropogenic CO_2 emissions. Large emission point sources, such as fossil-fuel-based power generation facilities are the first targets [10, 11]. In addition, CO_2 is also separated and purified for other several industrial applications, and the process to be used for this separation depends on the source and the final application. The materials

applied for CO_2 adsorption and separation can be classified depending on their way to incorporate CO_2

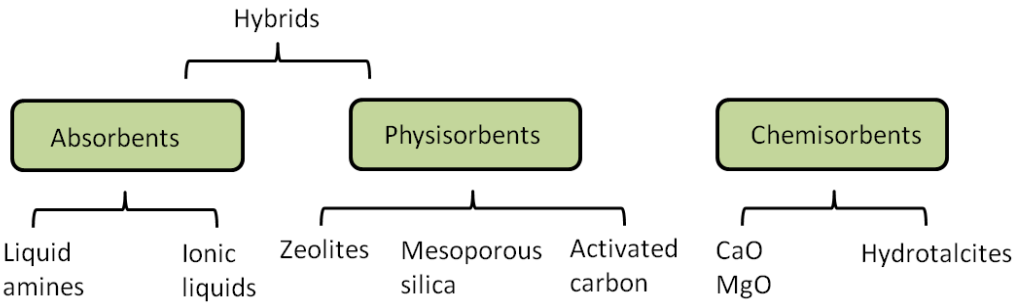

Figure 1.1 Common CO_2 sorbents.

Ideally, a good CO_2 sorbent should exhibit a fast sorption and desorption kinetics, a large sorption capacity, an infinite regenerability and stability. Aqueous amines are amongst the most used materials applied at an industrial scale. Primary and secondary amines can react directly with CO_2 to produce carbamates through the formation of zwitterionic intermediates. The CO_2 is released upon heating the carbamate. The use of aqueous amines entails problems related to the great energy required to desorb the molecule due to the high heat of adsorption of water, the energy needed to break the strong bond formed between CO_2 and the amine that causes losses due to amine volatility, oxidative degradation and stability problems [11]. Hybrid aminosilica materials are a class of sorbents merged to overcome some of the problems related to the use of aqueous amines. The immobilization of aminosilanes on the internal surface of porous silica has several advantages, such as the less energy required to release the captured CO_2 and a better thermal stability [12].

THESIS GOALS

This PhD thesis has the following scientific goals:

- To develop a generic $scCO_2$ process for the surface functionalization of meso- and microporous silica with organic functional molecules, in order to improve or modify their properties as sorbents.
- To obtain quality sorbents, i.e. with a homogenous distribution of the impregnated organic molecules and with a high thermal stability, exhibiting: (i) hydrophobic properties by functionalization with alkylsilanes, and (ii) CO_2 adsorption properties by functionalization with aminosilanes and aminopolymers.
- To study the behavior of amino compounds in $scCO_2$ in order to overcome the formation of insoluble species by controlling the operating conditions of pressure, temperature and the use of co-solvents.
- To demonstrate that $scCO_2$ is an advantageous and effective alternative to liquid organic methods for the preparation of organic-inorganic porous materials.
- To study the physicochemical properties and the improvement of the modified sorbents with respect to bare materials in their adsorption of H_2O, N_2 and CO_2.
- To obtain quantitative predictions of the adsorption of gases on functionalized silicas and to provide new insights in the adsorption mechanisms through the use of molecular simulations
- To predict thermodynamic properties of bulk- and single component adsorption systems through the use of an equation of state.

The following technical achievements were reached to meet the above mentioned objectives:

- Engineering of flexible bench-scale facilities for batch production using $scCO_2$ as a solvent and reaction media.
- Engineering of high pressure instrumentation for organic compounds phase equilibria and solubility behavior in $scCO_2$.
- Development of protocols for designing and evaluating the surface modification processes using $scCO_2$ as the reaction media.

- Development of protocols and methods for off-situ materials characterization: infrared spectroscopy, thermogravimetric analysis, differential scanning calorimetry, Karl-Fischer tritation method for water determination, low-temperature N_2 adsorption/desorption, CO_2 adsorption measurements at a wide range of temperatures, microbalance measurements for cyclic CO_2 adsorption/desorption under a gas mixture, X-ray diffraction, MALDI ToF and static light scattering.
- Development of theoretical structural models of the porous systems using atomistic procedures (f.i. hard-sphere model, LJ interactions).
- Development of the simulation tools based on the Monte Carlo method and using the grand canonical ensemble for the carbonation reaction.
- Establishing the theoretical transformation steps required to transform the model parameters of the mean field equation of state into real parameters of the fluid of interest.

OUTLINE OF THIS THESIS

This brief introduction aims at establishing the contents and the main goals that the reader will find throughout this thesis. In the next chapters, the following contents are developed:

Chapter I - Porous materials, contains a classification of the porous mater and a short description of their chemical composition, synthesis methods and applications. This chapter has a special focus in porous silica and in the selected porous systems used in this work. Relevant information of their textural properties is also given.

Chapter II - Supercritical CO_2: properties, applications and high pressure techonology, describes the thermophysical properties of supercritical CO_2 and the advantages of using it in chemical processes. It also presents the study of the thermodynamic properties of supercritical CO_2 confined in porous media by using a mean field equation of state. The equipment building materials and the elements required to set up a supercritical fluid process are depicted. A detailed description of the equipment and the different configurations used in this work is provided in this chapter.

Chapter III - Functionalization of porous substrates using supercritical CO_2, offers an initial description of the solid state characterization tools used to evaluate the general characteristics of the porous substrates. The experimental functionalization procedures are also described, giving the essential information of the working operation conditions and the experimental set up. In each section, characterization results confirming the presence of organic moieties after the functionalization and the textural properties of the processed porous substrate are given for the different materials prepared.

Chapter IV, Adsorption properties, is focused on the experimental characterization of the synthesized materials from the application point of view i.e. hydrophobicity, water uptake and CO_2 adsorption. A special attention is given in this chapter to the materials designed for CO_2 adsorption properties, comparing the data with simulation results. Data related to prepared products adsorption capacity, the effect of temperature on the adsorption, the efficiency, the rates of adsorption and cyclic adsorption/desorption behavior under a mixture of gases are shown. Molecular simulations are used to obtain relevant information on the adsorption properties of the porous systems. A wide comparison of the adsorption properties of the materials synthesized in this work and the materials from the literature obtained using more conventional synthesis procedures is finally offered in this chapter.

Chapter V, Conclusions and future work, provides the general conclusions of this thesis and the research lines that have been opened to continue with further research.

REFERENCES

1. A.P. Wight and M.E. Davis, *Design and Preparation of Organic−Inorganic Hybrid Catalysts.* Chemical Reviews, 2002, 102(10), 3589.
2. J. Evans, A.B. Zaki, M.Y. El-Sheikh, and S.A. El-Safty, *Incorporation of Transition-Metal Complexes in Functionalized Mesoporous Silica and Their Activity toward the Oxidation of Aromatic Amines.* The Journal of Physical Chemistry B, 2000, 104(44), 10271.
3. R. Voss, A. Thomas, M. Antonietti, and G.A. Ozin, *Synthesis and characterization of highly amine functionalized mesoporous organosilicas by an "all-in-one" approach.* Journal of Materials Chemistry, 2005, 15(37), 4010.
4. S. Yoo, J.D. Lunn, S. Gonzalez, J.A. Ristich, E.E. Simanek, and D.F. Shantz, *Engineering Nanospaces: OMS/Dendrimer Hybrids Possessing Controllable Chemistry and Porosity.* Chemistry of Materials, 2006, 18(13), 2935.
5. M. Vallet-Regí, M. Colilla, and B. González, *Medical applications of organic-inorganic hybrid materials within the field of silica-based bioceramics.* Chemical Society Reviews, 2011, 40(2), 596.
6. S. Wang, Y. Kang, L. Wang, H. Zhang, Y. Wang, and Y. Wang, *Organic/inorganic hybrid sensors: A review.* Sensors and Actuators B: Chemical, 2013, 182(0), 467.
7. H. Peker, M.P. Srinivasan, J.M. Smith, and B.J. Mccoy, *Caffeine extraction rates from coffee beans with supercritical carbon dioxide.* AIChE Journal, 1992, 38(5), 761.
8. M.K. Taylor, T.M. Young, C.E. Butzke, and S.E. Ebeler, *Supercritical fluid extraction of 2,4,6-trichloroanisole from cork stoppers.* Journal of Agricultural and Food Chemistry, 2000, 48(6), 2208.
9. Ipcc, *Climate change 2007: synthesis report. COntribution of Working Groups I, II and III to the Fourth Assesment Report of Intergovernmental Panel on Climate Change*, 2007: Geneva, Szwitzerland.
10. Ipcc, *Carbon Dioxide Capture and Storage vol I and II*, B.M.O.D.H.d.C.M.L.L. Meyer, Editor 2005: USA.
11. M.E. Boot-Handford, J.C. Abanades, E.J. Anthony, M.J. Blunt, S. Brandani, N. Mac Dowell, J.R. Fernandez, M.-C. Ferrari, R. Gross, J.P. Hallett, R.S. Haszeldine, P. Heptonstall, A. Lyngfelt, Z. Makuch, E. Mangano, R.T.J. Porter, M. Pourkashanian, G.T. Rochelle, N. Shah, J.G. Yao, and P.S. Fennell, *Carbon capture and storage update.* Energy & Environmental Science, 2014, 7(1), 130.
12. S. Choi, J.H. Drese, and C.W. Jones, *Adsorbent Materials for Carbon Dioxide Capture from Large Anthropogenic Point Sources.* ChemSusChem, 2009, 2(9), 796.

CHAPTER I

POROUS MATERIALS

This chapter reviews the family of porous materials, including their main properties, design and synthesis, and applications. In the first sections the main concepts of porous materials and the methods to obtain porous materials, with an special focus in the templating method, are described. Porous materials have been classified into three groups according to their chemical composition. The first group, the organic porous materials comprises covalent organic frameworks and porous polymers. The second group corresponds to the large family of inorganic porous materials, which includes carbon materials, silica, silicates and other minerals. Finally, the last group is formed by the organic-inorganic porous materials which have been classified by their synthesis method into metal organic frameworks and functionalized substrates. The bench of porous materias used in this work, belonging to the categories of silica and silicates, either pristine or functionalized, are described in detail in the last section.

1.1 INTRODUCTION TO POROUS MATERIALS

A porous material is a solid with pores, i.e., cavities, channels or interstices, which are deeper than they are wide [1]. Pores are classified according to their availability to an external fluid (Fig. 1.1a), to their size size or to the chemical composition.

- Availability to external fluid:
  - Open pores, those with a continuous channel of communication with the external surface of the solid. They can be open at two ends (through pores *(i)*) or only at one end (blind pores *(ii)*).
  - Closed pores, those totally isolated from their neighbors *(iii)*.
- Shape:

Pores can also be classified according to their shape (Fig. 1.1b) into (*i)* cylindrical, (*ii)* slit, (*iii)* ink bottle, (*iv)* funnel shaped and *(v)* irregular.

Two important features are commonly considered in the classification of porous matter, the pore size and the chemical composition of the network material. Both parameters significantly influence the physicochemical behavior of porous materials in different industrial applications, such as sorption, catalysis, molecular sievin g or membrane separation.

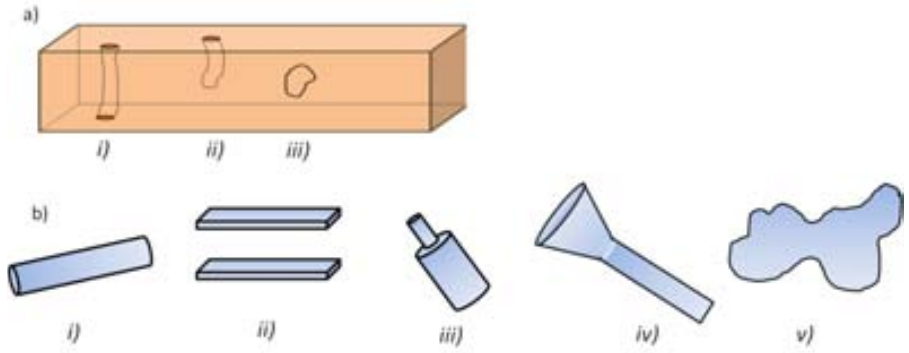

Figure 1.1 Classification of pores according to: a) the pore openning, being *(i,ii)* open pores and *(iii)* closed pores, and b) the pore shape, including *(i)* cylindrical, *(ii)* slit, *(iii)* ink bottle, *(iv)* funnel shapped and *(v)* irregular pores.

- Pore size:

The classification of th e po res according t o th eir diameter is established by t he International Union of Pure and Applied Chemistry (IUPAC) [2]:

- Micropores: pores smaller than 2 nm.
- Mesopores: pores between 2 and 50 nm.
- Macropores: pores larger than 50 nm.

Most porous materiales have po res involving several of the above mentioned pore diameter r anges. An add itional representative characteristic of porous materials is the porosity, defined as the ratio of the empty pore volume to the total volume of the solid.

- Chemical composition of the network:

Porous materials can be organic, inorganic or hybrid organic-inorganic (Fig. 1.2).

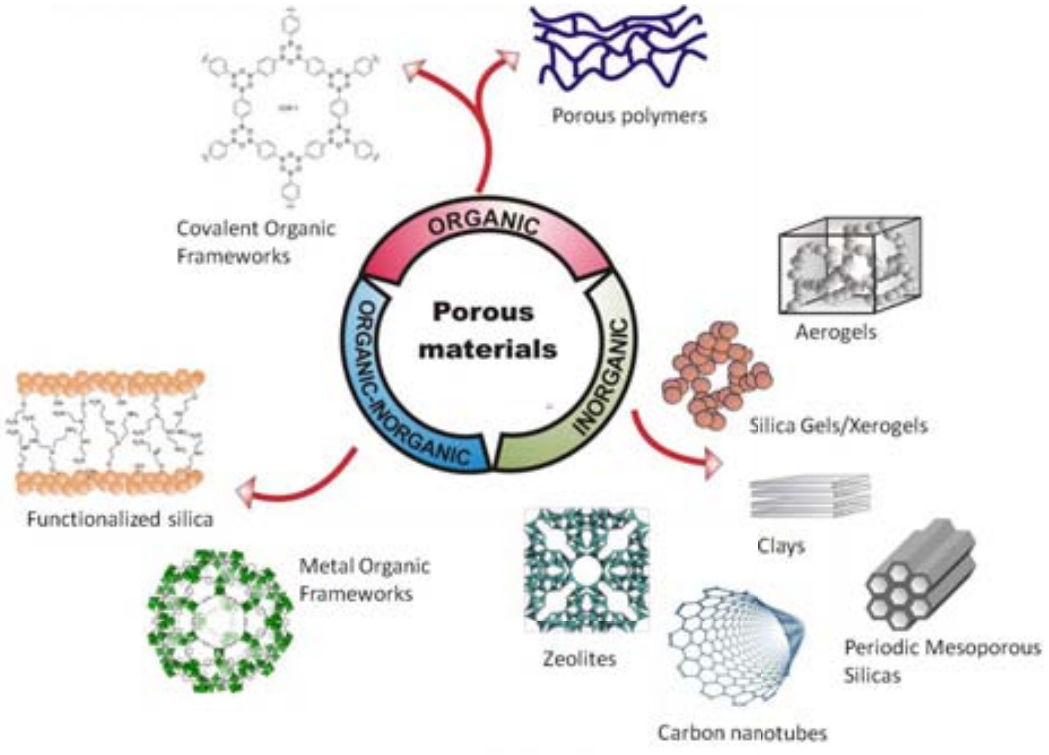

Figure 1.2 Examples of porous materials class ified by their network composition in o rganic, inorganic and hybrid organic-inorganic.

- Important groups of materials from the organic class are covalent organic frameworks and porous polymers [3].
- The inorganic type is the broadest class of porous matter and includes zeolites, microporous carbons, clay minerals, the large family of micro and mesoporous silicas, etc [4].
- The organic-inorganic porous hybrids comprise metal organic frameworks and functionalized inorganic porous materials as most respresentative family members [5].

1.2. METHODS TO CREATE PORES

Several routes have been designed to prepare porous materials, such as the sol-gel technique, the foaming and templating procedures, the direct synthesis or the Schiff-base chemistry [4]. The sol-gel process is a method commonly used to produce porous solid materials from alkoxides, particularly for the fabrication of oxides of silicon and titanium. This procedure will be further described in the section dedicated to porous silica products.

The templating-fabrication strategy is the most widely used method, due to its applicability to process a large variety of different porous network compositions with a wide range of pore size and well-defined pore morphologies [6]. The templating concept is based on the condensation of the end product precursors on the surface of a template that is later removed, thus, forming the void space of the porous material (Fig. 1.3). The pores created have a shape and size similar to the template used. Some common templates are organic molecules, micelles formed by surfactants and inorganic porous materials. The template fabrication method is applied to the synthesis of zeolites and zeolitic products (materials with a zeolite-type framework structure), ordered mesoporous silica materials, porous carbons and porous polymers.

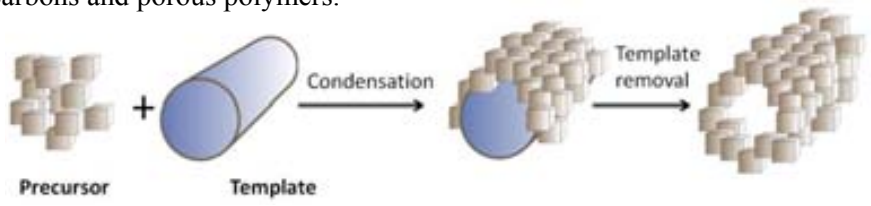

Figure 1.3 Scheme of the templating method. The end product precursor condensates around the template and, then, the template is removed by either calcination or solvent extraction.

1.3 ORGANIC POROUS MATERIALS

1.3.1 Covalent organic frameworks

Covalent organic frameworks (COFs) are 2D or 3D crystalline compounds, entirely composed by light elements (H, B, C, N and O), and constructed by assembling organic building units *via* covalent bonds [3, 7]. The building units are rigid organic fragments, most of them boronic acids and catechols. Fig. 1.4 shows an example of the building units used to fabricate a 2D hexagonal COF.

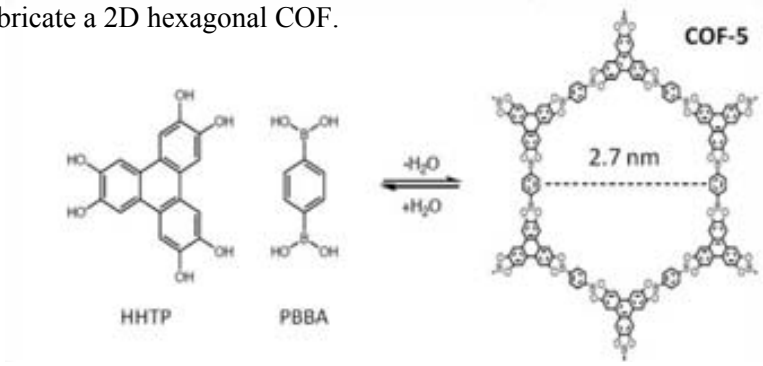

Figure 1.4 Example of a hexagonal 2D COF (COF-5) prepared using a solvothermal condensation reaction between PBBA (a compound composed of a benzene ring with two boronic acid groups) and HHTP (a flat trigonal building block composed of four fused benzene rings with two OH groups at each corner) [7].

The wide variety of structural configurations existing for the building fragments offers a enormous versatility to tune the pores and functionalities of COFs. COFs have a permanent porosity with pores in the micropore or low size mesopore range, up to 4-5 nm, as well as high chemical and thermal stabilities. Surface areas are tunable between 500 and 4200 $m^2 g^{-1}$. COFs are prepared by mechanochemical synthesis through polycondensation reactions under thermodynamic control [8]. The molecular length of the building units governs the pore size of COFs, while the shape of the building units determines the topology of the porous structures. Schiff-base chemistry is also applied to construct COFs [9, 10]. The possibility of tunning the textural properties of COF materials have made them strong candidates in applications for gas storage (including hydrogen, ammonia, methane and carbon dioxide), adsorption and catalysis [7].

1.3.2 Porous polymers

1.3.2.1 Micro and mesoporous permanent porous polymers

There are two main strategies for the synthesis of polymers with microporosity [11]. In the first one, an amorphous hypercrosslinked polymer is formed in the presence of a solvent that swells the network. After solvent removal, the extensive crosslinking reaction prevents the polymer chains from collapsing and a microporous material with high thermal stability is obtained. An important example is hypercrosslinked polystyrene (Fig. 1.5a) which is commercialized with a pore volume of 0.5-0.7 cm^3 g^{-1} [11]. Hypercrosslinked polymers are currently applied as adsorbents of organic vapors and organic contaminants from water, as well as for hydrogen storage [12].

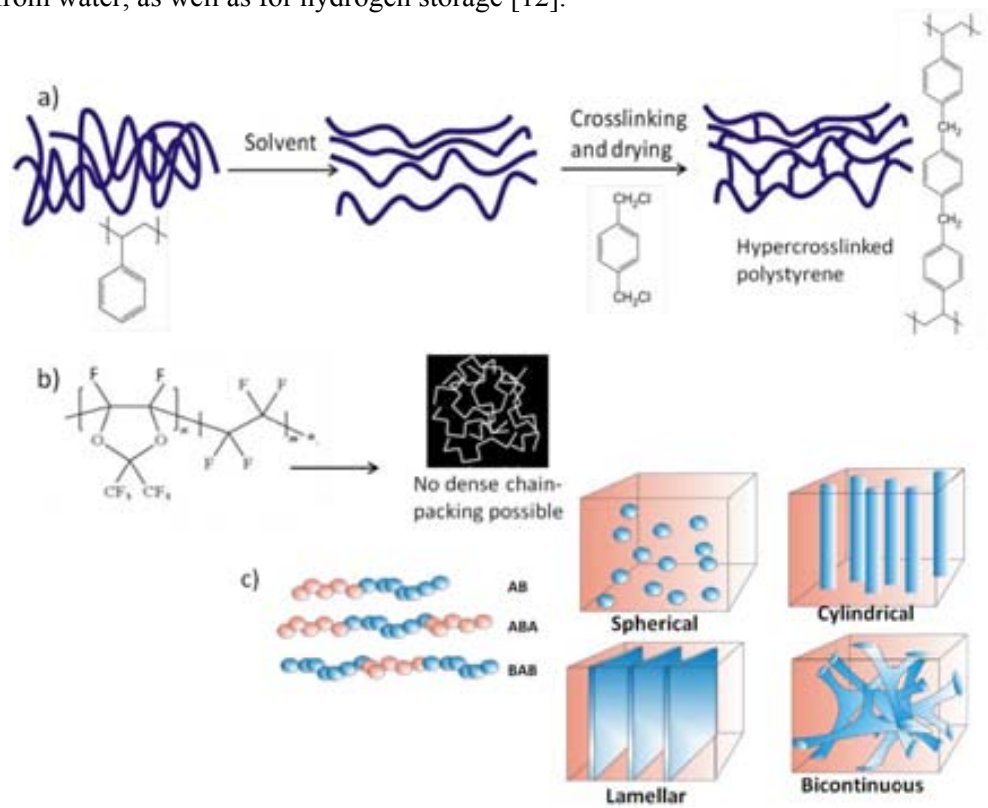

Figure 1.5 Examples of fabrication methods for permanent porous polymers: (a) Friedel-Craft alkylation synthesis of hypercrosslinked polystyrene [11], (b) geometrical constrains applied in the synthesis of Teflon AF 2400 [13], and (c) examples of different geometries obtained for diblock copolymers [14].

The second strategy for microporous polymer preparation is based on the possibility of using solely the geometry of the used monomers to define the microporosity, without the need of a template or blowing agent. The open void arises from the contorted molecular structure that prohibits an efficient packing of chains in the solid state. These polymers are prepared using a combination of hydroxylated and fluorinated or chlorinated aromatic monomers [15]. They exhibit surface areas between 500 and 1700 $m^2 g^{-1}$. There have been developed several microporous glassy polymers, which exhibit remarkably high gas permeability. Notable amongst these is the 2,2-bistrifluoromethyl-4,5-difluoro-1,3-dioxole–tetrafluoroethylene copolymer, designated as Teflon AF 2400 by Du Pont (Fig. 1.5b) that possesses high thermal stability and low reactivity towards acids, bases and oxidizing reagents [13].

Permanent mesoporous polymers are block copolymers, comprising two or more incompatible homopolymer subunits linked by covalent bonds (Fig. 1.5c) [16]. Block copolymers can yield a large variety of morphologies, including spheres, cylinders, bicontinous gyrois, lamellaes, etc (Fig. 1.5c), with space domains in the order of 5-35 nm [14]. Block copolymers are commercially available, being important examples thermoplastic polyurethanes, polyesters and polyamides.

1.3.2.2 Polymer foams

Polymer foams are structures formed by using chemical or physical blowing agents, together with especific nucleation agents and stabilizers [17]. Some common polymeric foams are polystyrene, polyurethane, polyethylene and polypropylene. Recently, the use of compressed carbon dioxide (CO_2) is a common method to prepare foamed amorphous or semicrystalline polymers, especially for biological applications [18]. According to this method, the polymer is saturated with compressed CO_2 at a constant temperature and pressure. Then the system is brought to supersaturation either by reducing the pressure or by increasing the temperature resulting in the nucleation and growth of the pores [19, 20]. Foamed polymers find applications in gas storage and separation, thermal insulation, catalysis, sporting equipment, tissue engineering, etc.

1.4 INORGANIC POROUS MATERIALS

1.4.1 Carbon materials

Important microporous carbon materials are activated carbons and carbon nanotubes [21, 22]. Activated carbon is produced from vegetals (wood, coconut shells, etc.), coal or polymers by a two-step process, involving carbonization at 450-900 °C in an inert atmosphere followed by an activation attained at 600-1200 ºC in an oxidizing atmosphere [23]. During the carbonization process, most of the noncarbon elements such as oxygen, hydrogen, and nitrogen are eliminated as volatile gaseous species creating interstices and, thus, microporosity (Fig. 1.6a). Activated carbons display surface areas from 500 to 1400 $m^2 g^{-1}$ and are characterized by a high hydrophobicity and an elevated corrosion resistance. Porous carbon materials can be also fabricated with uniform micro- and mesopores by using the template synthesis method and zeolites or mesoporous silicas as the template (Fig. 1.6b) [24]. Aside from zeolites, activated carbons represent the class of microporous materials with the highest industrial significance, partly because of their low production costs. They are applied in gas separation and adsorption processes, for water purification, as a catalyst supports or as a hosts for the immobilization of biomolecules for biosensors, in electrodes for electrochemical double layer capacitors and in fuel cells [21].

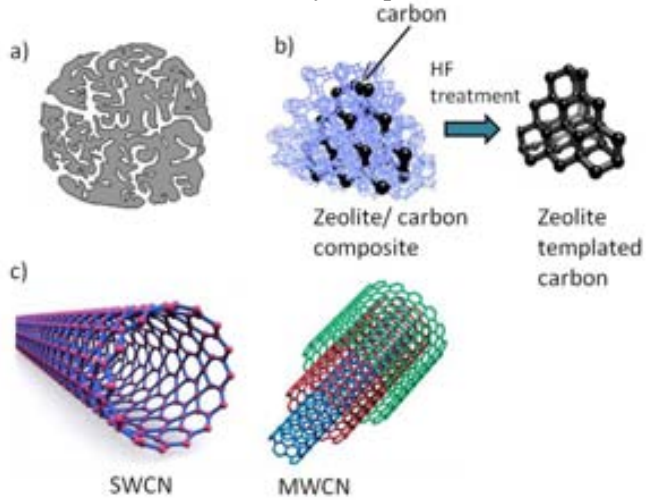

Figure 1.6 Representation of carbon materials: (a) disordered microporous activated carbon, (b) periodic carbon prepared using the template method, and (c) single (SWCN) and multi-walled (MWCN) carbon nanotubes.

Carbon nanotubes (CNTs) are allotropes of carbon with cylindrical structures and inherent porosity (Fig. 1.6c). In single-walled CNTs, the pore sizes are in two main ranges: < 5 nm and 10−100 nm [25]. Techniques such as arc discharge, high-pressure carbon monoxide disproportionation and chemical vapor deposition are used to produce nanotubes in commercial quantities. CNTs show high thermal and electrical conductivity, with applications in electronics and electrochemical. Moreover, nanotubes are used as a mechanical reinforcement in high performance composites, energy storage and for biological and chemical applications [26]

1.4.2 Silica

Silica is the common name for materials composed of silicon dioxide (SiO_2) occurring in both crystalline and amorphous forms [27]. Silica is found in nature as amorphous matter in the form of dense sand and as a crystalline compound in the form of quartz. Contrarily, synthetic silica is often prepared in the porous form [28]. Porosil is the general name of synthetic porous crystalline silica that includes zeosils and clathrasils, and silica gel is the denomination of porous synthetic amorphous silica [29]. In a silica material, the silicon atom is in a tetrahedral coordination with four oxygen atoms (Fig. 1.7a). Silica crystallizes in a diamond cubic crystal structure (Fig. 1.7b), whereas in amorphous silica the tetrahedra are randomly connected (Fig. 1.7c).

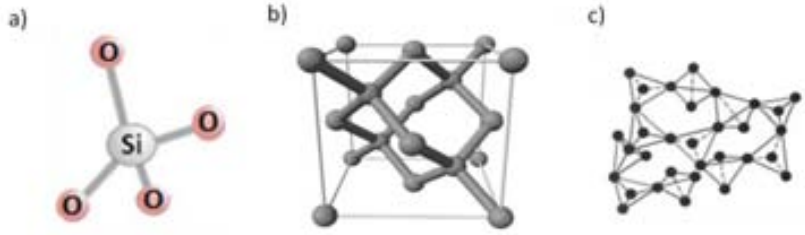

Figure 1.7 Schematic representation of: (a) the tetrahedra SiO^{4-}, (b) the cubic crystal structure of silica, and (c) amorphous silica.

1.4.2.1 Sol-gel process

The interest in the sol-gel process began in 1846 with Ebelman and Graham's studies on silica gel [30, 31]. Although in this thesis the sol-gel process is described for the preparation of porous silica, the method can also be applied to the synthesis of other metal oxides [32]. In the sol-gel process, the term "sol" refers to a dispersion of colloidal particles, whereas "gel" refers to a material consisting of a solid three-dimensional porous network entrapping a liquid phase. The sol-gel process allows the preparation of silica in different forms, such as nanoparticles, films or aerogels.

Silicon alkoxides of the type $Si(OR)_4$, where OR is an alkoxy group, are used as the monomer precursor for the sol gel reaction [33]. The most common used alkoxides are tetraethylorthosilicate (TEOS) and tetramethylorthosilicate (TMOS). The sol-gel process consists of a series of hydrolysis and condensation reactions of an alkoxide, which proceed according to the reaction scheme shown in Fig. 1.8.

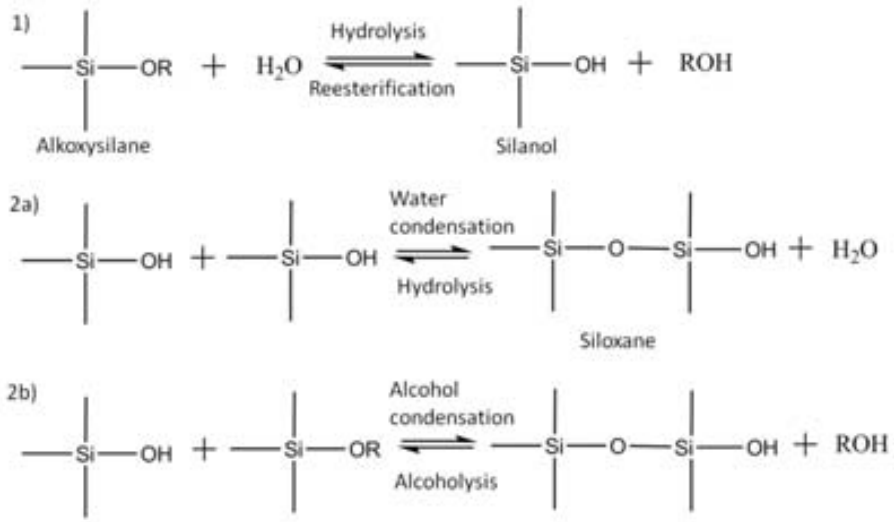

Figure 1.8 The three primary reactions the sol-gel process: (1) hydrolysis that replaces alkoxide groups (OR) by hydroxyl groups (OH), and (2a, 2b) condensation that produces siloxane bonds (Si-O-Si) plus the by-products water or alcohol.

Hydrolysis is initiated by the addition of water to a silane solution under acidic, neutral, or basic conditions (reaction 1 in Fig. 1.8). Since water and alkoxysilanes are immiscible, a mutual solvent such as an alcohol, is used to dissolve the silane. Under most conditions, condensation commences before hydrolysis is completed and reactions 2a and 2b in Fig. 1.8 occur simultaneously. A sol of amorphous silica primary particles (5-6 nm) is, thus, formed (Fig. 1.9a). Under base-catalyzed conditions in the sol, the primary particles tend to grow to sufficient size to become colloids (Fig. 1.9b). The colloidal particles can be separated form the liquid phase by chemical precipitation (Fig. 1.9c) or by solvent evaporation (Fig. 1.9d), giving place to precipitated silica. Under acid-catalyzed or neutral solutions, the interparticle forces between suspended particles in the sol or in the colloid have sufficient strength to cause considerable aggregation and/or flocculation. Both colloidal and primary particles can then link together to become a three dimensional network in a process called gelation (Fig. 1.9e). For the formation and aging of the gel, a long period of time, from hours to days, is needed. During the aging period, the strength of the gel network increases due to polycondensation. The resulting material receives the name of alcogel. A further step consists on drying the alcogel to remove the liquid from the interconnected pore network, obtaining either a xerogel by conventional solvent evaporation (Fig. 1.9f) or an aerogel by supercritical drying (Fig. 1.9g) [28, 34].

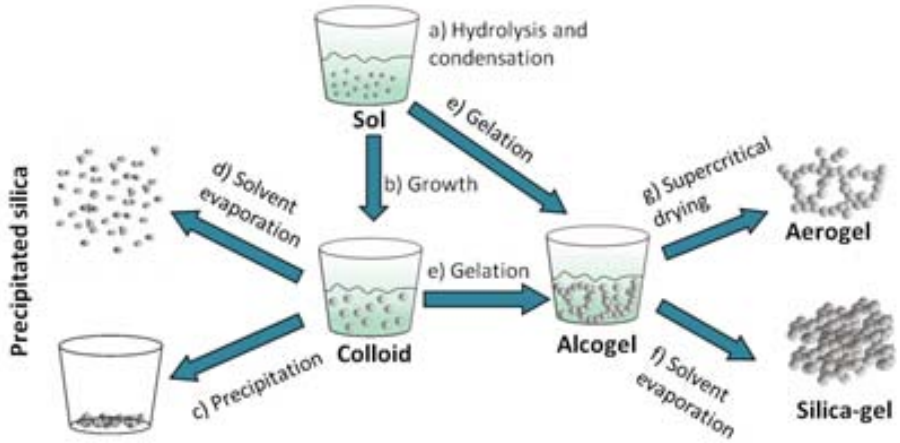

Figure 1.9 Schematic representation of the different stages and routes for silica materials preparation of the sol-gel process.

The surface chemistry of the silica deals with its hydrophilic character, which is related to the number of silanol or hydroxyl groups on the surface capable of forming hydrogen bonds with water molecules. Silanol groups in silica are classified into three types (Fig. 1.10): vicinal, geminal and isolated [35]. Vicinal silanols interact strongly with water molecules and are responsible for the excellent water adsorption properties of silica. The reported surface concentration of hydroxyl groups per square nanometer on hydrophilic silica products obtained by sol gel rangs es from 4 to 6 OH nm^{-2} [36]. When a calcination step is needed to obtained the silica products, e.g. fumed silica or ordered mesoporous silica, the surface density of silanols is considerably lower.

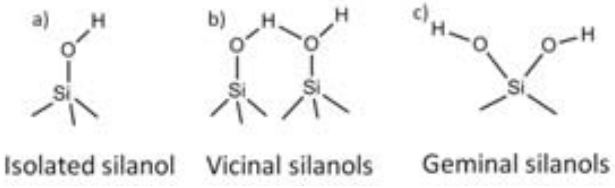

Figure 1.10 Schematic representations of isolated (a), vicinal (b) and geminal (c) silanols encountered on silica surfaces.

The major advantages associated with the sol-gel process include low processing temperatures, high levels of purity, easy control of dopants concentration and the ability to synthesize multiple component compositions in different product forms.

1.4.2.2 Silica nanoparticles

Colloidal silica is obtained through the sol-gel process (Fig. 1.9b) and stabilized by pH adjustment [37]. After solvent elimination (Fig. 1.9c,d), sub-micrometric and nanometric particles are precipitated. Obtained particles are dense and system porosity is associated to interparticle voids after particles aglomeration. The specific surface area for these kinds of products is typically in the range of 200 $m^2 g^{-1}$ and upwards. Silica nanoparticles are used as additives in cosmetics, fillers for paints, in polymer composites, as coating agents and in adhesives [38].

Pyrogenic or fumed silica is a different class of nanometric amorphous silica synthesized from the oxidation of $SiCl_4$ at temperatures exceeding 1000 °C (Fig. 1.11), giving place to non-porous primary particles, typically in the range of 2-50 nm, which collide to form aggregates of 1-250 µm [29, 38]. The product has a very low bulk density and a high specific surface area, typically 200-300 $m^2 g^{-1}$. Fumed silica is commercialized with the name of Aerosil® by Evonik. Fumed silica is applied as a thickener and as a high performance additive [39].

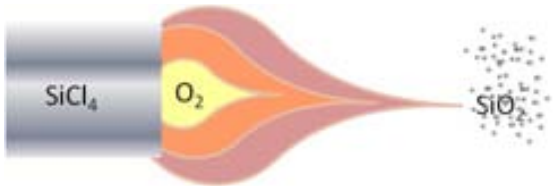

Figure 1.11 Preparation of fumed silica from the oxidation of $SiCl_4$ at high temperatures.

1.4.2.3 Porous silica gels and aerogels

A silica gel is an open 3D network obtained by the bulk condensation of either the sol or the colloidal silica (Fig. 1.9e). Depending on the applied drying technique, different materials are obtained: xerogels and aerogels (Fig. 1.9f,g).

If the drying step is carried out by solvent evaporation or under vacuum, a xerogel is obtained (Fig. 1.9f). These conventional drying methods lead to the partial collapse of the alcogel caused by capillary forces. The volume of the gel is reduced by 50-80 v% leading to a final pore volumen in the range of 0.4-0.8 cm^3 g and a solid with a pore size of 1-10 nm is obtained. Xerogels with micropores are used as high-capacity desiccants, since their pore size is adequate for an efficient absorption of water molecules. One example is silica blue, which is doped with cobalt chloride as a color indicator of the adsorbed water content. The color of the silica blue turns from blue to pink when water is absorbed. Porous silica gel materials are also used in the refining of oils to absorb phospholipids, trace metals and soaps. Silica gels can be used as absorbents for sulfur and nitrogen compounds, CO_2, gasoline-range hydrocarbons and aromatics [40].

By eliminating the solvent in the gel via supercritical drying (Fig. 1.9g), the network does not shrink and an extremely porous, low-density material, known as aerogel, is formed. The first aerogel was described by Teichner *et al.* in the 1960s [41]. There are two different methods of supercritical drying, either applying high temperature (HTSCD) or low temperature (LTSCD) [42]. In the HTSCD method, both the pressure and temperature are adjusted to reach values above the critical point of the solvent entrapped in the alcogel. The wet gel is placed in an autoclave and the temperature is slowly raised to *ca.* 250 ºC. Then, the fluid is vented at constant temperature avoiding liquid phase formation. In the LTSCD method, the solvent present in the gel is first replaced by pressurized CO_2 and then eliminated at low temperature (*ca.* 40 ºC). Aerogels can be produced in the form of monoliths, when the mature gel is dried in its container, or in the form of aerogel nanoparticles. In this last case, the primary particles suspension is not aged to form a gel and the supercritical fluid is used as the reactant media of the sol [43]. SiO_2 aerogels have unusual properties, such as extremely low density (< 0.5 g cm^{-3}), high specific surface area

(*ca.* 600-1200 $m^2 g^{-1}$), high porosity (80-99 %), high thermal insulation values, ultra low dielectric constant and low index of refraction [44]. Their thermal insulation properties have made them ideal materials to be applied in home building, vehicles or pipelines. Aerogel beads can be used as translucent spacers in windows for daylight applications. Silica aerogels have been also used for the NASA as insulators in space shuttle missions [42].

1.4.2.4 Ordered mesoporous silica

The family of Ordered Mesoporous Silica (OMS) was discovered by the Mobil company (USA) in 1992 [45, 46], and it is also referred in the literature as Mobil Composition of Matter (MCM) or as Mesoporous Molecular Sieves (MMS). OMSs are amorphous mesoporous products with a high degree of periodicity on the arrangement of the pores. The different classes of OMS products are obtained through the templating method [46]. The synthesis requires a source of silica, a structure-directing amphiphile, such as surfactants or block-copolymers, and a solvent (usually water). In short, the inorganic source of silica (TEOS or TMOS) is hydrolyzed and then mixed with the structure-directing agent. The alkoxides polymerize and crosslink around the micelle template. The mixture is then hydrothermally aged (≥ 100 ºC) for several hours (24-150 h). The process is concluded with the removal of the template, by either calcination at *ca.* 500 ºC or washing with an organic solvent. Fig. 1.12 shows the scheme of the synthesis of the MCM-41 phase [46]. As a function of the used surfactant, the micelles can be organized in different symmetries and the final porous material adopts different structures: 1D hexagonal for MCM-41, 3D cubic for MCM-48, and 2D-like lamellar for MCM-50 [47]. The type of surfactant also defines the pore size. In general, this class of materials has a uniform pore size distribution in the mesopore range, tunable between 2 nm and 10 nm, a high specific surface area ranging from 700 to 1500 $m^2 g^{-1}$, and a high porosity (*ca.* 1 $cm^3 g^{-1}$). Some cubic MMSs, labelled as SBA-1, SBA-6 and SBA-16, are synthesized under acidic conditions and have a unusual micro-meso bimodal pore size distribution. OMSs

are used for catalytic applications and in adsorption processes [47]. Currently, there is an active research in the adsorption of CO_2 using OMS products [48-50].

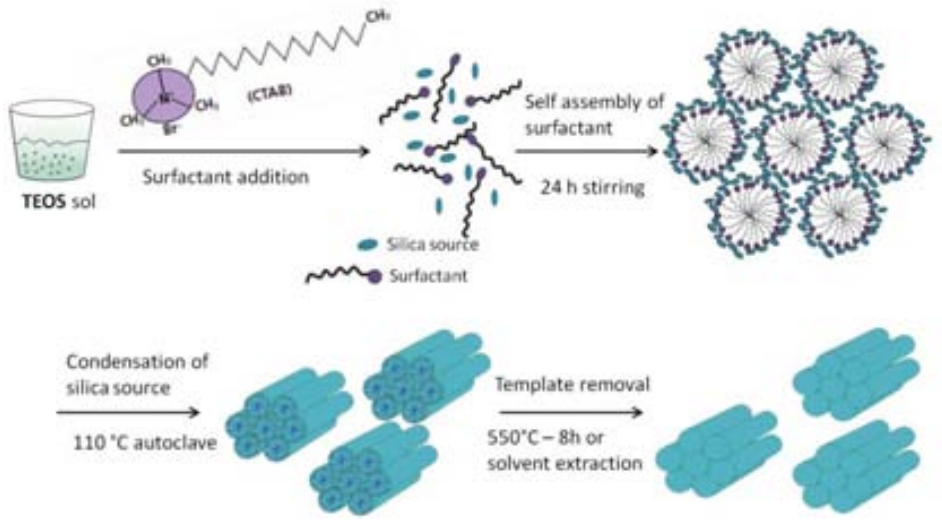

Figure 1 .12 Synthesis of MCM-41 via the te mplating rout e. The long alkyl chain le ngth quaternary d irecting age nts (CTAB) self-assemble to supramolecular species (micelles), which generate the formation of the mesoporous silica under hydrothermal treatment.

1.4.3 Silicates

Silicates are defined as compounds containing silicon atoms surrounded by ox ygen to form anions of the type $[SiO_4]^{4-}$ (Fig. 1.7a). Natural silicates can exist in both crystalline and amorphous states [51, 52]. The tetrahedral anions are able to form polymers by linkage with on e, two, th ree or fo ur neig hbouring tetrahedra, fo rming siloxane Si-O-Si bo nds. Other ions can be located in the silicate lattices such as to lithium, sodium, calcium, boron, aluminum, etc. Some c ations, such as aluminum, are able to isomorphically substitute silicon atoms in the silica-oxygen tetrahedra. However, most of them are located out of the anionic framework and pla y th e role of charg e balanced cations. Important gr oups of silicates are the t ectosilicates (fra mework silicates) and p hyllosilicates (lay ered silicates). The tectosilicates hav e a three dimensional fra mework where al l four oxy gen atoms of

each tetrahedral are shared by adjacent tetrahedra. Zeolites are tectosilicates, in which a substitution of silicon for aluminum occurs [53]. Phyllosilicates have two-dimensional layers of $[SiO_4]^{4-}$ tetrahedra sharing three oxygen atoms between each other. Such structures have the ability to split along definite smooth planar surfaces (clays) [54].

1.4.3.1 Zeolites

The term zeolite was formalized by the Baron A. F. Cronstedt in 1756, who also established the first classification [55]. Zeolites are hydrated tectoaluminosilicates constructed by TO_4 tetrahedra (T=tetrahedral atom, either Si or Al, Fig. 1.7a), in which each oxygen atom in the corner is shared between two adjacent tetrahedra (Fig. 1.13a) giving a miriad of different structures with a framework ratio of O/T=2. Low aluminium content zeolites (Si/Al > 10) have low framework charge, since the silicon atom is tetravalent. The most important of these are the ZSM-5 zeolite and the zeolite-β (Fig. 1.13b). Contrarily, aluminosilicates with high aluminium content have a negatively charged framework, which requires balancing with extra-framework positive ions, such as alkali or alkaline ions. Examples of high aluminium content products are zeolites A, X and Y with a Si/Al ratio close to unity (Fig. 1.13c). The Si/Al ratio plays an important role in adsorption, catalysis and ion-exchange applications [56]. Zeolites are of natural occurrence, but they can also be synthesized under hydrothermal conditions [57]. Roughly, 130 different zeolite framework structures are known [58].

Unique properties of zeolites arise from their uniformity in pore size given by their crystalline nature. Pores are about the same size of small organic molecules (0.5-2 nm) and they consist on interconnected cages or channels, which can have dimensionalities from one to three. Pore volumes in zeolites vary from 0.1 to 0.4 $cm^3\ g^{-1}$. Zeolites have many industrial applications in the areas of catalysis, adsorption and ion exchange. Examples in catalysis are H_2S oxidation, CO_2 hydrogenation and oxidation of CH_4 [56]. As adsorbents, zeolites are used for the removal of CO_2 from flue gases and for the separation of sulfur or O_2 compounds from air. In ion exchange applications, zeolites major use is as a water softening in the detergent industry.

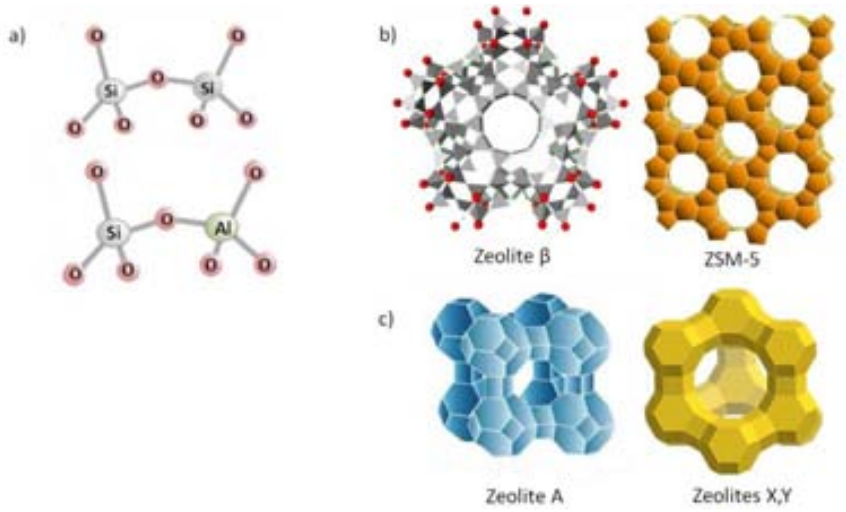

Figure 1.13 Zeolites topology: (a) possible forms of shared tetrahedra composing the framework, and examples of (b) high Si/Al ratio zeolites and (c) low Si/Al ratio zeolites

1.4.3.2 Clay minerals

Clay minerals are crystalline aluminophyllosilicates, divided in to kaolinite, montmorillonite-smectite and illite main groups. Basic building blocks of clay minerals are SiO_4 silica tetraheda linked together to form sheets. The tetrahedral sheets are combined with octahedral sheets containing Al^{+3}, and sometimes other cations, surrounded by 6 oxygens or hydroxyls neighbors (Fig. 1.14a). Clays are microporous materials, in which water and organic molecules can enter into the interlayer region leading to the swelling phenomena and resulting in an enlarged interlayer space (Fig. 1.14b). Expanded clay minerals facilitate easier infiltration of compounds into the clay interlayer space. The final structure is exfoliated clays. Kaoline clays are applied in the paper, ceramic, paint, plastic, rubber and cracking catalyst industries. Other clays such as sepiolite are used as adsorbents in pet litter, agricultural chemicals, water and oil sorption, pharmaceuticals, etc [59].

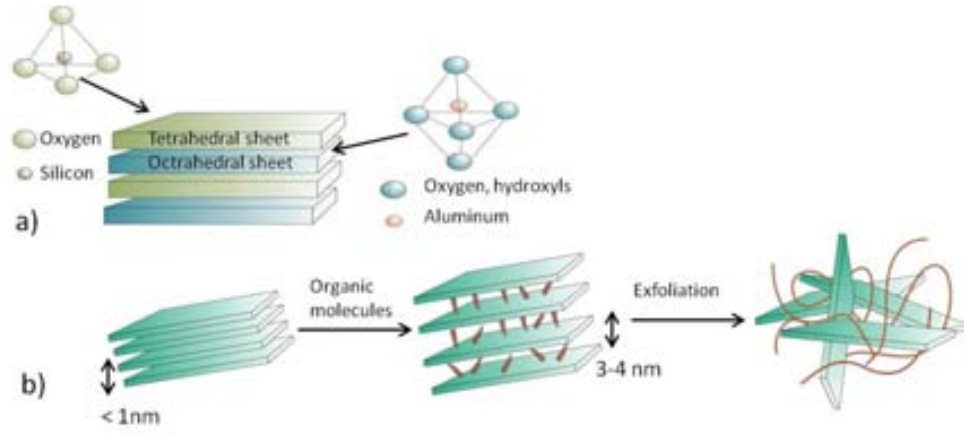

Figure 1.14 Schematic representation of: a) tetrahedral and octahedral sheets conforming the clay structure, and b) swelling and exfoliation of the clay structure.

1.4.4 Meso-macroporous minerals

Porous inorganic materials having meso- and macropores are found in the nature mainly in the form of minerals. In their chemical composition, SiO_2 is combined with other oxides such as Al_2O_3, FeO, Na_2O, etc. Examples of such porous minerals are vermiculite, diatomaceous earth, bentonite, kaolinite and perlite [60]. There is a wide range of applications for these materials. For instance, bentonite is widely applied as a binder for iron and steel foundries, in the purification of wine and as an adsorbent of oils [61]. Diatomaceous earth is extensively applied as a filter aid, adsorbent, insulating material, catalyst support or carrier and natural insectide [62]. Expanded perlite is a very lightweight material applied in the construction industry, as a rooting medium and soil conditioner in horticulture, as an adsorbent in the chemical industry and as a filler in miscellaneous processes [63].

1..5 ORGANIC-INORGANIC POROUS MATERIALS

The combination of inorganic and organic properties in a single material is attractive for the development of materials with new fu nctionalities. These fu nctionalities can be introduced in a single step during the synthesis of the porous material (direct synthesys) or by post-functionalization of the already synthesized porous material.

1.5.1 Direct synthesis

Representative porous materials prepared through the direct synthesis method are metal organic frameworks and periodic mesoporous organosilicas.

1.5.1.2 Metal Organic Frameworks

Metal organic fra meworks (MOFs) are highly crystallin e compounds con sisting of metal ions or clusters coordinated with rigid organic molecules to form one-, two- or three-dimensional structures [64]. Fig. 1.15 illustrates examples of 2D and 3D MOFs.

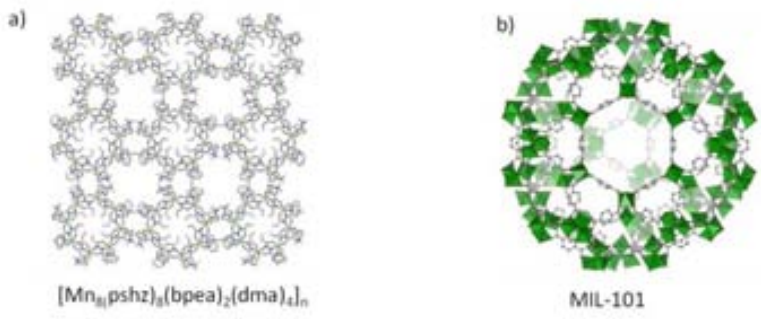

Figure 1.15 Representation of MOF structures: (a) 2-D layered, and (b) 3-D.

The choice of metal and l inker dictates the structure and , hence, th e properties of the MOF. MOFs di splay an extraordinary compositional and structu ral variety with well - defined pores and channels. The pore size within the framework of a MOF is typically less than 2 nm . High in ternal surface area is on e of the fo remost attributes of MOFs. The highest experimental surface area for a MOF reported to date is 7000 $m^2 g^{-1}$ and it has been

demonstrated computationally that the theoretical upper limit for MOF surface areas is *ca.* 14600 $m^2 g^{-1}$ [65]. MOFs are prepared by reacting metal ions with an organic ligand, using standard coordination chemistry methods, through hydrothermal or solvothermal techniques. Maximization of surface area is a key to the optimization of MOFs for many applications. Careful post-processing with supercritical carbon dioxide leads to substantial, or in some cases spectacular (up to 1200 %), increases in gas-accesibble surface area, due principally to solvent elimination [66]. Potential applications of MOFs are the storage of fuels and gases such as hydrogen, methane, carbon dioxide and oxygen, and in heterogeneous catalysis [67].

1.5.1.3 Organically modified silica

Trialkoxyorganosilanes of the type $(RO)_3SiR'$, containing the R' functional group, can be incorporated during the sol-gel process of silica formation, consequently being the functionality R' projected into the pores. Through this co-condensation method, it is possible to obtain organically modified silica gels (ormosils) [68] and functionalized aerogels [69]. On a similar way, periodic mesoporous organosilicas can be obtained if tryalkoxysilanes are introduced during the condensation step around the micelle template [70]. The wide range of molecules that can be introduced allows the control of the charge, functionality, reactivity and stability of the porous material.

1.5.2 Post-synthesis functionalization: silanization

A simple and cost-effective way of regularly organize chemical entities on surfaces is represented by self-assembly [71]. One of the most successful self-assembly approach is the chemical grafting of organosilanes on hydrated surfaces (silanization). Silanol groups from the internal surface of porous silica are the reactive sites where the molecules are anchored via covalent or hydrogen bonding.

Organosilanes are chemical compounds with the general formula$(OR)_nSiR'_{4-n}$,where R' represents the functional group and OR is the hydrolysable group, usually an alkoxy group,

either methoxy or ethoxy. According to the number of hydrolysable groups, organosilanes can be mono-, di, or trisilanes for n=1, 2 or 3, respectively [72]. Fig. 1.16 illustrates some of the common functional and hydrolysable groups available for organosilanes.

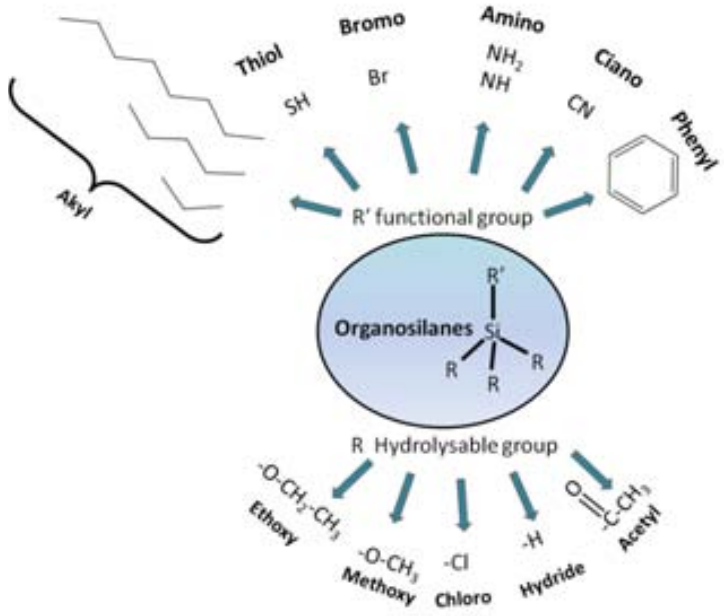

Figure 1.16 Common hydrolysable and functional R groups in organosilanes.

In the silanization process, the actual bottom-up mass-production methods involve techniques such as gaseous deposition for high vapor pressure silanes, and liquid chemisorption, where the self-assembled monolayer is spontaneously formed by the immersion of the substrate into a water-diluted alcoholic silane solution [73, 74]. In the liquid aproach, the silanization mechanism can be divided into two steps (Fig. 1.17):

Step 1. Hydrolysis of the alkoxy group: the initiation of the silanization occurs by the hydrolysis of one or more alkoxy group(s) promoted by water molecules (Fig. 1.17a), either added to the reaction medium or present as a moisture adsorbed on the pores of the inorganic substrate. Alkyl groups are released in the form of an alcohol (R-OH).

Step 2. Condensation: the hydrolyzed organosilane is now susceptible to react with other silane molecules and with the silanol groups from the silica surface, establishing

siloxane linkages (Si-O-Si). Both siloxane bonds and hydrogen bonding with the silanol groups on the silica surface are possible reactions (Fig 1.17b).

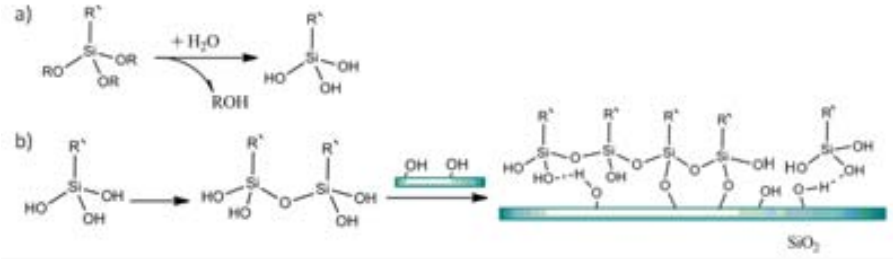

Figure 1 .17 Mechanism of silanization: (a) hydrolysis of the al koxy groups in the organosilane, an d (b) condensation between org anosilane molecules and with the surface silanols forming a self-assembled structure.

The chemical gr afting of organosilane allows to attain high fu nctionalization deg rees and well -ordered monolayers without altering the po rous structure of the origin al silica [75]. Disadvantages of the liquid chemisorption route are related to the need of applying a large volume of water and organic sol vents. Moreover, applying th is route the re may be undesired side reactions, such a s excessive cross-linking of hydrolyzed organosilane molecules in solution (Fig. 1.18a), multilayer deposition on the silica surface, non-uniform surface coverage due to vertical polymerization (Fig. 1.18b) and pore-blocking [76-80].

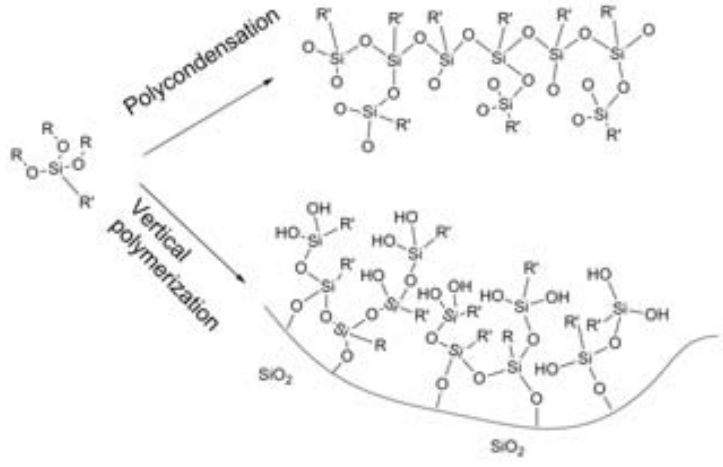

Figure 1 .18 Side reactions of the sila nization proc ess using conve ntional liquid solvents.

In order to avoid such problems, liquid solvents can be substituted by supercritical carbon dioxide as the solvent media. Supercritical carbon dioxide has been demonstrated as an efficient technology for the silanization of silica substrates [79, 81-87].

1.6 POROUS MATERIALS USED IN THIS WORK

Ten different silicium-based materials are scrutinized in this work. All of them satisfy the key attributes required for inorganic supports to be used as solid sorbents: inertness, robustness over a wide range of pressure and temperature and easiness of functionalization. Some important characteristics of the processed matrices are shown in Table 1.1, whereas Table 1.2 summarizes the textural properties. Studied materials belong to very diverse groups of porous solids:

i. Mesoporous silica gels: silica blue, clean cat and silica gel 40.
ii. Ordered mesoporous silica: MCM-41.
iii. Microporous aluminosilicates: zeolite Y.
iv. Microporous aerogel-like particles: silica and a composite magnetite/silica.

Table 1.1 Matrices classification and some important characteristics.

Type	Substrate	Sample	Supplier	SiO_2 [wt%]	Particle size [nm]
Mesoporous	CleanCat	CC	Iberamigo SA	>99.8	$20 \cdot 10^5$ -$50 \cdot 10^5$
	Silica Gel 40	SG_{40}	Fluka	>99.8	$2 \cdot 10^5$ -$5 \cdot 10^5$
	MCM-41	MCM41	ACS Materials	>99.5	200-500
Meso- and microporous	Silica Blue	SB	Fluka	>99.8	$10 \cdot 10^5$ -$30 \cdot 10^5$
Microporous	Zeolite Y	ZY	Strem Chemicals	49	$2 \cdot 10^4$ -$5 \cdot 10^4$

Table 1.2 Main textural properties of th e used substrates o btained from low temperature N_2 adsorption.

Sample	S_a [$m^2 g^{-1}$]	V_p [$cm^3 g^{-1}$]	D_p [nm]
CC	440	0.96	8.8
SG_{40}	591	0.58	4.1
MCM41	1127	0.92	3.8
SB	611	0.10	2
ZY	739	0.38	1.3**

* value from MIP [88]
** Geometrical data [52]

1.6.1 Mesoporous and meso/microporus silica gels

Hydrophilic mesoporous silica gels are extremely important commercial materials (Fig. 1.20). The choice of such amorphous silica materials as important adsorbents in this thesis relies on their low cost and adsorbent properties that are suitable for a large amount of bulk applications. Amorphous silica gels CC and SG_{40} have a di sordered pore structu re and surface areas in the order of 400–500 $m^2 g^{-1}$. Mean pore diameters are of 9 and 4 nm for CC and SG_{40}, respectively. SB, with cobalt chloride as a humidity indicator, has a mixture of meso- and microporosity with a mean pore diameter of 2 nm and a surface area in the order of 600 $m^2 g^{-1}$. This material was partially dehydrated before use by heating it in an air oven at 120 ºC during 20 h. Polar silica gel substrates have a highly reactive surface with a hydroxyl surface density of 4-6 OH nm^{-2}.

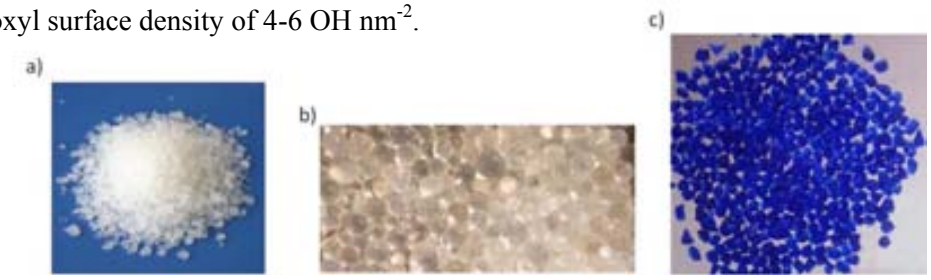

Figure 1.20 Pictures of th e silica gel s used: (a) Clean Cat, (b) Sili ca Gel 40 and (c) dehydrated silica blue.

1.6.2 Mesoporous MCM-41

MCM-41 is chosen here as the representant of the ordered mesoporous silica family, with a pore diameter of 4 nm (Fig. 1.21). MCM-41 has a periodic arrangement with uniform hexagonal channels running parallel in one-dimensional non-intersecting arrays [89, 90]. This material has an extremely high mesopore volume in the order of 0.9 $cm^3 g^{-1}$ and a surface area of *ca.* 1100 $m^2 g^{-1}$. The mesoporous MCM-41 was boiled in distilled water at 100 ºC for 1 h [91] previous use to increase the surface silanol density from 1 to 3 OH nm^{-2}.

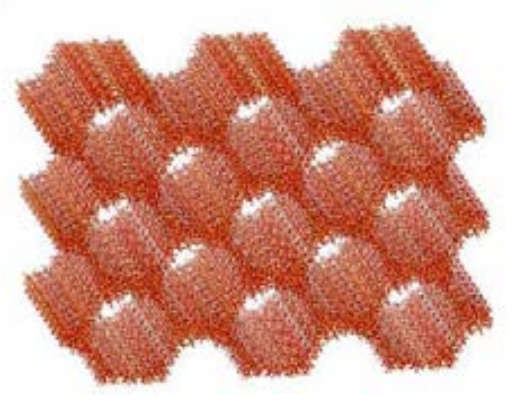

Figure 1.21 Representation of the hexagonal structure of the MCM-41.

1.6.3 Microporous zeolite

Zeolite Y, from the Faujasite class, is chosen as the microporous substrate. It is an aluminosilicate with the chemical formula $[(Ca^{2+},Mg^{2+}Na^{+}_{2})_{29}(H_2O)_{240}]$ $[Al_{58}Si_{134}O_{384}]$ and a tridirectional ordered network of pores. This zeolite consists in almost spherical cavities of 1.3 nm in diameter accessible through tetrahedral windows of 0.74 nm (Fig. 1.23) [58]. This zeolite nust be activated before it can be used as an adsorbent. The activation was carried out by calcination in a tubular oven (Carbolite 3216) at 520 ºC during 48 h under a flow of nitrogen with oxygen traces. The zeolite surface area after calcination has a value of 740 $m^2 g^{-1}$ being the pore volume of 0.38 $cm^3 g^{-1}$. In a perfect zeolite crystal, the internal pore surface is electrically neutral, and no silanols would be present. Silanol groups in crystalline zeolite Y are mostly present in the external surface as terminal groups.

Experimentally, some internal silanols have been noticed and are taken as an indication of lattice defects.

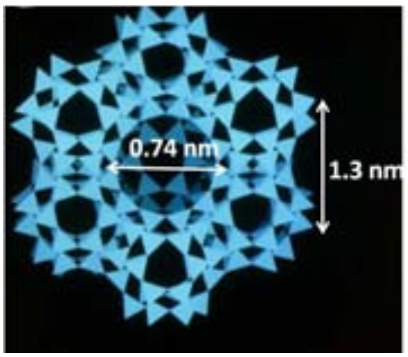

Figure 1.23 Representation of the molecular structure of the zeolite Y. The supercage in zeolite has a 1.3 nm diameter accessible through tetrahedral windows of 0.74 nm.

1.7 CONCLUSIONS

We have presented here an overview of the most common adsorbent materials, with key characteristics, such as synthesis, chemical composition and porous size. Among them, porous silica based materials were chosen in this work to modify their surface by chemical grafting with organic functionalities. These materials were chosen for several reasons: *i)* their pore size varied from the micro- to the mesoporous range allows the easy insertion of organic molecules, *ii)* the presence of silanol groups in most of the porous substrates allows the chemical grafting of organosilanes, *iii)* some of the porous substrates, such as silica gels, are low cost materials and, therefore, suitable for a large amount of bulk applications, *iv)* finally, the compositional and textural differences on the porous materials chosen allow to study and compare their influence on the final properties of the organic modified products. Results concerning their synthesis process, characterization and adsorption properties are presented and discussed in chapters III and IV.

1.8 REFERENCES

1. J. Rouquerol, D. Avnir, C.W. Fairbridge, D. H. Everett, J. H. Haynes, N. Pernicone, J.D. F. Ramsay, K.S.W. Swing, and K.K. Unger, *Recommendations for the characterization of porous solids* International Union of Pure and Applied Chemistry, 1994, 66(8), 1739.
2. D.H.E. K.S.W. Sing, R.A.W. Haul, L. Moscou, R.A. Pierotti, J. Rouquerol and T. Sieminiewska, , Pure and Appl. Chem., 1985, 57(4), 603.
3. R. Dawson, A.I. Cooper, and D.J. Adams, *Nanoporous organic polymer networks.* Progress in Polymer Science, 2012, 37(4), 530.
4. S. Polarz and B. Smarsly, *Nanoporous Materials.* Journal of Nanoscience and Nanotechnology, 2002, 2(6), 581.
5. G.L. Athens, R.M. Shayib, and B.F. Chmelka, *Functionalization of mesostructured inorganic–organic and porous inorganic materials.* Current Opinion in Colloid & Interface Science, 2009, 14(4), 281.
6. X.S. Zhao, F. Su, Q. Yan, W. Guo, X.Y. Bao, L. Lv, and Z. Zhou, *Templating methods for preparation of porous structures.* Journal of Materials Chemistry, 2006, 16(7), 637.
7. S.-Y. Ding and W. Wang, *Covalent organic frameworks (COFs): from design to applications.* Chemical Society Reviews, 2013, 42(2), 548.
8. X. Feng, X. Ding, and D. Jiang, *Covalent organic frameworks.* Chemical Society Reviews, 2012, 41(18), 6010.
9. Y. Jin, Y. Zhu, and W. Zhang, *Development of organic porous materials through Schiff-base chemistry.* CrystEngComm, 2013, 15(8), 1484.
10. A.M. Lopez-Periago, C.A. Garcia-Gonzalez, and C. Domingo, *Towards the synthesis of Schiff base macrocycles under supercritical CO2 conditions.* Chemical Communications, 2010, 46(24), 4315.
11. V.A. Davankov and M.P. Tsyurupa, *Structure and properties of hypercrosslinked polystyrene—the first representative of a new class of polymer networks.* Reactive Polymers, 1990, 13(1–2), 27.
12. S. Xu, Y. Luo, and B. Tan, *Recent development of hypercrosslinked microporous organic polymers.* Macromolecular Rapid Communications, 2013, 34(6), 471.
13. I. Pinnau and L.G. Toy, *Gas and vapor transport properties of amorphous perfluorinated copolymer membranes based on 2,2-bistrifluoromethyl-4,5-difluoro-1,3-dioxole/tetrafluoroethylene.* Journal of Membrane Science, 1996, 109(1), 125.
14. V. Abetz, *Block Copolymers II*, ed. V. Abetz2005: Springer.
15. P.M. Budd, S.M. Makhseed, B.S. Ghanem, K.J. Msayib, C.E. Tattershall, and N.B. Mckeown, *Microporous polymeric materials.* Materials Today, 2004, 7(4), 40.
16. M. Hillmyer, *Nanoporous Materials from Block Copolymer Precursors*, in *Block Copolymers II*, V. Abetz, Editor,2005, Springer Berlin Heidelberg. p. 137.
17. C. Khemani Kishan, *Polymeric Foams: An Overview*, in *Polymeric Foams*,1997, American Chemical Society. p. 1.

18. L.J.M. Jacobs, M.F. Kemmere, and J.T.F. Keurentjes, *Sustainable polymer foaming using high pressure carbon dioxide: a review on fundamentals, processes and applications.* Green Chemistry, 2008, 10(7), 731.
19. I. Tsivintzelis, A.G. Angelopoulou, and C. Panayiotou, *Foaming of polymers with supercritical CO2: An experimental and theoretical study.* Polymer, 2007, 48(20), 5928.
20. A. Salerno, U. Clerici, and C. Domingo, *Solid-state foaming of biodegradable polyesters by means of supercritical CO2/ethyl lactate mixtures: Towards designing advanced materials by means of sustainable processes.* European Polymer Journal, 2014, 51(0), 1.
21. J. Lee, J. Kim, and T. Hyeon, *Recent progress in the synthesis of porous carbon materials.* Advanced Materials, 2006, 18(16), 2073.
22. R.H. Baughman, A.A. Zakhidov, and W.A. De Heer, *Carbon nanotubes - The route toward applications.* Science, 2002, 297(5582), 787.
23. R.C. Bansal; and M. Goyal, *Activated Carbon Adsorption*, ed. T. Francis2005: CRC Press.
24. John H. Knox and B. Kaur, *Structure and performance of porous graphitic carbon in liquid chromatography.* Journal of Chromatography A, 1986, 352, 3.
25. Y.H. Hu and E. Ruckenstein, *Pore Size Distribution of Single-Walled Carbon Nanotubes.* Industrial & Engineering Chemistry Research, 2004, 43(3), 708.
26. Q. Zhang, J.-Q. Huang, W.-Z. Qian, Y.-Y. Zhang, and F. Wei, *The Road for Nanomaterials Industry: A Review of Carbon Nanotube Production, Post-Treatment, and Bulk Applications for Composites and Energy Storage.* Small, 2013, 9(8), 1237.
27. R.K. Iller, *The Chemistry of Silica: Solubility, Polymerization, Colloid and Surface Properties, and Biochemistry*, ed. A.W.I. Publication1979.
28. K.K. Unver, *Porous silica*1979The Netherlands: Elsevier Scientific Publishing Company.
29. E.F. Vansant;, P.V.D. Voort;, and K.C. Vranchken, *Characterization and chemical modification of the silica surface*, ed. E. ScienceAmnsterdam, The Netherlands: Elsevier Science.
30. M. Ebelmen, Ann. Chimie Phys, 1846, 16.
31. T. Graham, J. Chem. Soc, 1864, 17.
32. J.D. Wright; and N.a.J.M. Sommerdijk, *Sol-Gel Materials: Chemistry and Applications*: CRC Press.
33. L.L. Hench and J.K. West, *The sol-gel process.* Chemical Reviews, 1990, 90(1), 33.
34. A. Soleimani Dorcheh and M.H. Abbasi, *Silica aerogel; synthesis, properties and characterization.* Journal of Materials Processing Technology, 2008, 199(1), 10.
35. L.T. Zhuravlev, *The surface chemistry of amorphous silica. Zhuravlev model.* Colloids and Surfaces A: Physicochemical and Engineering Aspects, 2000, 173(1-3), 1.
36. R. Mueller, H.K. Kammler, K. Wegner, and S.E. Pratsinis, *OH Surface Density of SiO2 and TiO2 by Thermogravimetric Analysis.* Langmuir, 2002, 19(1), 160.
37. I. Rk, *The Chemistry of Silica: Solubility, Polymerization, Colloid and Surface Properties and Biochemistry*, ed. Wiley1979New York Wiley.

38. O.W. Flörke, H.A. Graetsch, F. Brunk, L. Benda, S. Paschen, H.E. Bergna, W.O. Roberts, W.A. Welsh, C. Libanati, M. Ettlinger, D. Kerner, M. Maier, W. Meon, R. Schmoll, H. Gies, and D. Schiffmann, *Silica*, in *Ullmann's Encyclopedia of Industrial Chemistry*,2000, Wiley-VCH Verlag GmbH & Co. KGaA.
39. H. Barthel, L. Rösch, and J. Weis, *Fumed Silica - Production, Properties, and Applications*, in *Organosilicon Chemistry Set*,2008, Wiley-VCH Verlag GmbH. p. 761.
40. G. Cao, Y. Lu, L. Delattre, C.J. Brinker, and G.P. López, *Amorphous silica molecular sieving membranes by sol-gel processing.* Advanced Materials, 1996, 8(7), 588.
41. G.A. Nicolaon and S.J. Teichner, Bull. Soc. Chim. Fr., 1968.
42. J. Fricke and T. Tillotson, *Aerogels: production, characterization, and applications.* Thin Solid Films, 1997, 297(1–2), 212.
43. N. Murillo-Cremaes, A.M. López-Periago, J. Saurina, A. Roig, and C. Domingo, *Nanostructured silica-based drug delivery vehicles for hydrophobic and moisture sensitive drugs.* The Journal of Supercritical Fluids, 2013, 73(0), 34.
44. N. Hüsing and U. Schubert, *Aerogels—Airy Materials: Chemistry, Structure, and Properties.* Angewandte Chemie International Edition, 1998, 37(1-2), 22.
45. J.S. Beck, J.C. Vartuli, W.J. Roth, M.E. Leonowicz, C.T. Kresge, K.D. Schmitt, C.T.W. Chu, D.H. Olson, and E.W. Sheppard, *A new family of mesoporous molecular sieves prepared with liquid crystal templates.* Journal of the American Chemical Society, 1992, 114(27), 10834.
46. C.T. Kresge, M.E. Leonowicz, W.J. Roth, J.C. Vartuli, and J.S. Beck, *Ordered mesoporous molecular sieves synthesized by a liquid-crystal template mechanism.* Nature, 1992, 359(6397), 710.
47. J.Y. Ying, C.P. Mehnert, and M.S. Wong, *Synthesis and applications of supramolecular-templated mesoporous materials.* Angewandte Chemie - International Edition, 1999, 38(1-2), 57.
48. Y. Belmabkhout, R. Serna-Guerrero, and A. Sayari, *Adsorption of from dry gases on MCM-41 silica at ambient temperature and high pressure. 1: Pure adsorption.* Chemical Engineering Science, 2009, 64(17), 3721.
49. C.A. Koh, T. Montanari, R.I. Nooney, S.F. Tahir, and R.E. Westacott, *Experimental and computer simulation studies of the removal of carbon dioxide from mixtures with methane using AlPO4-5 and MCM-41.* Langmuir, 1999, 15(18), 6043.
50. M. Kruk, M. Jaroniec, and A. Sayari, *Adsorption study of surface and structural properties of MCM-41 materials of different pore sizes.* Journal of Physical Chemistry B, 1997, 101(4), 583.
51. W. Eytel, *The physical Chemistry of the Silicates*, ed. U.o.C. Press1954.
52. Y. Ma, W. Tong, H. Zhou, and S.L. Suib, *A review of zeolite-like porous materials.* Microporous and Mesoporous Materials, 2000, 37(1–2), 243.
53. Y. Ma, W. Tong, H. Zhou, and S.L. Suib, *A review of zeolite-like porous materials.* Microporous and Mesoporous Materials, 2000, 37(1-2), 243.
54. J.E. Shelby, *Introduction to Glass Science and Technology* ed. T.r.S.o. Chemistry2005.

55. A.F. Masters and T. Maschmeyer, *Zeolites – From curiosity to cornerstone.* Microporous and Mesoporous Materials, 2011, 142(2–3), 423.
56. K.a.C. Scott M. Auerbach, Prabir K. Dutta, *Handbook of Zeolite Science and Technology* New York, USA.
57. C.S. Cundy and P.A. Cox, *The hydrothermal synthesis of zeolites: Precursors, intermediates and reaction mechanism.* Microporous and Mesoporous Materials, 2005, 82(1–2), 1.
58. *International Zeolite Association (IZA) Structure Commission*. 1977; Available from: www.iza-structure.org.
59. H.H. Murray, *Overview — clay mineral applications.* Applied Clay Science, 1991, 5(5–6), 379.
60. P.W. Scott; and C.M. Bristow, *Industrial Minerals and Extractive Industry Geology*, ed. P.W. Scott; and C.M. Bristow2002London, England: The Geological Society.
61. H. J.W.; and S.H. Patterson, *Bentonite and Fuller's earth resources of the United States* U.S.G.S.P.P. 1522, Editor 1992, United States Government Printing Office: Washington D.C., USA.
62. Z. Korunic, *ReviewDiatomaceous earths, a group of natural insecticides.* Journal of Stored Products Research, 1998, 34(2–3), 87.
63. F. Bektas, L. Turanli, and P.J.M. Monteiro, *Use of perlite powder to suppress the alkali–silica reaction.* Cement and Concrete Research, 2005, 35(10), 2014.
64. S.L. James, *Metal-organic frameworks.* Chemical Society Reviews, 2003, 32(5), 276.
65. O.K. Farha, I. Eryazici, N.C. Jeong, B.G. Hauser, C.E. Wilmer, A.A. Sarjeant, R.Q. Snurr, S.T. Nguyen, A.Ö. Yazaydın, and J.T. Hupp, *Metal–Organic Framework Materials with Ultrahigh Surface Areas: Is the Sky the Limit?* Journal of the American Chemical Society, 2012, 134(36), 15016.
66. A.P. Nelson, O.K. Farha, K.L. Mulfort, and J.T. Hupp, *Supercritical Processing as a Route to High Internal Surface Areas and Permanent Microporosity in Metal−Organic Framework Materials.* Journal of the American Chemical Society, 2008, 131(2), 458.
67. R.J. Kuppler, D.J. Timmons, Q.R. Fang, J.R. Li, T.A. Makal, M.D. Young, D. Yuan, D. Zhao, W. Zhuang, and H.C. Zhou, *Potential applications of metal-organic frameworks.* Coordination Chemistry Reviews, 2009, 253(23-24), 3042.
68. S. Dash, S. Mishra, S. Patel, and B.K. Mishra, *Organically modified silica: Synthesis and applications due to its surface interaction with organic molecules.* Advances in Colloid and Interface Science, 2008, 140(2), 77.
69. N. Huesing, U. Schubert, B. Riegel, and W. Kiefer. *Chemical functionalization of silica aerogels*. in *Materials Research Society Symposium - Proceedings*. 1996.
70. C. Yoshina-Ishii, T. Asefa, N. Coombs, M. J. Maclachlan, and G. A. Ozin, *Periodic mesoporous organosilicas, PMOs: fusion of organic and inorganic chemistry 'inside' the channel walls of hexagonal mesoporous silica.* Chemical Communications, 1999(24), 2539.
71. A. Ulman, *Formation and structure of self-assembled monolayers.* Chemical Reviews, 1996, 96(4), 1533.

72. G. Tesoro, *Silane coupling agents, Edwin P. Plueddemann, Plenum, New York, 1982, 235 pp. Price: $37.50.* Journal of Polymer Science: Polymer Letters Edition, 1983, 21(6), 503.

73. F. Schreiber, *Structure and growth of self-assembling monolayers.* Progress in Surface Science, 2000, 65(5-8), 151.

74. P. Van Der Voort and E.F. Vansant, *Silylation of the silica surface. A review.* Journal of Liquid Chromatography and Related Technologies, 1996, 19(17-18), 2723.

75. F. Hoffmann, M. Cornelius, J. Morell, and M. Fröba, *Silica-Based Mesoporous Organic–Inorganic Hybrid Materials.* Angewandte Chemie International Edition, 2006, 45(20), 3216.

76. Y. Wang and M. Lieberman, *Growth of ultrasmooth octadecyltrichlorosilane self-assembled monolayers on SiO2.* Langmuir, 2003, 19(4), 1159.

77. I. Anac and T.J. Mccarthy, *Chemical modification of chromium oxide surfaces using organosilanes.* Journal of Colloid and Interface Science, 2009, 331(1), 138.

78. A.Y. Fadeev and T.J. Mccarthy, *A new route to covalently attached monolayers: Reaction of hydridosilanes with titanium and other metal surfaces [1].* Journal of the American Chemical Society, 1999, 121(51), 12184.

79. C. Domingo, E. Loste, and J. Fraile, *Grafting of trialkoxysilane on the surface of nanoparticles by conventional wet alcoholic and supercritical carbon dioxide deposition methods.* Journal of Supercritical Fluids, 2006, 37(1), 72.

80. D.W. Britt and V. Hlady, *Protonation, hydrolysis, and condensation of mono- and trifunctional silanes at the air/water interface.* Langmuir, 1999, 15(5), 1770.

81. M. Lazghab, K. Saleh, and P. Guigon, *A new solventless process to hydrophobize silica powders in fluidized beds.* AIChE Journal, 2008, 54(4), 897.

82. C.A. Garćia-González, J. Saurina, J.A. Ayllón, and C. Domingo, *Preparation and characterization of surface silanized TiO2 nanoparticles under compressed CO2: Reaction kinetics.* Journal of Physical Chemistry C, 2009, 113(31), 13780.

83. E. Loste, J. Fraile, M.A. Fanovich, G.F. Woerlee, and C. Domingo, *Anhydrous supercritical carbon dioxide method for the controlled silanization of inorganic nanoparticles.* Advanced Materials, 2004, 16(8), 739.

84. C.A. García-González, J. Fraile, A. López-Periago, and C. Domingo, *Preparation of silane-coated TiO2 nanoparticles in supercritical CO2.* Journal of Colloid and Interface Science, 2009, 338(2), 491.

85. W. Gu and C.P. Tripp, *Reaction of Silanes in Supercritical CO2 with TiO2 and Al2O3.* Langmuir, 2006, 22(13), 5748.

86. P. López-Aranguren, J. Saurina, L.F. Vega, and C. Domingo, *Sorption of tryalkoxysilane in low-cost porous silicates using a supercritical CO2 method.* Microporous and Mesoporous Materials, 2012, 148(1), 15.

87. T.S. Zemanian, G.E. Fryxell, J. Liu, S. Mattigod, J.A. Franz, and Z. Nie, *Deposition of self-assembled monolayers in mesoporous silica from supercritical fluids.* Langmuir, 2001, 17(26), 8172.

88. X. Li and Z. Li, *Advances in Construction materials Part IX*. Springer-Berlag, ed. C.U. Grosse2007Berlin, Heidelberg, New York Springer.

89. D. Kumar, K. Schumacher, C. Du Fresne Von Hohenesche, M. Grün, and K.K. Unger, *MCM-41, MCM-48 and related mesoporous adsorbents: their synthesis and characterisation.* Colloids and Surfaces A: Physicochemical and Engineering Aspects, 2001, 187-188, 109.

90. *Advances in Nanoporous Materials*, ed. S. Ernst. Vol. 1. Elsevier.

91. S.A. Kozlova and S.D. Kirik, *Post-synthetic activation of silanol covering in the mesostructured silicate materials MCM-41 and SBA-15.* Microporous and Mesoporous Materials, 2010, 133(1-3), 124.

CHAPTER II

SUPERCRITICAL CO_2: PROPERTIES, APPLICATIONS AND HIGH PRESSURE TECHNOLOGY

This chapter begins with a description of the critical properties of supercritical fluids, giving a special attention to CO_2, as it is fluid used for the experiments performed in this thesis. Moreover, a fundamental study of the properties of supercritical CO_2 confined in porous media is described through the use of a mean field equation of state..The main applications of supercritical fluids are also presented here followed by a description of the high pressure technology necessary to attain supercritical conditions. The high pressure equipments are constituted by several components such the pump, the vessel, tubing and valves, etc., and they are configured for the specific reaction needs. A detailed description of the high pressure equipments used in this work is offered at the end of the chapter.

2.1 INTRODUCTION: PROPERTIES OF SUPERCRITICAL FLUIDS

A fluid is in supercritical conditions when both pressure and temperature are above the critical pressure and temperature (the critical point), in which the liquid and gaseous phases become indistinguishable. In the supercritical region, an isothermal pressure increase above the critical pressure or an isobaric temperature increase above the critical temperature maintains the fluid at supercritical conditions, without phase transition. Fig. 2.1a shows a schematic representation of a pressure-temperature phase diagram of a fluid. The phase diagram shows the regions corresponding to the three states of matter and the triple point, at which the three phases coexist in equilibrium. The diagram also highlights the critical point of the fluid, including the critical values of pressure and temperature for CO_2. CO_2 has a critical temperature (T_c) of 31 °C and a critical pressure (P_c) of 7.4 MPa, being in the supercritical state ($scCO_2$) above these values.

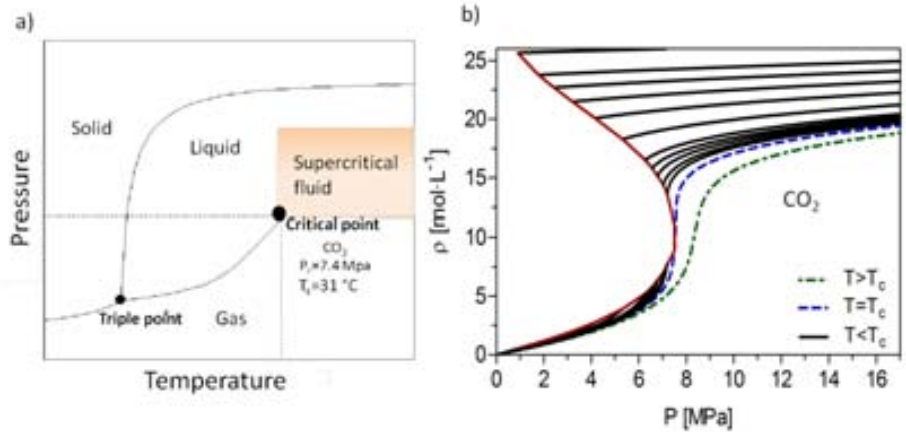

Figure 2.1 Representation of phase diagrams: a) pressure-temperature for a fluid, and b) density-pressure for CO_2. Data has been obtained from NIST thermophysical properties website [1].

Table 2.1 provides the critical point values for several supercritical fluids. In the supercritical region, the physicochemical properties can be tuned with small pressure and temperature variations. $ScCO_2$ is considered a green solvent, as it is non-flammable, is naturally abundant, and has much lower global warming potential (GWP) than any other solvent (apart from water) [2]. Moreover, CO_2 is considered non toxic [3].

Table 2.1 Critical point of some fluids [4].

Fluid	T_c (ºC)	P_c (MPa)
He	-269	0.2
CO_2	31	7.4
C_2H_6	32	4.9
N_2O	37	7.3
C_3H_8	97	4.2
NH_3	132	11
H_2O	374	22

2.1.1 Single phase and tunable density

The possibility to have a single phase and tunable density are among the most relevant thermodynamical properties of supercritical fluids (SCFs). The density(X)-pressure(Y) diagram for CO_2 is represented in Fig. 2.1b [1]. The solid red line represents the coexistence curve line, at which liquid and gas phases are always present. This curve is obtained from all the isotherms below the critical point of CO_2. Above the critical point, the distinction between liquid and vapor phases disappear and a single density phase (dotted curves) is obtained at supercritical conditions. In this region, small changes in pressure or temperature induce great changes in the density of the fluid. For instance, within the temperature range of 31 ºC to 127 ºC, and pressures between 7.4 MPa and 20 MPa, the CO_2 density can be tuned in the range of 2.6 to 20 mol L^{-1}.

A supercritical fluid has both gas- and liquid-like properties (Table 2.2). It behaves as a gas as it is a compressible fluid that fills its container, exhibits low viscosity and shows high diffusivity. It is liquid-like because it has comparable densities and solvating power than some organic low-polarity liquids [5].

Table 2.2 Comparison of some physical characteristic properties of gases, liquids and supercritical fluids.

	Density [g mL^{-1}]	Diffusivity [cm^2 s^{-1}]	Viscosity [g $cm^{-1}s^{-1}$]
Gas	10^{-3}	10^{-1}	10^{-4}
Liquid	1	10^{-6}	10^{-2}
SCF	10^{-1}	10^{-3}	10^{-4}

2.1.2 Negligible surface tension and low viscosity

The surface tension of supercritical fluids is considered almost null (it vanishes at the critical point, and it is very low in the near critical region) and, therefore, it is much lower than that of conventional organic solvents or water exhibiting values in the range of 20-70 mN m^{-1} at 20 ºC. Besides, supercritical fluids exhibit viscosities of *ca.* 100 times lower than those of liquids (Table 2.2).

When working with pore systems at the nanoscale, the use of liquid solvents entails some disadvantages. For instance, when drying gels the surface tension of the solvent induces capillary forces leading to the collapse of the structure. However, if the gel is dried at supercritical conditions, the structure is prevented from collapse thanks to the null surface tension of SCFs. Another example is found on the modification of porous solid surfaces with organic functional molecules, where the diffusion of solutes along the pores is somehow limited by the viscosity of liquid solvents. The use of SCFs enhance the diffusivity of the organic molecules along the pores leading to complete and homogeneous surface coating [6].

2.1.3 Low critical temperature and pressure

An important characteristic that makes $scCO_2$ desirable among other supercritical fluids is related to its low critical temperature and accessible pressure (Table 2.1). The critical pressures of the fluids shown in Table 2.1 are easily achievable with the available technology. However, some of these fluids, such as water (H_2O), require heating at high

temperatures, which can have economical limitations, in terms of energy, in addition to the limitations of the equipments to be used. Other drawbacks are related to the toxicity of the fluid as it occurs for ammonia (NH_3), or to the flammability as occurs for propane (C_3H_8). H_2O is, after CO_2, the second most used fluid for supercritical oxidation, hydrolysis and gasification processes [7]. The use of water in supercritical conditions involves highly oxidizing medium which entails corrosion of the high pressure components.

Pressure is divided into four ranges: low, up to 103.5 MPa; medium, up to 138.0 MPa; high, up to 413.5 MPa, and ultra high, up to 1034 MPa [8]. According to this, CO_2 exhibits a low critical pressure, besides a close to room temperature critical temperature. The low critical temperature of CO_2 represents a clear advantage when working with thermally labile materials, as for instance pharmaceutical or natural compounds.

2.1.4 Green solvent

Solvents define a major part of the environmental performance of processes in chemical industry, and also its use impacts on cost, safety and health issues. The idea of "green" solvents expresses the goal to minimize the environmental impact resulting from the use of solvents in chemical production [9]. Volatile organic liquid solvents applied for the synthesis of materials are generally used in large amounts during the synthesis and washing steps. Most of them have a high toxicity, are flammable and the residues may be environmentally difficult to eliminate. $ScCO_2$ represents an environmental friendly alternative to replace organic solvents. It is considered a green solvent because it has a very low toxicity, it is nonflammable, it has a lower GWP compared to the organic solvents it is replacing, and it is relatively inert. Moreover, in contrast to the materials processed using liquid solvents, which usually requires a washing step to remove solvent traces and unreacted species, the final products obtained by $scCO_2$ processing do not require to be dried, because at the end of the process CO_2 is released as a gas.

2.1.5 Solvent properties of $scCO_2$

Carbon dioxide exhibits some solvent properties due to the presence of a quadrupole moment in the molecule. The solvent capacity of $scCO_2$ is comparable to that of n-hexane. Hence, nonpolar or low molecular weight molecules easily dissolve in $scCO_2$, whereas polar or high molecular weight molecules have very low solubilities [10]. The only polymers shown to have a significant solubility in $scCO_2$ under mild conditions of pressure and temperature are certain amorphous fluoropolymers and silicones [11]. Some light organic compounds, such as methanol, acetone and ethanol, are used as cosolvents (also called modifiers) to enhance the solvating power of carbon dioxide.

2.1.6 Production of CO_2

Besides being a green solvent, another advantage that promotes the use of carbon dioxide is its natural occurrence and abundance. It can be found in natural reservoirs with a high purity or obtained after purification from fossil fuels burning, in pre-combustion by reacting carbon matter with O_2 and in post-combustion by separation of the CO_2 from flue gas. It can also be obtained as a byproduct from some industrial processes, like in the production of NH_3, hydrogen (H_2) and ethanol (CH_3CH_2OH) [12].

2.2 STUDY OF THE DENSITY ENHANCEMENT ON CONFINED SUPERCRITICAL CO_2 USING AN EQUATION OF STATE

When a fluid is confined in a porous matrix (Fig. 2.2) its properties relative to its bulk state are shifted and this may be important in engineering applications. The magnitude of this change depends on the pore size, geometry and the nature of the fluid-surface interaction.

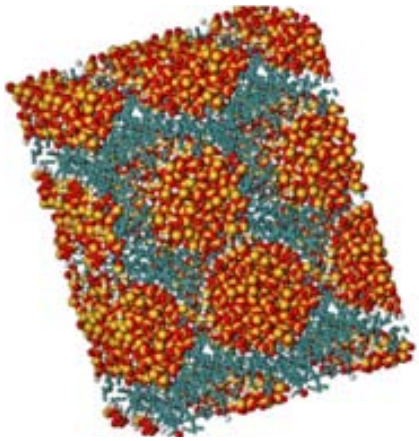

Figure 2.2 Illustration of CO_2 gas molecules confined into a silica gel structure.

The effect of confinement on the criticality of fluids in controlled-pore materials with narrow size distribution has been studied, indicating a shift of the gas-liquid critical point of the fluid in the porous material to lower temperature. However, the situation is different in amorphous mesoporous materials such as silica aerogel. Due to the wide pore-size distribution and ill-defined pore geometry, it has not been possible to establish a quantitative description of the critical point shift [13, 14]. Given this situation, there has been substantial effort over the years devoted to developing equations of state suitable for thermodynamic property predictions in fluids confined in porous media, nevertheless, tractable, physically based models have remained elusive [15]. In this thesis, a mean field and analytical equation of state (Eq. 2.1) was used to predict the density of pore-confined CO_2. An equation of state is a formula describing the interconnection between various macroscopically measurable properties of a system. This equation only requires the pure fluid critical properties to predict properties of bulk pure fluids and it can be extended for calculating thermodynamic properties of pore-confined fluids by considering the fluid-fluid and the fluid-matrix parameters as well of a series of transformation factors between the model and the real fluid of interest. The theoretical underpinnings of the equation of state can be found elsewhere [16].

$$(2\rho - 1) = (1 - zp)\tanh\left[\beta'(2z\rho + \mu'/2)\right] + zp\tanh\left[\beta'(2\rho(z-1) + \tfrac{1}{2}\Gamma' + \mu'/2)\right] \qquad 2.1$$

where p is the porosity, ρ is the density, μ is the chemical potential, □ and r are the fluid-fluid and the fluid-solid coupling parameters, respectively, β is a temperature dependent constant and the superscript " ' " denotes a dimensionless property.

In Fig. 2.3 theoretical results are shown for carbon dioxide at the critical temperature in a confined system and varying the porosity from 80 to 90 %. Large enhancements in density are seen especially in the critical region. Moreover, there are large decreases in the predicted critical pressure values for the confined system.

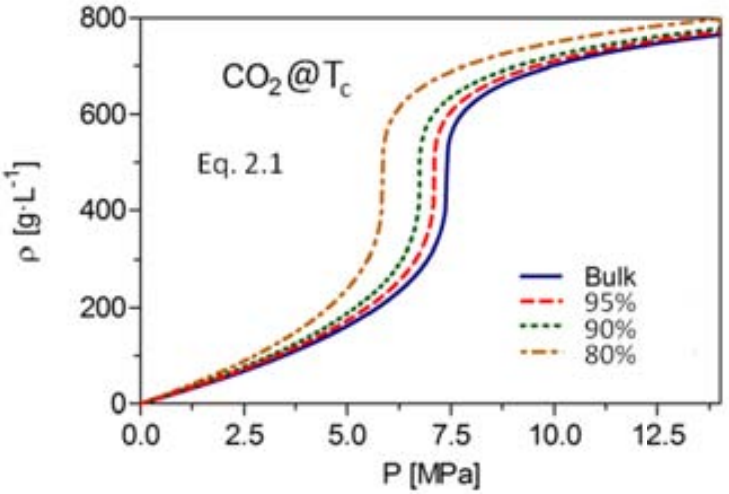

Figure 2.3 Adsorption isotherms at the critical temperature of confined CO_2 at three different porsities compared to bulk density.

The model was fitted to recently published data [17] for carbon dioxide adsorbed in a silica aerogel. The results are presented in Fig. 2.4 for various values of porosity at a temperature of 35 ºC with the model providing a particularly good fit in the transition region using a porosity of 95 % (authors report a porosity of over 90 %). Furthermore, model predictions of density enhancements at other conditions for which experimental data are unavailable are also shown. These show large pressure shifts and density enhancements, demonstrating the value of having a theoretical equation of state model available for such purposes.

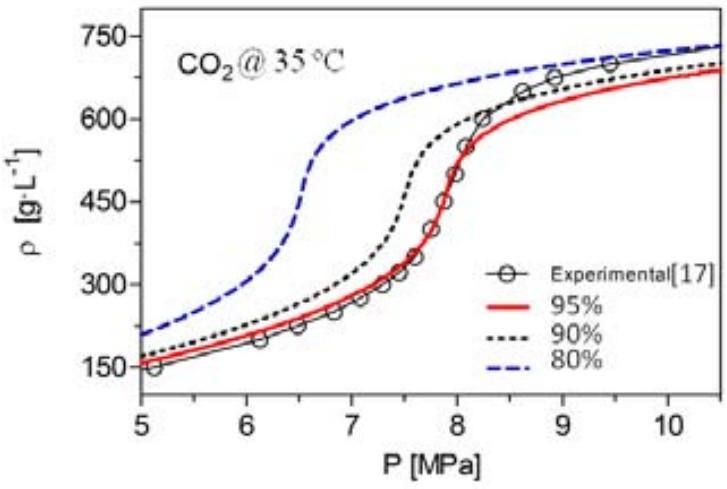

Figure 2 .4 Adsorption isotherms of confined CO_2 adjusted to an experimental temperature of 35º C at three different porosities compared to the experimental adsorption of CO_2 on silica aerogel [17].

2.3 APPLICATIONS OF SUPERCRITICAL CO_2

Carbon dioxide (CO_2) is a valuable compound applied in the gas state in several industrial processes as a reactant, f.i., in the production of urea to manufacture fertilizers or in the mineral carbonation for the preparation of precipitated calcium carbonate ($CaCO_3$). It is also used in refrigeration, food packaging, beverages, wastewater treatment for pH control, oil recovery and as a fire extinguisher [18]. $ScCO_2$ is used in a range of industrial processes, such as in the extraction of organic components (f.i., coffee decaffeination), in the fractionation of liquid mixtures, in polymer processing, for paint and coating, in particle formation for pharmaceutical and cosmetic industries and in textile dying [6, 18-20]. $ScCO_2$ is also an ideal candidate for the synthesis and processing of porous materials [21], being the most convenient or an alternative route to the use of liquid solvents. For instance, gels drying to obtain aerogels are only possible using supercritical conditions. Another example is the surface modification of nanoporous materials with organic molecules, where the use of organic solvents have limitations related to the diffusion of the

solute molecules due to viscosity and high surface tension [21]. Processes using $scCO_2$ can be performed at the laboratory scale, such as its use as mobile phase in chromatography for separation purposes [22, 23], assistance in particle design and size control or in the modification of porous supports using impregnating agents [24]. Industrial applications of $scCO_2$ include the extraction of valuable compounds (e.g. caffeine, spices, etc. [25], pharmaceutical and nutraceutical active agents [26]), its use as a reagent in the preparation of rigid thermoplastics or as a solute in polymer foaming [27]. Supercritical carbon dioxide has been used for the last thirty years for enhance oil recovery in oil fields [28-30].

2.3.1 Extraction of organic compounds

Supercritical fluid extraction of organic compounds is the most widely studied application of $scCO_2$ [11]. A scheme of a general extraction equipment is depicted in Fig. 2.5. The extractor vessel is charged with the raw material to be extracted. $ScCO_2$ flows through the vessel and the extracted compound is separated from the CO_2 at the separator vessel. The CO_2 released is introduced again into the process. Among the industrial companies performing supercritical fluid extractions, stand out FLAVEX (Germany) [31], devoted to the extraction of balm leaf, cinnamon, coriander, ginger and rosemary and Phasex (USA) [32], dedicated to the extraction of carotenoids. Others such as MedWest (USA) [33] use $scCO_2$ to extract cannabis oil and to decaffeinate coffee. Germany is the country with the highest capacity to extract caffeine (160.000 tonnes) from coffee beans using supercritical CO_2. An example is the HAG Company (Germany), extracting caffeine since 1979 [34]. The Spanish company DIAM Corchos S.A., Corchos de Mérida (with French technology), is the largest company using $scCO_2$ to eliminate trichloroanisole from cork [35].

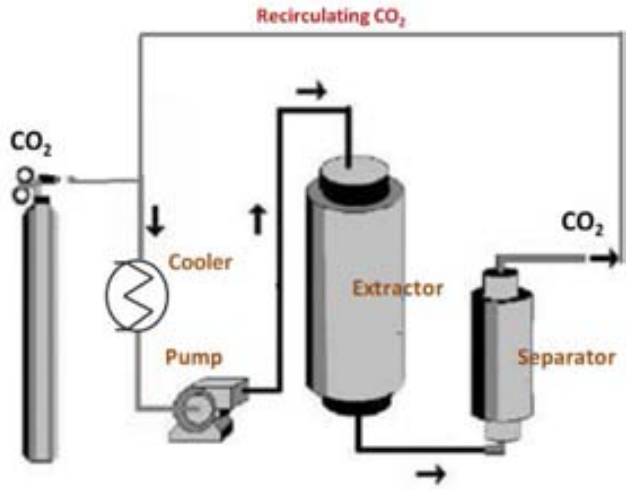

Figure 2.5 Representation of a high pressure extraction equipment.

2.3.2 Mobile phase in chromatography

Nowadays, the use of $scCO_2$ in chromatography is applied for separation of complex chemical mixtures into individual components rather than as an analytical tool. Separation in supercritical fluid chromatography is based on the solvating power of the $scCO_2$. In contrast to liquid chromatography, the separation is faster, because of greater diffusion of solutes in supercritical fluids than in liquids (Table 2.2). Supercritical fluid chromatography finds use in the pharmaceutical industry, f.i., in the separation of chiral molecules, and for purification processes [14].

2.3.3 Supercritical carbon dioxide applied to polymers

Supercritical carbon dioxide is used as an alternative to traditional solvents for polymer synthesis, such as the production of high molecular weight fluoropolymers, polycarbonates and polyethers [36], and also for purification, impregnation and dyeing processes. Most of polymer processing is based on the plasticization effect that occurs when CO_2 is substantially dissolved in the polymer [36, 37]. This leads to a decrease in the polymer glass transition temperature (T_g). For example, the T_g of polystyrene is reduced by 50 ºC

under a CO_2 pressure of 2.5 MPa. CO_2 is also used as a foaming agent for the preparation of biocompatible and biodegradable polymer foams for biomedical applications [38]. Dyecoo Textile Systems B.V. (The Netherlands) performs a waterfree textile dyeing of synthetic polymers using CO_2 [39] .

2.3.4 Supercritical CO_2 in the preparation of micro- and nanoparticles

Supercritical CO_2 is largely applied in the preparation and design of micro and nanoparticles, fibers and thin films with successful results. The CO_2 technology takes advantage of the $scCO_2$ properties converting this fluid in an ideal non damaging solvent for nanostructures. There are a vast number of technical processes used to produce particles, where $scCO_2$ is applied either as a solvent, as an antisolvent or as solute [40].

Some of the most common techniques are:

i) Rapid Expansion of Supercritical Solutions (*RESS):* $scCO_2$ is used as a solvent. The solute is dissolved in a compressed fluid and rapidly depressurized through a nozzle, resulting in the precipitation of small size and monodisperse particles (Fig.2.6a). The RESS process is used to dissolve an active substance and the coating material in the supercritical fluid, and then co-precipitate both substances. The main limitation of RESS techniques is the low solubility of many substances in $scCO_2$.

ii) Gas/Supercritical Anti-Solvent (GAS/SAS) and Precipitation with a Compressed Antisolvent (PCA): all of these processes rely on reducing the density and solvating power of an organic solvent, in which the solute is dissolved, by mixing it with compressed CO_2 used as an antisolvent (Fig. 2.6b and c).

iii) Particles from Gas Saturated Solutions (PGSS): $scCO_2$ is used as a solute dissolved in amorphous or semicrystalline high molecular weight materials (e.g., polymers and solid lipids) (Figure 2.7d). The pressurized gas diffuses into the product, lowering both the product melting point and the mixture viscosity. This process produces particles by

spraying the mixture *via* a nozzle. The process has been demonstrated on a large scale, but it is only applicable to produce micrometric particles.

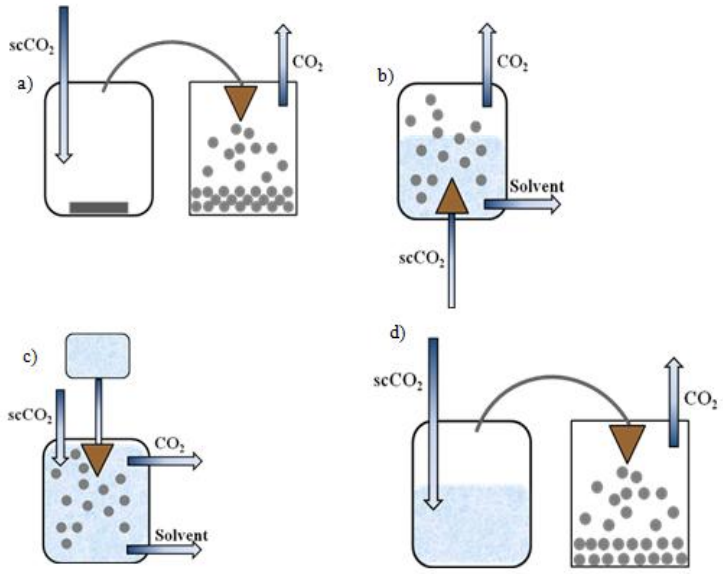

Figure 2.6 $ScCO_2$ spray precipitation techniques: a) RESS, b) GAS/SAS, c) PCA, and d) PGSS.

2.3.5 Processing and modifying porous materials in supercritical CO_2

The use of $scCO_2$ entails a series of benefits in the synthesis and processing of porous materials in front of the use of conventional organic solvents [21]. $ScCO_2$ allows rapid mass transfer of solute molecules and improve the wetting of surfaces with intricate geometries. $ScCO_2$ is used for the impregnation of nanoporous systems (e.g., particles, polymers) with active compounds for drug-delivery purposes [41-43] and for the fabrication of functional materials through surface modification with organic compounds [44-47].

2.4 HIGH PRESSURE EQUIPMENTS: HIGH PRESSURE EQUIPMENT MATERIALS AND ELEMENTS

The use of supercritical fluids necessarily requires high pressure equipment able to stand the operating conditions. The design and selection of the equipment must be done considering the thermophysical properties, i.e., T_c and P_c, of the fluid. It is also necessary to pay special attention to other aspects, such as the chemical nature of the supercritical fluid and the type of processing to be performed (e.g., extraction, chemical reaction, precipitation, etc) in either batch or continuous mode.

$ScCO_2$ is the most used supercritical fluid and, therefore, most of the high pressure equipment available are designed for its use. There are a number of international companies providing engineering components and systems for gas and fluid applications. For instance, Parker (USA) [48] and HiP (USA) [49] offer a diversity of engineering products such as valves, tubes and fittings, reactors and pressure vessels, pumps and gas boosters, etc. Autoclave Engineers (USA) [8] offers a bench of laboratory high pressure vessels and stirred reactors besides other high pressure elements. There are a number of companies in china, such as Tawian Supercritical Technology [50] providing supercritical fluid components. Separex (France) [51] proposes process and product development services using supercritical technology. It also designs and builds high pressure systems and components for lab and for production scale. A similar company, GITSU Greentech, has been recently created in Spain.

Thar Process (USA) [52] is a company providing supercritical fluid technology and equipment design focused on extraction and separation processes at laboratory and plant scale. Swagelok (USA) [53] is well known for the fabrication of connectors for high and low pressure stainless steel tubing. Chematur technologies (USA) [54] provides engineering services for process plants. Natex (Austria) [55] is a company that tests processes at lab unit and then scale-up is carried out to determine yields and process parameters for industrial operation.

The equipment building materials and elements for SCFs applications are described next.

2.4.1 Materials

A high pressure equipment is constituted by several elements: the reactor vessel, the high pressure pump, tubing, valves and fittings, cooler, controllers, pressure and temperature measurement devices and pressure safety elements. Stainless steel AISI-316 is the common material applied in the manufacturing of those components subjected to $scCO_2$ conditions. This steel alloy contains carbon, chromium, nickel and molybdenum on its composition. Other stainless steel alloys are employed depending on the corrosive environment generated by the supercritical fluid. For instance, supercritical water generates an extremely oxidation environment that degrades rapidly stainless steel vessel walls, junctions and pipes. For supercritical water purposes, there are special materials based on iron doped with Cr, ceramics, titanium- and nickel-base alloys [56].

2.4.2 Vessels and sealing systems

The reactor vessel is where the supercritical fluid is brought into contact with the material to be processed. This element is selected according to its size, closure style, stirring and heating systems. The closure type of a vessel mostly defines its pressure and temperature limits. Therefore, the closure type is chosen depending on the working conditions, the seal compatibility and the frequency and ease of opening/closing. For instance, Autoclave Engineers [57] offers quick opening and closing systems such as Zipperclave® with a quick o-ring seal (Fig. 2.7a). Polymeric materials for o-rings are Viton®, silicone, ethylene propylene rubber, Kalrez®, etc., having different pressure and temperature limits and different resistances to organic solvents. Other closure systems from Autoclave Engineers are the EZE-Seal® (Fig. 2.7b), designed for high temperatures and moderate pressures, and the Bolted Closure system (Fig. 2.7c) designed to work at up to 37.9 MPa, and high temperatures. Another common sealing system is the energized spring seal (Fig. 2.7d) patented by Thar Process [58]. These seals are based on a polymeric

material with an internal energizing spring. When the pressure increases, the spring creates a highly efficient seal against the mating surface.

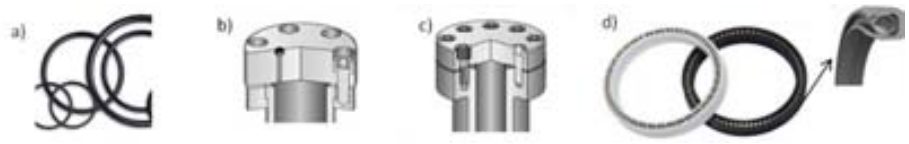

Figure 2.7 Different seals and closure systems: a) o-ring, b) EZE-S, c) bolted-closure, and d) energized spring.

2.4.3 Stirring mechanism and impeller types

The stirring mechanism has a direct influence on the fluid motion and mixing degree. The agitation flow pattern in a vessel can be easily attained by means of a horizontal stir bar and a magnetic stirrer (Fig. 2.8). Some reactors incorporate a more robust system based on a vertical impeller shaft. The impeller can be driven through a standard belt drive moved by an electric motor or by a magnetic mechanism. MagneDrive® technology is an example of vertical stirrers that applies magnets to rotate the agitator shaft [59].

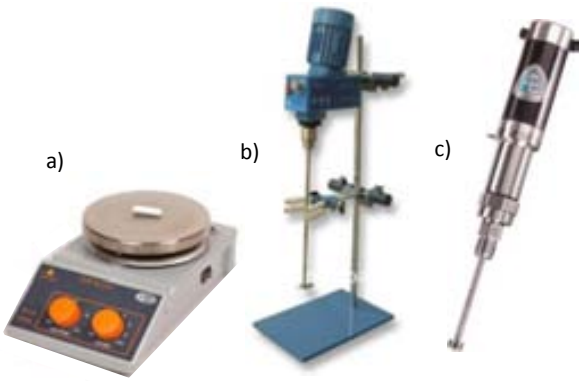

Figure 2.8 Agitation systems: (a) horizontal magnetic bar stirrer, (b) mechanically rotated impeller shaft and (c) the high pressure magnetic stirrer Magnedrive®.

2.4.4 Pressure pumps

When working with supercritical fluids, it becomes necessary to pressurize the gas. The best option is the use of pressure pumps, which allows pressurizing up to the chosen pressure with high accuracy. The fluid, supplied from a deep-tube CO_2 gas bottle at *ca.* 60 bar, is first cooled with the aid of a chiller or cryostat to maintain its liquid state and to avoid cavitation. Pumping systems applied for $scCO_2$ technology include reciprocating, syringe and membrane pumps:

i) Reciprocating piston pumps (Fig. 2.9a): the term reciprocating describes the continuously repeated backwards and forwards motion of the piston. Reciprocating piston pumps used in supercritical processes are mostly of the dual head type. In this way, the flow becomes continuous and almost pulseless. Thar Technologies manufactures and commercialize this type of pumps for $scCO_2$ [52].

ii) Syringe pump (Fig. 2.9b): a motor drives the syringe piston to control the outlet pressure of the pump. Teledyne Isco (USA) fabricates efficient high pressure syringe pumps [60].

iii) Membrane or diaphragm pump (Fig. 2.9c): these are accurate flow pumps based on a reciprocating movement, where the piston is replaced by a diaphragm or membrane. The use of these pumps for supercritical fluids have some advantages as they do not have mechanical seals which are the main breaking cause. Membranes are highly resistant to corrosion, as they are made of neoprene, viton, teflon or polyurethane. Lewa (Germany) [61] manufactures several types of high pressure pumps including diaphragm pumps.

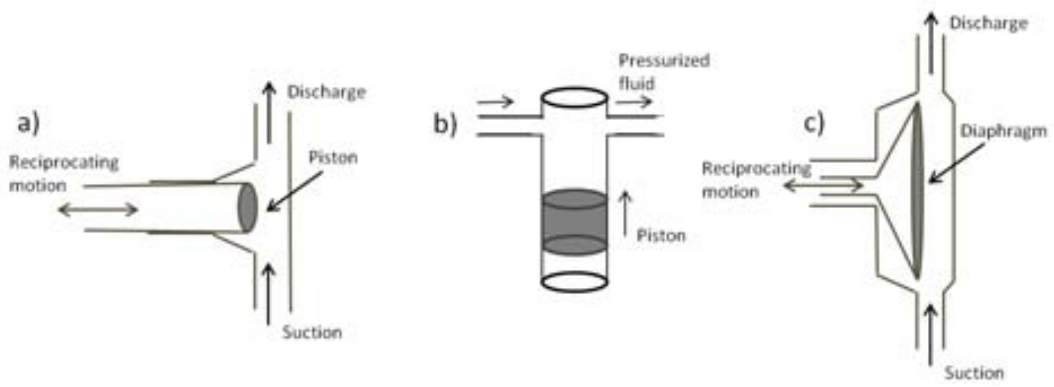

Figure 2.9 Representation of the different types of pumps: a) reciprocating, b) syringe, and b) membrane pump.

2.4.5 High pressure tubing and valves

High pressure tubing is used to transport the gas to the different high pressure equipment components. Typical tubing sizes are 1/16", 1/8", 1/4", 3/8", 9/16" and 1-1/2". Tubes with similar or different diameters can be connected through different devices. For instance A-LOK® tube fittings are connections that used ifferent ferrules for the assemblies. Quick fit couplings are pneumatic coupling devices used to connect and/or disconnect tubes quickly and easily without the use of tools. Gas flow between the components is controlled through valves. Common valves applied in high pressure equipments are needle, ball, non-return and pressure release valves. While needle valves (Fig. 2.10a) are used when a precise control in the flow rate is needed, ball valves (Fig. 2.10b) only have two fix positions and are used to allow or stop the gas flow. Non-return or check valves (Fig. 2.10c) are applied to allow the gas flow in a single direction. Pressure release valves (Fig. 2.10d) are devices that allow the fluid to flow from an auxiliary passage out of the system to avoid overpressures. They are designed or set to open at a predetermined pressure.

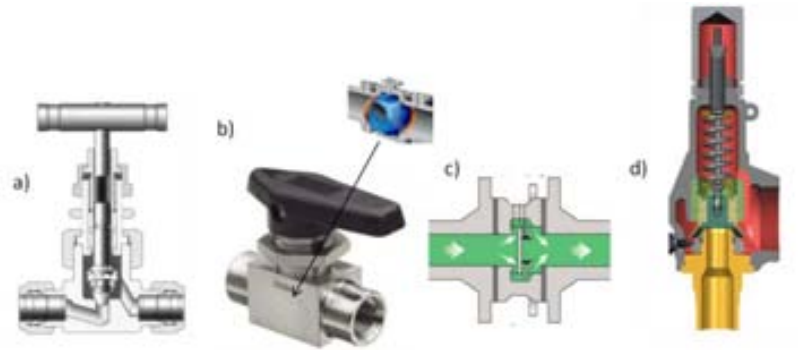

Figure 2.10 Common valves used in supercritical fluid equipment: a) needle, b) ball, c) non-return and d) pressure release valves.

2.4.6 Pressure and flow measurement devices

The fluid movement can be measured in a variety of ways. For instance, positive flow meters accumulate a fixed volume of fluid and then count the number of times the volume is filled to measure the flow. Other methods rely on the forces produced by the flowing stream as it overcomes a known constriction. The pressure can be measured by many instruments, being the manometer the most common one. The manometer uses a column of liquid to measure the pressure. More modern instruments are electronic pressure sensors based on the piezoelectric effect. The pressure transducer is the device used to convert the pressure into an analog electrical signal. Coriolis are flow meters built from parallel curved tubes where the fluid circulates through. When there is a mass flow it induces a vibration in the tubes that is translated into a mass flow measurement. Other coriolis devices use rotating tubes that twist slightly when the fluid is flowing through the tubes.

2.4.7 Heating systems

In general, supercritical processes require heating. A simple heating system can be a hot plate, although there are more sophisticated systems, such as internal heating resistances or band heaters, which allow a more homogenous and precise heat distribution. Usually, the vessel incorporates a thermocouple probe coupled with a proportional-integral-derivative controller (PID) to accurately control the temperature.

2.4.8 Pressure release systems

Safety precautions must be taken when working with high pressure systems. Release devices such as rupture disks or safety release valves are located in those spaces of the high pressure equipment where the gas is confined and pressurized [62].

2.5 HIGH PRESSURE SYSTEMS USED IN THIS WORK

The experiments using compressed CO_2 were carried out in three different reactors. A similar configuration was used for the three vessels, with the main differences being the type of pump and the pressure controller used. Fig. 2.11 shows the process flow diagram of the high pressure equipment.

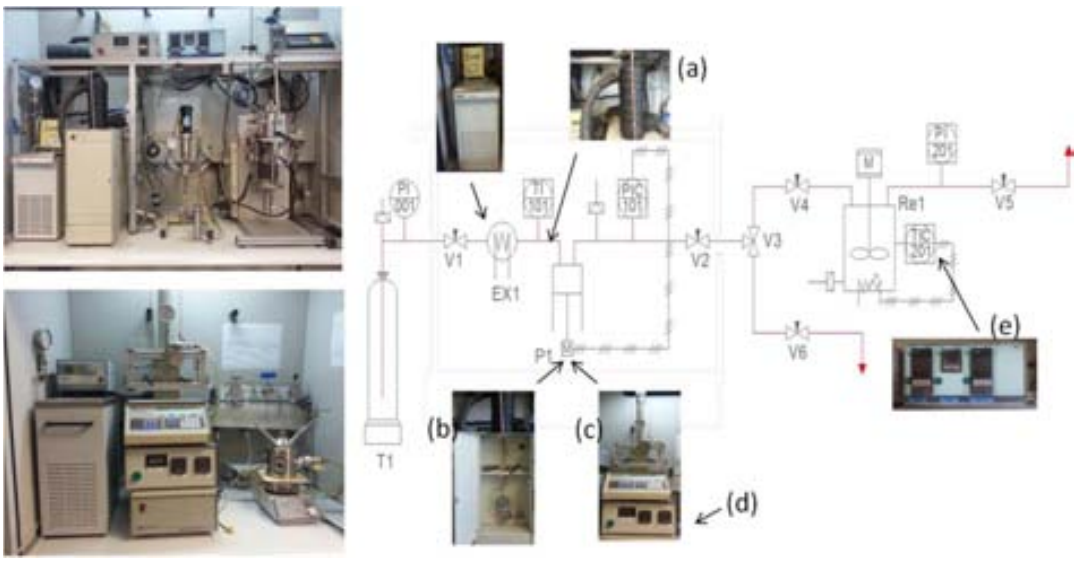

Figure 2.11 Process flow diagram of the high pressure equipment used.

All the elements on the equipment were connected through 316 stainless steel 1/4" pipes. T1 represents the CO_2 bottle supply. A cooling bath (EX1, Laud a Ecoline

Staredition RE106) containing poly(ethylene glycol) was used for cooling the CO_2. A pipe-jacket (a) was used to isolate the cooling area to provide an efficient chilling before CO_2 was pressurized. A rupture disk (Oseco, 12.9 MPa @ 22.2 ºC) was placed in the line between the supply bottle and valve V1. An inconel rupture disk (Ficker, 51 MPa @ 22.2 ºC) was placed between valves V1 and V2 (HiP).V1 and V2 are, respectively, the inlet and outlet valves of the pump. The equipment configuration allows to working with two different pumps (P1):

- a 240 mL syringe pump module (Thar Designs SP240) (b) controlled through a computer.
- a 260 mL syringe pump module (Teledyne Isco Model 260D) (c) controlled through a Teledyne Isco Pump Controller device (d).

Needle valves V2, V3 and V5 (HiP) controlled the CO_2 flow to the vessel system.

The three reactor vessels used in this work are:

i) A 100 mL tubular Minireactor (Autoclave Engineers) (Fig. 2.12a), suitable for applications where a relatively high temperature is required. The closing up mechanism, containing a self sealing O-ring, is designed to work at pressures below 20 MPa and high temperatures. Teflon and viton o-rings, with maximum working temperatures of 204 and 232 ºC, respectively, were used for the experiments performed in this autoclave. The vessel is equipped with an in-line Magnedrive III (Fig. 2.12a), which is a high speed rotary stirring mechanism with a straight blade turbine agitator (Fig. 2.12b). An inconel rupture disk (Oseco, 20 MPa @ 22.2 ºC) was placed in the body of the vessel. A heating band (Fig. 2.11, Re1) controlled by a PID device (Eng&Tech) was used to heat the vessel to the desired temperature (Fig. 2.11e).

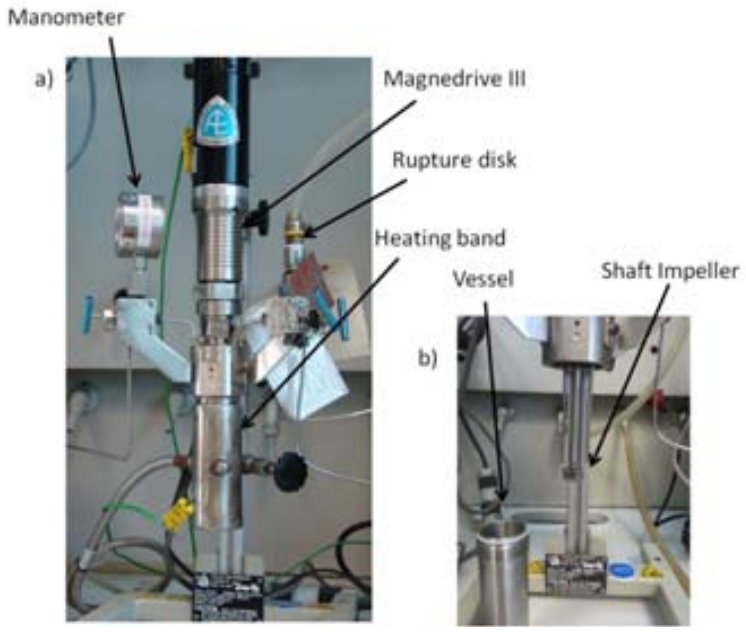

Figure 2 .12 (a) High pre ssure tubul ar minireactor of 100 m L (Autoclave Engineers), and (b) detailed view of the vessel and the shaft impeller

Two thermocouples (K type) located inside of the vessel and in the metallic heating jacket allowed the control of both internal and external temperatures. The pressure attained in the vessel was analogically read through a manometer (Fig. 2.11, P1). The reactor can be coupled to a two stage oil rotatory vacuum pump (Edwards, E2 M0.7, 0.3 Pa) (Fig. 2.12c) connected through valve V5 (Fig 2.11). This pump is used to eliminate residual water or other solvents from the reactor when necessary.

ii) The second used reactor is the 100 mL high pressure autoclave (ThaDesign) shown in Fig. 2.13. The vessel is equipped with two single-crystal sapphire windows (LG-201, 7/8" diameter) placed 180º apart in the reactor body to allow a visual inspection of the experiments. An inconel rupture disk (HiP, 70.1 MPa @ 22.2 ºC) was placed in the body vessel for safety precautions. The heating mechanism on this vessel is based on four resistance heaters placed in four cylindrical cavities made inside of the reactor wall (Fig. 2.14). The agitation on this reactor was attained by using an stir bar. An stainless steel

support was designed and constructed to place the solid samples into the vessel avoiding contact with liquids when they are added at the bottom of the reactor.

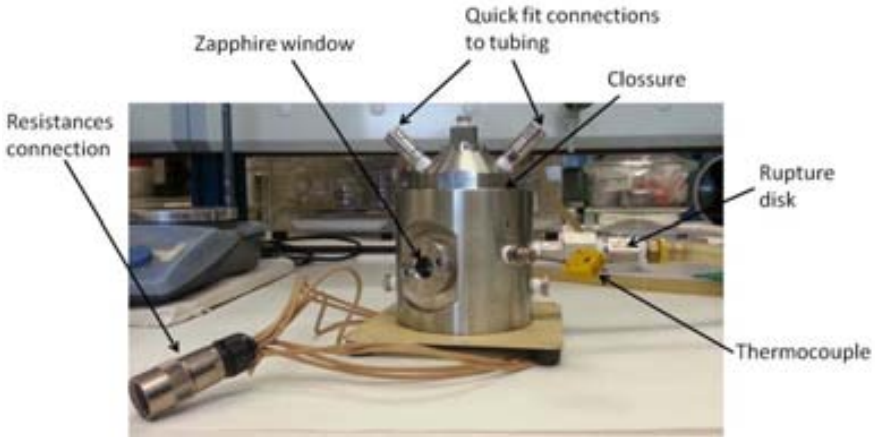

Figure 2.13 Schematic representation of the high pressure reactor from TharDesign.

iii) The third high pressure vessel, depicted in Fig 2.14, is a variable-volume cell (Phase Equilibrium Analyzer, Thar Technologies) used to analyze the phase behavior of solutes in supercritical CO_2. This system was designed to measure the solubility of liquids or solids in supercritical CO_2. An special characteristic of this reactor is the hydraulic hand pump that allows to increase or release pressure from the system by varying the vessel volume from 5 mL to 15.5 mL, while keeping constant the amount of gas, and thus of solute, on the vessel. The vessel was operated with the Thar Design SP240 pump. The vessel is equipped with a rupture disc protection with a pressure limit of 41.4 MPa at 150 °C. The cell includes two zapphire windows to adapt a digital camera to record the phase changes occurring in the vessel and to light up the cell.

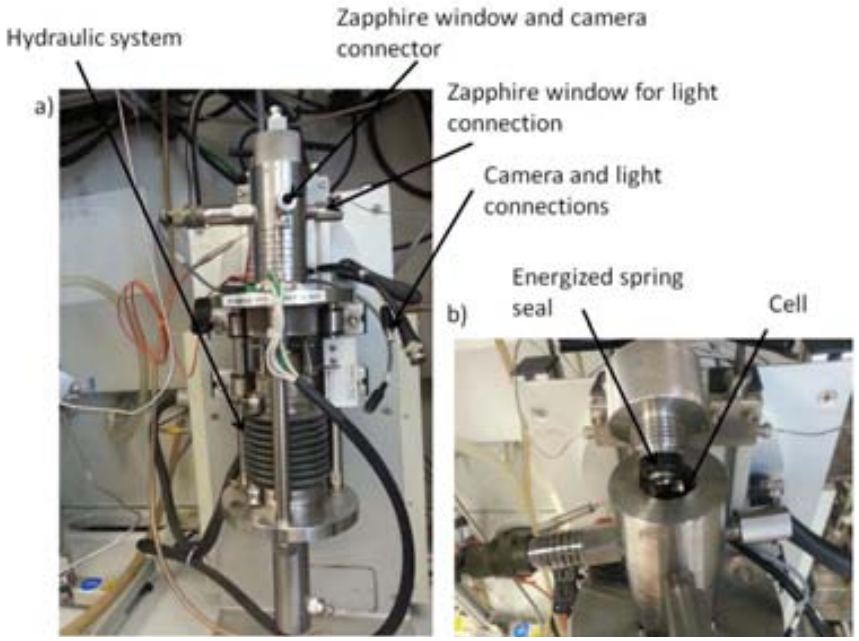

Figure 2.14 Schematic representation of the phase equilibrium analyzer from TharDesign: (a) the whole equipment including the hydraulic system, and (b) detailed view of the cell.

2.5 CONCLUSIONS

The properties of supercritical CO_2 were reviewed and it was illustrated the enhancement on the density of CO_2 confined in porous media by using a mean field equation of state. The properties of $scCO_2$ represent an advantage for a bench of applications, such as extractions, chromatography, polymerizations, synthesis of nanoparticles and the functionalization of porous materials with organic molecules. High pressure technology is required to perform such processes in $scCO_2$. High pressure equipments and specially the vessel are designed with specific characteristics for the process to carry out. In this thesis, three high pressure equipments were used for the experiments performed, which are described in chapter III. Among them, the variable-volume cell was designed to measure the solubility of liquids or solids in supercritical CO_2 while the tubular and the sapphire window vessels, both with a volume of 100 mL were designed to perform experiments in batch mode.

2.6 REFERENCES

1. M.M.O. Lemmon E.W., Friend D.G., *NIST Chemistry Web-Book, NIST Standad Reference Database Number 69*. Thermophysical Properties of Fluid Systems ed. M.W.G. Linstrom P.J.2001National Institute of Standards and Technology, Gaithersburg MD.
2. I.P.O.C. Change. Available from: http://www.ipcc.ch/publications_and_data/ar4/wg1/en/ch2s2-10-3-2.html.
3. C.J. Lambertsen, *Carbon Dioxide Tolerance and Toxicity*, in *Environmental Biomedical Stress Data Center*1971, Universty of Pennsylvania Medical Center: Philadelphia, PA.
4. J.-J.S. Ram B. Gupta, *Solubility in Supercritical Carbon Dioxide*2007: CRC Press.
5. J.R.D. S.M. Hitchen, *Applications of Supercritical Fluids in Industrial Analysis* ed. S.S.B.M. Dordrecht1993.
6. E.J. Beckman, *Supercritical and near-critical CO2 in green chemical synthesis and processing.* Journal of Supercritical Fluids, 2004, 28(2-3), 121.
7. R.W. Shaw, T.B. Brill, A.A. Clifford, C.A. Eckert, and E. Ulrich Franck, *Supercritical water a medium for chemistry.* Chemical and Engineering News, 1991, 69(51), 26.
8. P.A. Engineers. Available from: http://www.autoclave.com/.
9. C. Capello, U. Fischer, and K. Hungerbuhler, *What is a green solvent? A comprehensive framework for the environmental assessment of solvents.* Green Chemistry, 2007, 9(9), 927.
10. Ram B. Gupta and J.-J. Shim, *Solubility in Supercritical Carbon Dioxide*, ed. C. Press2007.
11. E. Reverchon and I. De Marco, *Supercritical fluid extraction and fractionation of natural matter.* Journal of Supercritical Fluids, 2006, 38(2), 146.
12. T.C.W. P.T. Anastas, *Green Chemistry: Theory and Practice*, ed. O.U. Press2002New York.
13. A.P.Y. Wong, S.B. Kim, W.I. Goldburg, and M.H.W. Chan, *Phase separation, density fluctuation, and critical dynamics of N_2 in aerogel.* Physical Review Letters, 1993, 70(7), 954.
14. A.P.Y. Wong and M.H.W. Chan, *Liquid-vapor critical point of ^{4}He in aerogel.* Physical Review Letters, 1990, 65(20), 2567.
15. D.D. Duong, *Adsorption analysis: equilibria and kinetics*1998: Imperial College Press.
16. P. López-Aranguren, L.F. Vega, C. Domingo, and E.H. Chimowitz, *An equation of state for pore-confined fluids.* AIChE Journal, 2012, 58(11), 3597.
17. M.S. Gruszkiewicz, D.J. Wesolowski, and D.R. Cole, *Thermophysical properties of pore-confined supercritical carbon dioxide by vibrating tube densitometry.* Proceedings of the Thirty-Sixth Workshop of Geothermal Reservior Engineering, Stanford University, Stanford, California, 2011.
18. R. Pierantozzi, *Carbon Dioxide*, in *Kirk-Othmer Encyclopedia of Chemical Technology*,2000, John Wiley & Sons, Inc.
19. E. Ramsey, Q. Sun, Z. Zhang, C. Zhang, and W. Gou, *Mini-Review: Green sustainable processes using supercritical fluid carbon dioxide.* Journal of Environmental Sciences, 2009, 21(6), 720.

20. M. Perrut, *Supercritical Fluid Applications: Industrial Developments and Economic Issues.* Industrial & Engineering Chemistry Research, 2000, 39(12), 4531.
21. A.I. Cooper, *Porous Materials and Supercritical Fluids.* Advanced Materials, 2003, 15(13), 1049.
22. G. Gübitz and M.G. Schmid, *Chiral separation by chromatographic and electromigration techniques. A review.* Biopharmaceutics and Drug Disposition, 2001, 22(7-8), 291.
23. R.M. Smith, *Supercritical fluids in separation science - The dreams, the reality and the future.* Journal of Chromatography A, 1999, 856(1-2), 83.
24. C. Magnan, C. Bazan, F. Charbit, J. Joachim, and G. Charbit, *Impregnation of porous supports with active substances by means of supercritical fluids*, 1996. p. 509.
25. H. Içen and M. Gürü, *Extraction of caffeine from tea stalk and fiber wastes using supercritical carbon dioxide.* Journal of Supercritical Fluids, 2009, 50(3), 225.
26. E. Reverchon and R. Adami, *Nanomaterials and supercritical fluids.* Journal of Supercritical Fluids, 2006, 37(1), 1.
27. D.L. Tomasko, H. Li, D. Liu, X. Han, M.J. Wingert, L.J. Lee, and K.W. Koelling, *A Review of CO2 Applications in the Processing of Polymers.* Industrial and Engineering Chemistry Research, 2003, 42(25), 6431.
28. G.C. Institute, *CO2 for use in enhanced oil recovery (EOR)*, 2012, Global CCS Institute.
29. C. Aurel, *Applied Enhanced Oil Recovery*, ed. P. Hall1992.
30. A. Amarnath, *Enhanced Oil Recovery Scoping Study*, 1999, Electric Power Research Institute California, USA.
31. Flavex. Available from: http://www.flavex.com/naturextrakte/home/.
32. P. Corporation. Available from: http://www.phasex4scf.com/.
33. Medwest. Available from: http://www.med-west.com/index.html.
34. R.J. Clarke; and O.G. Vitzthum, *Coffee: recent developments*, ed. R.J. Clarke; and O.G. Vitzthum2001Great Britain: Blackwell Science.
35. D. Corchos. Available from: http://www.diam-corchos.com.
36. J.L. Kendall, D.A. Canelas, J.L. Young, and J.M. Desimone, *Polymerizations in Supercritical Carbon Dioxide.* Chemical Reviews, 1999, 99(2), 543.
37. A.I. Cooper, *Polymer synthesis and processing using supercritical carbon dioxide.* Journal of Materials Chemistry, 2000, 10(2), 207.
38. A. Salerno and P.A. Netti, *Introduction to biomedical foams.* Biomedical Foams for Tissue Engineering Applications, 2014, 3.
39. D.T.S. B.V.; Available from: http://www.dyecoo.com/.
40. M.J. Cocero, Á. Martín, F. Mattea, and S. Varona, *Encapsulation and co-precipitation processes with supercritical fluids: Fundamentals and applications.* The Journal of Supercritical Fluids, 2009, 47(3), 546.

41. U.B. Kompella and K. Koushik, *Preparation of drug delivery systems using supercritical fluid technology*. Critical Reviews in Therapeutic Drug Carrier Systems, 2001, 18(2), 173.
42. N. Murillo-Cremaes, A.M. López-Periago, J. Saurina, A. Roig, and C. Domingo, *Nanostructured silica-based drug delivery vehicles for hydrophobic and moisture sensitive drugs.* Journal of Supercritical Fluids, 2013, 73, 34.
43. N. Murillo-Cremaes, A.M. López-Periago, J. Saurina, A. Roig, and C. Domingo, *A clean and effective supercritical carbon dioxide method for the host-guest synthesis and encapsulation of photoactive molecules in nanoporous matrices.* Green Chemistry, 2010, 12(12), 2196.
44. P. Lopez-Aranguren, L.F. Vega, and C. Domingo, *A new method using compressed CO2 for the in situ functionalization of mesoporous silica with hyperbranched polymers.* Chemical Communications, 2013, 49(100), 11776.
45. P. López-Aranguren, J. Saurina, L.F. Vega, and C. Domingo, *Sorption of tryalkoxysilane in low-cost porous silicates using a supercritical CO2 method.* Microporous and Mesoporous Materials, 2012, 148(1), 15.
46. A.M. López-Periago, W. Sandoval, and C. Domingo, *Chemical modification of nanometric TiO2 particles by anchoring functional silane molecules in supercritical CO2.* Applied Surface Science, 2014, 296, 114.
47. N. Murillo-Cremaes, P. Subra-Paternault, J. Saurina, A. Roig, and C. Domingo, *Compressed antisolvent process for polymer coating of drug-loaded aerogel nanoparticles and study of the release behavior.* Colloid and Polymer Science, 2014.
48. Parker. Available from: http://www.parker.com.
49. Hip. Available from: http://www.highpressure.com/products/.
50. T.S. Tehnology. Available from: http://www.tst.tw/en/home.php.
51. Separex. Available from: http://www.separex.fr.
52. T. Process. Available from: http://www.tharprocess.com/index.html.
53. Swagelok. Available from: http://www.swagelok.com/.
54. C. Technologies. Available from: http://www.chematur.se/.
55. N. Prozesstechnologie. Available from: http://www.natex.at/index.html.
56. H. Kim, *An investigation of Corrosion Mechanisms of Constructional Alloys in Supercritical Watare Oxidation (SCWO) Systems.* , 2000, Massachusetts Institute of Technology.
57. A. Engineers. Available from: http://www.autoclaveengineers.com/.
58. L. Kumar, *Pressure vessel seal with self-energizing seal*, 1998, Google Patents.
59. A.E.-. Magnedrive. Available from: http://www.autoclaveengineers.com/products/magnetic_coupled_mixer/index.html?zoom_highlightsub=ly.
60. T. Isco. Available from: http://www.isco.com/.
61. Lewa. Available from: http://www.lewa.com/.

62. C. Vemavarapu, M.J. Mollan, M. Lodaya, and T.E. Needham, *Design and process aspects of laboratory scale SCF particle formation systems.* International Journal of Pharmaceutics, 2005, 292(1–2), 1.

CHAPTER III

FUNCTIONALIZATION OF POROUS SUBSTRATES USING SUPERCRITICAL CO_2

This chapter describes the synthesis procedures and the working conditions for the functionalization of porous silica with organic molecules using supercritical CO_2 as the reaction media. The functionalization step requires the knowledge of the best operating conditions f.i. pressure, temperature, reaction time or use of co-solvents, which are here discussed in detail. For the samples prepared results concerning the identification of the introduced species, the change in the textural properties and the thermal behavior of were analyzed here. For this reason, at the beginning of the chapter a short description of the solid state characterization tools applied is presented.

3.1 INTRODUCTION

The internal surface of micro and nanoporous substrates can be modified in terms of charge, functionality or even reactivity and stability by means of organic molecules. As described in chapter I, the modification of porous materials can be performed after their synthesis through post-synthethic methods. Among these methods, the silanization reaction is a common approach to graft organosilanes to the surface of porous silica. The silanization reaction using alkyl- and aminosilanes was performed here using a CO_2 solventless strategy. On one hand, hydrophobic molecules, such as octyltriethoxysilane, were used to modify the internal surface of the chosen substrates, with the objective of obtaining high capacity oil adsorbents. On the other hand, aminosilanes containing primary and secondary amino groups were grafted on porous substrates to obtain sorbents for CO_2 adsorption. The use of supercritical CO_2 as a solvent, requires to determine the solubility of the solutes involved in the reaction. Alkylsilanes exhibit high solubilities of *ca.* $2 \cdot 10^{-3}$ g L^{-1} in $scCO_2$ under low temperature and pressure conditions (45 ºC, 10 MPa). On the contrary, amino groups present in aminosilane molecules react with CO_2 forming carbamates, unsoluble salts in $scCO_2$. However, the carbamate formation is a reversible reaction that can be controlled through the operating conditions of pressure and temperature. In order to determine those conditions, the behavior of the aminosilane in $scCO_2$ was visually studied using the variable volume cell.

Porous sorbents for CO_2 adsorption purposes can also be prepared by introducing aminopolymer networks into the pores of the silica. In this thesis, porous silica was modified with a hyperbranched polyethyleneimine polymer through the in situ polymerization of ethyleneimine under compressed CO_2.

The knowledge of the surface characteristics of porous substrates is of great importance for an eventual improvement on their performance through the introduction of functionalities. Solid state characterization tools were applied to understand the physico-chemical properties of bare and functionalized substrates. Fourier transform infrared spectroscopy, thermogravimetric analysis and low temperature N_2 adsorption/desorption isotherms were used to determine the success of the functionalization, the interactions between the substrate and the organic molecules introduced and the textural properties of

the prepared materials. An special focus is given to identify the adaptation of hybrid structures for sorption processes.

From an experimental perspective, micro- and mesoporous structures are difficult to characterize being hard to understand the sorbent structure at a molecular level. Moreover, the underlying mechanism of the sorption process in highly complex organic functionalized materials is not yet fully understood. This incomplete understanding limits the possibilities of designing optimal adsorbents increasing the interest in performing complementary experimental-simulation studies. In this work, the adsorption of N_2 in organosilane-modified disordered mesoporous silica (silica gel 40), ordered mesoporous silica (MCM-41) and crystalline aluminosilicate (zeolite Y) is analyzed by a combination of experiments and simulations. The goal of the adsorption simulation study was twofold: first, to assess the ability of using grand canonical Monte Carlo to obtain quantitative predictions of the adsorption characteristics of gases on bare and organolsilane post functionalized products and, second, to provide new insights into the adsorption mechanism. The simulated results are discussed and compared with experimental data.

3.2 CHARACTERIZATION TOOLS

3.2.1 Confirming the presence of organic moieties: Fourier Transform Infrared Spectroscopy

To confirm the presence of the organic moieties in the treated materials, the Fourier transformed infrared (FTIR) spectra of the solid samples mixed with KBr were recorded on a Perkin-Elmer Spectrum in the range of *ca.* 500-4000 cm^{-1}. This technique was useful to determine the presence of organic moieties into the silica matrices, mainly through the characteristic peaks corresponding to the vibration of CH_3 and/or CH_2 groups in the range of 3000-2750 cm^{-1}.

3.2.2 Loading concentration and thermal stability: thermogravimetric and elemental analysis

Thermogravimetric analysis (TGA) allows the quantification of the weight loss occurring from a compound when increasing the temperature. In this thesis, thermogravimetric profiles of raw and modified substrates were recorded in a Q5000 IR TA Instruments in the temperature range of ambient to 800 ºC, applying a heating rate of 10 ºC min^{-1} and 25 mL min^{-1} of N_2 flow. Thermogravimetric analysis is a well established method to determine the organic content of organically modified porous silica [1-5]. Moreover, the obtained thermogravimetric profiles provided information about the decomposition patterns of the organic content introduced into the pore media. The representation of the first derivative of the weight loss curve indicates the inflection points where there is the greatest rate of change on the weight loss curve. The amount of silanol groups on the raw substrates was also estimated through this technique. In some selected samples, the organic content was determined by elemental analysis of C, N and H, performed in a Flash EA2000 Thermo Fisher Sci., in order to contrast data with thermogravimetric profile results.

The measurement of the weight loss occurring for the substrates modified with organosilanes allows the determination of the deposited silane (d_s), expressed as the amount of grafted molecules (g_s) per gram of dry matrix (g_m), $d_s = g_s\, g_m^{-1}$. The grafting density (ρ_{graft}) is expressed as the number of molecules (molec) per square nanometer of surface area referred to the raw substrate ($\rho_{grafting}$ = molec nm^{-2}). The molecular weight (M_w) calculations were performed independently for the trapped silanols, calculated as the hydrolyzed form of the alkoxysilane (f.i., for octyltriethoxysilane $Mw = C_8Si(OH)_3$) and for the grafted siloxane (only the organic chain, f.i., for octyltriethoxysilane $Mw = C_8$). The grafting density was calculated using Eq. 3.1:

$$\rho_{graft} = \frac{d_s \cdot 6 \cdot 10^{23}}{M_w \cdot S_a(raw)} \qquad \text{(Eq. 3.1)}$$

3.2.3 Determining the textural properties: N_2 adsorption isotherms

The low temperature adsorption of N_2 (-196 ºC) is a widely used technique for the characterization of porous materials [6]. In the recorded isotherms, the amount of adsorbed gas is represented versus the relative pressure, P/P_0, where P_0 represents the saturation pressure of the gas [7]. The application of adsorption models allows for the determination of the textural properties from the isotherms. Thus, the specific surface, the pore volume and the pore size distribution can be determined from them. The most widely used method applied on the determination of the specific surface area is the BET method, developed by Brunauer, Emmett and Teller [8, 9]. The expression of the BET model [9] includes the C value. The C parameter represents the surface adsorbate/adsorbent interaction energy, so it must have a positive value. Although rigorous interpretation of the C constant combined with its use for the determination of surface energies has fundamental limitations, this simplistic qualitative approach gives an idea of the hydrophobic character of the surface: the lower the C constant value, the lower the hydrophilicity. The BET equation can be plotted as a straight line where the linear relationship is maintained only in the range $0.05 < P/P_0 < 0.3$. The value of the slope is related to the surface area. The calculation of the specific surface area (S_a) through the BET method is based on the average area occupied by a N_2 molecule in a completed monolayer [10]. For N_2 at -196 ºC, the area is usually taken as 0.162 nm^2. The BET equation is applicable for surface area analysis of nonporous- and mesoporous materials, but in a strict sense, it is not applicable to microporous adsorbents. The high adsorption potentials that micropores exhibit make difficult to separate the processes of mono and multilayer adsorption from micropore filing. Micropore filling is usually completed at relative pressures below 0.1 and linear BET plots are found at even lower relative pressures. In this case, the obtained surface area value does not reflect the true internal surface area but should be considered as a kind of characteristic or equivalent BET area. For mesoporous materials with pores wider than 4 nm, pore filling occurs in the multilayer region of the sorption isotherms and usually no special difficulties arise in the application of the BET theory [11, 12]. The method of Barret, Joyner and Halenda (BJH) is the most applied one in the determination of the pore size distribution [13]. For BJH calculations, both the adsorption and desorption branch of the isotherm can be used. For microporous materials, the t-plot method, proposed by

Lippens and de Boer [14], is used for the determination of the micropore volume, surface area and the average pore size.

In this work, N_2 adsorption/desorption isotherms at -196 ºC of raw and modified substrates were performed on an ASAP 2000 Micromeritics instrument. Prior to the measurements, all samples were outgassed at 120 ºC under vacuum (0.26-0.53 Pa) for 24 h, with the exception of Zeolite Y that was degassed at 150 ºC for 48 h. The specific surface area (S_a) of the samples was determined by the BET method. Pore volume (V_p) and the mean pore diameter (D_p) were calculated using the BJH method from the adsorption branch of the isotherm. The micropore volume (V_{mp}) was estimated by the t-curve method.

3.2.4 Molecular simulations: structural models of the porous media

The gas adsorption behavior of pristine and organosilane modified porous silica was studied by molecular simulation. Prior to simulate the gas adsorption, the porous structure had to be modeled. The models for the surface-modified substrates were generated in two steps. First, the geometrical structure of the porous silica skeleton was generated together with the silanol groups. Second, silane chains were added considering two possible kinds of interactions with the substrate, physical (impregnation) and chemical (grafting).

3.2.4.1 Zeolite Y

The structures of crystalline solids, such as zeolites, are entirely known, and atomistic models are already available [15]. The faujasite structure was extracted from the zeolite database available in the Materials Studio software package [16]. A ratio Si/Al =1 was considered in the model, with no lattice defects and, thus, no silanol groups on the pores surface. Further details on the faujasite model can be found elsewhere [17]. The model of the zeolite Y structure is shown in Fig. 3.1a

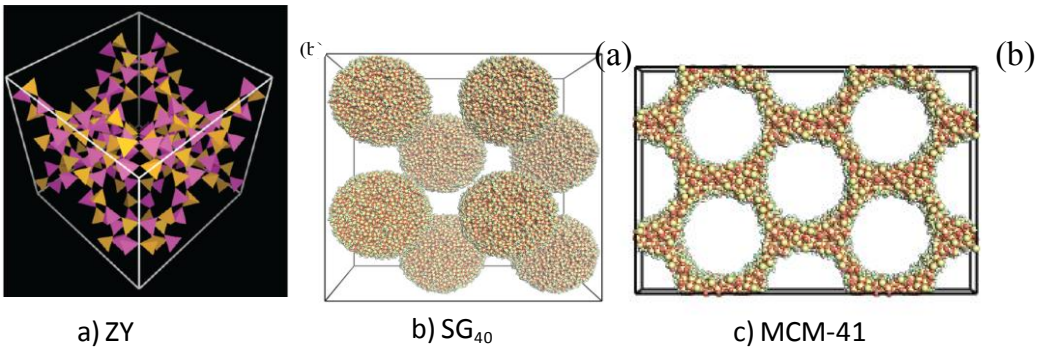

Figure 3.1 Models of the supports used for functionalization. Color key for SG40 and MCM-41: Si: yellow; bridging O: red; nonbridging O: green; H: white

3.2.4.2 Amorphous silica gel

For non-crystalline materials, such as silica gel, the link between the real and the model (simulated) material is merely statistical. Therefore, the first step to reproduce the functionalized silica gel surface was to build a realistic model to represent the pristine porous matrix. The method used in this work to generate the model of the amorphous silica gel is an atomistic procedure that follows the concepts of the experimental synthetic procedure [18-20]. Using the hard-sphere model, a cubic box with a preset void volume is filled with a chosen number of spheres and a predetermined surface area. The spheres are placed in the box at random positions until they fit in the simulation cell, being both the dimension of the simulation cell and the radius of the sphere found by iteration. Because of computational constrains, the specific model was constructed using only two interconnected spheres. Although this restriction may limit the validity of some quantitative aspects of the adsorption results, the model is suitable for the thoughtful analysis of obtained data, assessed by comparison with experimental observations.

The hard spheres in the box were subsequently replaced by a realistic model of pregenerated amorphous silica spheres. The primary silica nanospheres in the model were considered as constituted by nonporous vitreous silica; the initial amorphous silica blocks were taken from the Materials Studio structures database [16]. The primary silica spheres were built by carving out from the bulk vitreous silica model using a random central point

and the previously calculated radius. The surface of the silica spheres obtained in this manner is composed of oxygen atoms bonded to two silicon atoms and oxygen bonded to a single silicon atom. Single-bonded nonbridging oxygens were connected to hydrogen atoms and represent the hydroxyl silanol groups. The calculated silanol density in the model was 4.5 $OHnm^{-2}$. Figure 3.1b shows a snapshot of the generated silica structure. Information regarding the interaction parameters can be found in detailed elsewhere [17].

3.2.4.3 MCM-41

The MCM-41 model was generated following the work of Pellenq et al. [21] to build atomistic models of MCM-41. The method consists of carving out a hexagonal array of cylindrical pores (Fig. 3.1c) from a block of amorphous silica [22] obtained from the Materials Studio database [16]. The silica atoms outside the volume of the carved cylinder are kept, and all of the oxygen atoms bonded to these silica atoms are included in the silica model. These nonbridging oxygen atoms are connected to hydrogen atoms to form surface hydroxyl groups. The final structure generated by this procedure provides a sufficiently realistic model of amorphous silica, particularly of its surface. The full details of the generation of the model can be found elsewhere [17, 23].

3.2.5 Molecular weight determination of PEI polymer: Static Light Scattering and Maldi-ToF.

The experiments performed in this thesis include the polymerization of the ethyleneimine monomer under compressed CO_2, which leads to a hyperbranched polyethyleneimine polymer. The characterization of the polymer included its molecular weight determination. Two different techniques were applied: first, static light scattering (SLS) method was used to estimate the molecular weight of the synthesized polymer using a Nano Zetasizer equipped with a He/Ne 633 nm laser (Malvern Instruments). Four concentrations (0.25, 0.5, 0.75 and 1.00 g L^{-1}) of the polymer dissolved in deionized water were prepared. To determine the absolute molecular weight, a Debye plot was generated from the light scattering measurements performed for the solvent and polymer solutions. Second, an Applied Biosystems Voyager 6214 time-of-flight mass spectrometer equipped

with a matrix-assisted laser desorption/ionization source (MALDI-ToF) was also used to estimate the polymer molecular weight. Prior to measurements, the polymer sample was disolved in deionized water.

3.3 SUPERCRITICAL FUNCTIONALIZATION USING ORGANOSILANES

The silanization process using trifunctional silanes is described as an effective method to introduce organic groups into the surface of porous silica based materials (section 2.5.2). Silanization using supercritical CO_2 as a solvent medium is applied in this work to take advantage of the properties of SCFs (section 3.2). Previous works reported detailed studies of the bottom-up formation of hybrid materials by the self-assembly of trialkoxysilanes on the surface of nanoparticulate systems using $scCO_2$ as the solvent medium [24-26].

When the loading is carried out from a liquid solution the possibility of competition between solvent and solute molecules for the substrate adsorption sites often leads to the incorporation of both components into the internal surface of the porous system. The adsorptive behavior of $scCO_2$ in porous systems is fundamentally different from that of fluids at pressures and temperatures lower than the critical [27]. Adsorption at mesopores receives the name of capillary condensation and is not possible in supercritical fluids. Only microporous materials are slightly effective at adsorbing $scCO_2$, as physical adsorption is enhanced by the overlapping of the molecule-surface interaction potentials from opposite pore walls. Nevertheless, the micropore filling process is only accomplished in large quantities with vapors. Thus, competition between the solvent and the solute for the substrate adsorption sites is reduced in $scCO_2$ with respect to liquid solvents.

3.3.1Alkylsilanes

3.3.1.1 Functionalization procedure

The functionalization of porous silica using octyltriethoxysilane and octyldimethylmethoxysilane (Fig. 3.2a1,b1) was performed in the TharDesign reactor (Fig. 3.3a), which meets the requirement for the operating conditions applied (section 3.5).

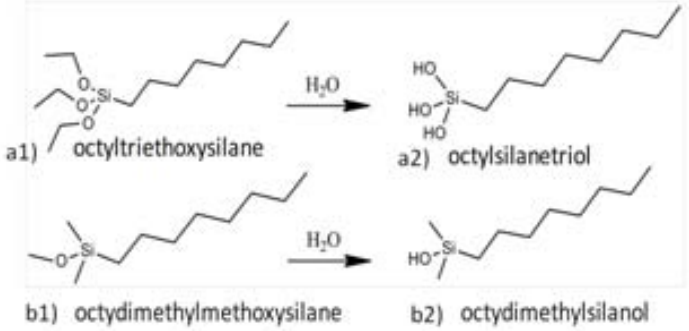

Figure 3 .2. Al kylsilanes used in this work: (a 1) octyltriethoxysilane and (b1) octyldimethylmethoxysilane with their respective hydrolized forms (a2, b2).

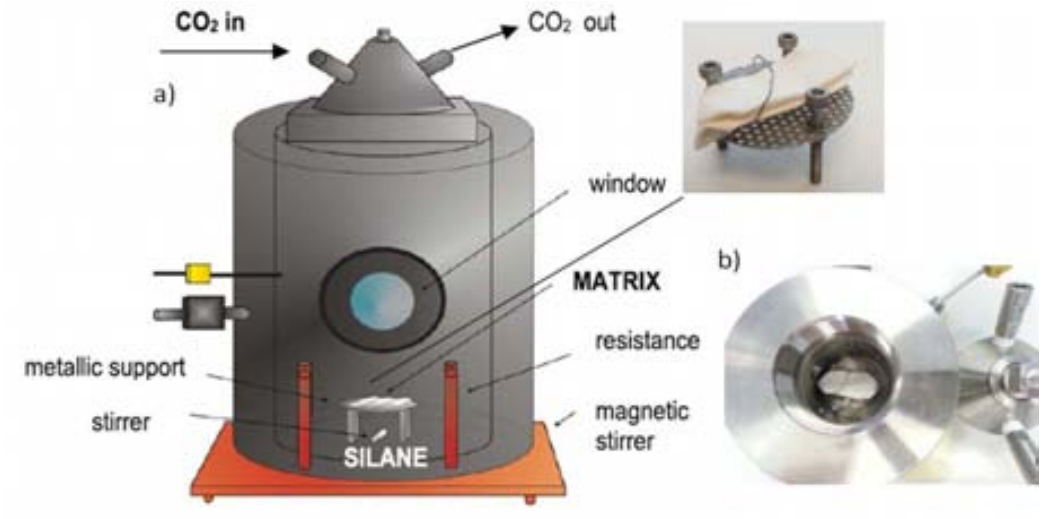

Figure 3.3 Representation of the set up used in the silanization process: (a) vessel charged with the silane at the bottom and the metallic support containing the matrices and (b) top view of the matrices placed in the metallic support.

The operating conditions were selected according to the solubility of the alkoxysilane used in $scCO_2$. García et al. evaluated the solubility behavior of octyltriethoxysilane in compressed CO_2 at 45 and 75 °C and pressures in the range of 8-18 MPa [28]. The

measured solubility data was correlated using the density-based equation proposed by Chrastil [29]. Table 3.1 shows the solubility values for octyltriethoxysilane at different conditions. Octyldimethylmethoxysilane exhibit less polarity than octyltriethoxysilane and therefore it is expected to have a higher solubility in $scCO_2$.

Table 3.1.Solubility values for octyltriethoxysilane obtained from experimental measurements from ref. [30].

Temperature [ºC]	Pressure [MPa]	Solubility [g L^{-1}]
45	10	$2 \cdot 10^{-3}$
	20	$18 \cdot 10^{-3}$
75	10	$0.2 \cdot 10^{-3}$
	20	$27 \cdot 10^{-3}$

A set of grafting experiments was performed at temperatures of 45 and 75 ºC and pressures of 10 and 20 MPa. Reaction times were varied from 90 to 420 min. For each experiment, the reactor was charged with *ca.* 0.5 g of the porous silica substrate enclosed in a cylindrical cartridge made of 0.45 µm pore filter paper, which was placed in the upper part of the autoclave in a metallic support (Fig. 3.3b). Liquid alkylsilane (*ca.* 0.5 mL) was added to the bottom of the reactor. Liquefied CO_2 was compressed with the aid of the syringe pump at the desired pressure (P). The autoclave was heated at the chosen temperature value (T). The system was stirred at 300 rpm with a magnetic stirrer during all the running time. At the end of each experiment, the reactor was depressurized and led to cool to room temperature. Recovered samples were washed with a continuous flow of $scCO_2$ at 10 MPa and 45 ºC during 30 min to remove the excess of deposited silane. For each substrate, a blank sample resulting from the supercritical treatment of the matrix in the absence of silane was also prepared under similar supercritical conditions of processing and washing [31]. Experimental conditions of each run are shown in Table 3.2, together with some products characteristics.

Table 3.2. Supercritical operating conditions and some obtained results: TGA estimated amount of deposited silane [ds] in the interval 150-600 ºC, expressed as grams of silane per grams of dry matrix [gs gm-1]; textural properties including the C value of the isotherm; silane grafting density (ρgrafting), expressed as the number of silane molecules per square nanometer [molec nm^{-2}].

Sample	T	P	t	d_s	S_a	V_p	D_p	V_{mp}	C	ρ_{graft}
	[ºC]	[MPa]	[min]	[$g_s\ g_m^{-1}$]	[m^2g^{-1}]	[m^3g^{-1}]	[nm]	[m^3g^{-1}]		[molec nm^{-2}]
b-CC	75	10.0	120	-	384	0.89	8.8	0.008	111	-
1-CC	75	10.0	90	0.065	350	0.71	8.5	-	42	0.85
2-CC	75	10.0	240	0.065	360	0.80	7.3	-	38	0.82
5-CC	75	10.0	420	0.095	300	0.67	7.4	-	33	1.02
3-CC	75	20.0	90	0.060	340	0.81	8.0	-	46	0.75
4-CC	45	20.0	120	0.056	340	0.79	7.4	-	54	0.7
b-SB	75	10.0	120	-	611	0.09	2.3	0.18	-	-
1-SB	75	10.0	90	0.146	500	0.07	2.0	0.17	-	1.02
2-SB	75	10.0	240	0.144	382	0.06	2.0	0.10	-	0.95
5-SB	75	10.0	420	0.163	52	0.02	1.9	0.01	-	1.16
3-SB	75	20.0	90	0.133	320	0.05	2.0	0.08	-	0.94
4-SB	45	20.0	120	0.132	464	0.07	2.0	0.13	-	0.94
b-SG_{40}	75	10.0	120	-	591	0.48	4.0	-	98	-
1-SG_{40}	75	10.0	90	0.055	460	0.41	4.0	-	48	0.43
2-SG_{40}	75	10.0	240	0.057	500	0.40	4.0	-	52	0.44
3-SG_{40}	75	20.0	90	0.078	410	0.38	4.2	-	49	0.57
4-SG_{40}	45	20.0	120	0.066	490	0.40	4.1	-	50	0.50
b-ZY	75	10.0	120	-	600	-	-	0.28	-	-
2-ZY	75	10.0	240	0.156	425	-	-	0.17	-	0.96
5-ZY	75	10.0	420	0.161	352	-	-	0.14	-	1.02
3-ZY	75	20.0	90	0.186	360	-	-	0.17	-	1.13
4-ZY	45	20.0	120	0.179	360	-	-	0.17	-	1.05

3.3.1.2 Infrared characterization

The FTIR spectra of the pristine matrices showed intense absorption bands in the 1000–1400 cm^{-1} region (Fig. 3.4a), which corresponded to the stretching vibrations of the O–Si–O bond in the SiO_4 tetrahedrons of the SiO_2 skeleton. The band at *ca.* 950 cm^{-1} was associated with vibrations of Si–OH bond. The two intense absorption bands present at 3400 and 1620 cm^{-1} were assigned, respectively, to the stretching and deformation vibrations of adsorbed water molecules. The presence of silane in the prepared samples was confirmed by FTIR (Fig. 3.4b) [32]. Characteristic bands corresponding to the organic part of the silane molecule were those appearing at *ca.* 2955 cm^{-1} (CH_3 symmetric stretching), 2928–2914 cm^{-1} (CH_2 antisymmetric stretching) and 2851 cm^{-1} (CH_2 symmetric stretching). The pattern of alkyl groups in the silane monolayer was assessed by means of the position of the CH_2 stretching bands [33].

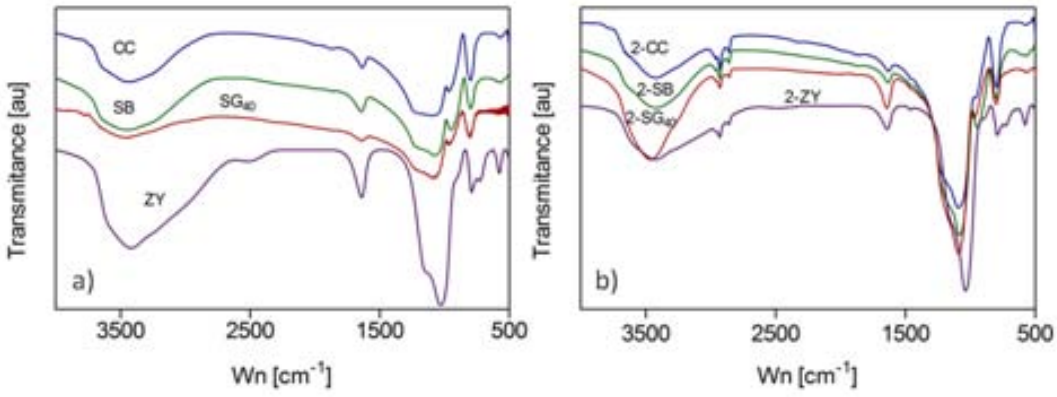

Figure 3.4 FTIR spectra of the different impregnated matrixes at 100 bar and 75 ºC: (a) 4000–500 cm^{-1} range, and (b) zoom of the 3000–2900 cm^{-1} range showing the position of the CH_2 stretching antisymmetric band. Vertical line is situated at 2926 cm^{-1}.

3.3.1.3 Thermal analysis and grafting density

Thermal behavior of silane treated samples as well as the amount of impregnated silane was studied by thermogravimetric analysis [34, 35]. For all alkylsilica samples prepared, the first significant weight loss occurred below *ca.* 150 ºC, and it was attributed to desorption of physically adsorbed water also present in the raw substrates. At temperatures

ranging from 150 to 600 ºC, the weight loss was attributed to evaporation and decomposition of the deposited organic moieties. For silica gel samples, some of the weight loss occurring within this temperature range was due to the removal of surface silanol by the formation of siloxane bonds with the concomitant loss of water [36]. For raw zeolite, the loss of water in this temperature interval was almost negligible. The chemistry of the reaction of trialkoxysilanes with hydrated surfaces is complex because several mechanisms can be involved simultaneously [37]. The silanization reaction is hydrolytically initiated, which leads to the formation of hydroxyl groups ($C_8Si(OH)_3$) that replace the alkoxide groups in the raw silane. In the supercritical anhydrous process, the water needed to start the hydrolysis comes from moisture adsorbed on the substrate pores and no additional water was added to the system. The formed silanols, first hydrogen bonded (Si–OH…HO–Si) and, then, condensed with other silanol groups or with the OH groups that are present on the surface of the pores forming in both cases siloxane (Si–O–Si) bonds. Hence, many different intermediates are possible and this was reflected in the recorded thermographs [38]. In general, it is described that the weight loss mainly occurs in two uneven stages, attributed to weakly and strongly bound alkyltriethoxysilanes. The first step takes place from *ca.* 150 to 375 ºC and corresponds to vaporization of physisorbed and hydrogen-bonded silanol molecules ($Mw_{(C8Si(OH)3)}$=192) (Fig. 3.5a). The decomposition of strongly bounded species (highly cross-linked and/or chemisorbed silanes) by cleavage of C–C and Si–C bonds occurs in a second step in the range of ca. 375–600 ºC ($Mw_{(C8)}$=113) (Fig. 3.5b) [35].

The influence of the operating conditions on product characteristics was first evaluated (Table 3.1). Working conditions, specifically 10 MPa and 75 ºC, corresponded to high solubility of silane in $scCO_2$ [30]. The reaction time is identified as a key parameter influencing the diffusion of the silane solution in the substrate pores. However, in the performed series of experiments, with reaction times ranging from 90 to 240 min, results indicated that the influence of the reaction time was quite limited after 90 min. This finding is related to the described enhanced diffusion of $scCO_2$ to the interior of the porous network compared to liquid solvents. Only for mesoporous samples the amount of deposited silane increased in experiments performed during 420 min, but in these cases the effect was most likely associated to multilayer formation. Large differences in regard of

deposited silane and resulting sample characteristics were observed as a function of the used substrate.

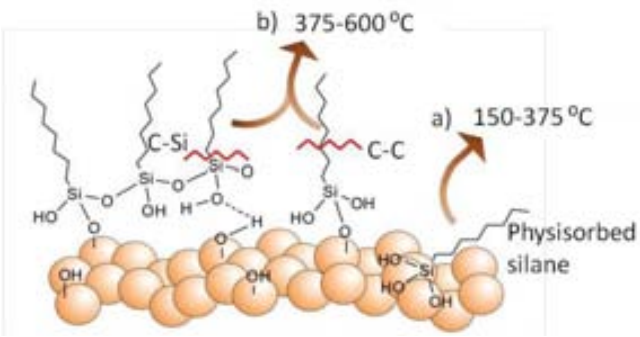

Figure 3.5 Schematic representation of the weight loss ranges on functionalized silica: weight loss of physisorbed silane (a) occurs at temperatures between 150 -375 °C whereas chemisorbed and (b) crosslinked silanes decompose at 375-600 °C.

Fig. 3.6 shows some examples of thermogravimetric and derivative curves for each type of silanized substrate. The importance of the weight loss produced in the two temperature intervals strongly depended on the substrate type. Polar mesoporous substrates have a highly reactive surface with a hydroxyl surface density of 4 –6 OH nm^{-2} [39]. In consequence, these compounds lost most of the deposited silane in the second temperature stage of the thermograph (375-600 °C): 90% for CC (Fig. 3.6a), 80% for SB (Fig. 3.6b) and SG_{40} (Fig. 3.6c). The maximum rate of thermal decomposition occurred at *ca.* 550 °C. The mesoporous space facilitated the siloxane self-condensation reaction between adjacent silanols and the high hydroxyl surface density assisted the chemisorption, thus, resulting in highly stable coatings. For running times between 90 and 240 min, total mass loss for these materials were 5–6 wt%, except for the SB matrix that presented values of deposited silane of *ca.* 14–16 wt%. This high impregnation percentage for the SB material indicated that adsorption also occurred in the micropore space. For experiments performed at 420 min, the amount of impregnated silane increased, although the extra-silane adsorbed was located in the area of weakly adsorbed silane, and could be due to multilayer formation (Fig. 3.6a and b for 5-CC and 5-SB samples, respectively). The estimated grafting densities were *ca.* 0.50 molec nm^{-2} for SG_{40}, 0.85 molec nm^{-2} for CC and 1.0 molec nm^{-2} for SB samples. The maximum bonding density attained for small-pore silica gel substrates

reported in the literature is 1.6 molec nm^{-2} when working at P > 50 MPa [40]. A continuous decay in the thermograph curve was observed for microporous zeolite samples in the range 200–600 ºC (Fig. 3.6d), with no inflexion point in the derivative curve. The surface density of silane deposited was 1.0–1.1 molec nm^{-2}. Most of the weight loss (*ca.* 75–80 wt%) occurred in the low temperature range (200-375 º C). For microporous samples, cross-linking is sterically hindered due to the lack of space, which resulted in a high number of low molecular weight species with low evaporation temperature. Moreover, silanol groups in zeolites were mostly present in the external surface as terminal groups, thus being difficult to attain chemisorption in the internal crystalline porous structure.

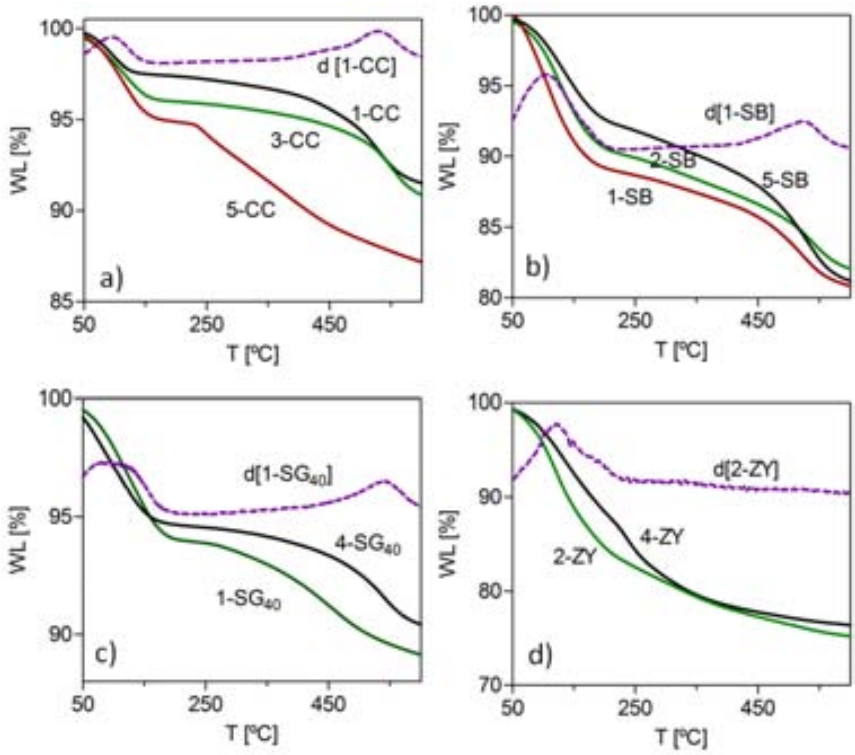

Figure 3.6 Selected TGA profiles of samples prepared using different conditions for: (a) CC, (b) SB, (c) SG40 and (d) ZY. d[sample] indicates the derivative curve of the corresponding sample.

3.3.1.4. Textural properties

Figure 3.7 shows the N_2 adsorption/desorption isotherms of the blank adsorbents (treated with pure scCO $_2$) compared to the respective silanized samples. For the mesoporous and microporous studied materials, the generated isotherms were distributed into the types I and IV. In all the cases, isotherms of raw ant treated matrices had a similar shape, but the silanized materials presented a lower volume of N_2 adsorbed. Raw and treated CC and SG_{40} samples displayed a type IV isotherm with an H2 hysteresis loop (Fig. 3.7a and c), corresponding to mesoporous systems with not well-defined distribution of pore size and shape. Both SB and ZY adsorbents had a predominant type I isotherm (Fig. 3.7b and d) indicative of microporosity.

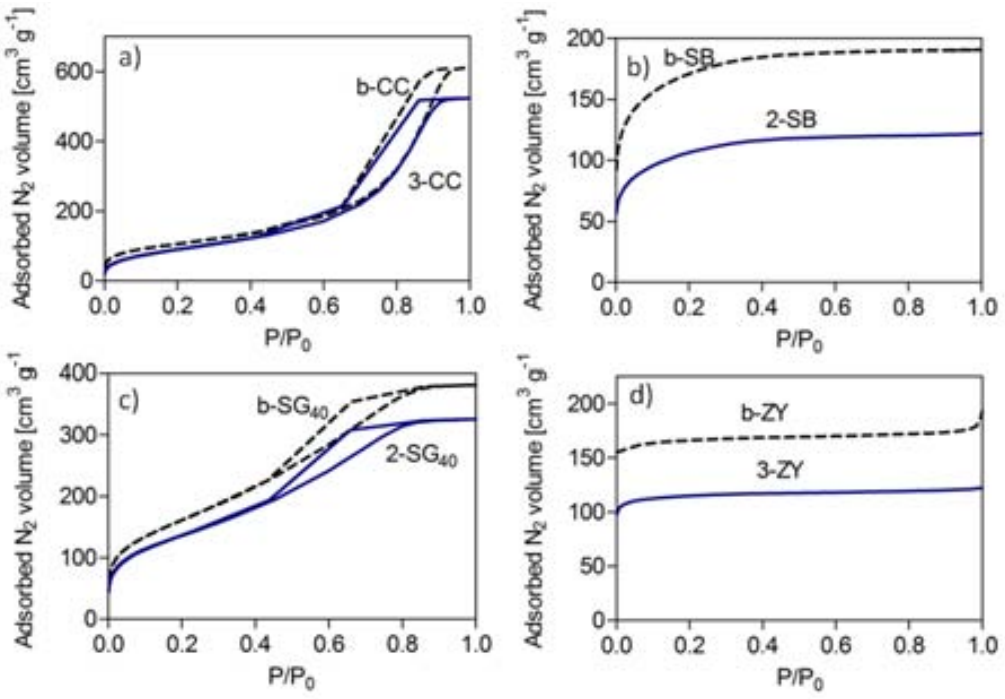

Figure 3.7 Recorded isotherms for blank and selected treated samples: (a) CC, (b), SB, (c) SG40 and (e) ZY.

The BET surface area and pore volume of the studied adsorbents are given in Table 3.2. Data of Table 3.2 shows that the surface area of treated mesoporous adsorbents (CC and

SG_{40}) underwent a slight decrease in comparison to bare matrices treated with pure $scCO_2$. On the contrary, the decrease in surface area was more noticeable for substrates with microporosity (SB and ZY). As a conclusion, the effect of silanization in the estimated values of surface area was found to be significant only for microporous materials. The thickness of the deposited C_8SiO- layer was estimated to be *ca.* 1.2 nm. As a consequence, silane deposition considerably modified the architecture of the cylinders with the smallest pore diameter, which had the highest contribution to the specific surface area. Similarly, the deposition of silane molecules on the internal surface of porous materials implied a decrease in pore volume, attributed to both decrease in mean pore diameter and potential pore blocking, more significant for materials with micropores (Table 3.2).The treatment of the silica materials with silane was expected to confer hydrophobicity to the samples. The hydrophobic character could be assessed from the intensity of the N_2 adsorption interactions with the substrate related with the values of the C constant in the BET equation (Table 3.2) [41]. Results indicated that bare materials had a relatively high value of the C constant (*ca.* 100), which was consistent with high-energy interactions between N_2 and the OH groups on the surface of a hydrated silica. The silanization process decreased the values of the C constant by a 2-fold factor, approximately. This is explained as a weakening of the N_2 interactions with the hydrophobic silanized surfaces.

3.3.1.5 Molecular simulation

The methodology commonly found in the literature for simulating functionalization of silica materials consists of using an algorithm to replace a number of surface silanol groups by organic moieties. A common procedure consists of adding to the surface only the organic group (R-) in the silane molecule and not the whole hydrolyzed compound (R-SiO) [42-44]. In that conventional approach, the additional silica group (−SiO) from the silane molecule is taken into account in the pure silica model as an extra SiO_2 layer. Consequently, this model gives better results for in situ modified materials than for the postsynthesis functionalized ones [42]. For this reason, the procedure of grafting the complete surface group (R-SiO) on the surface of the pure silica model material is taken in this work [17].

The driving force for functionalization with silanes was selected between impregnation of nonhydrolyzed species (Fig. 3.2a1,b1) and the surface reaction with hydrolyzed forms (Fig. 3.2a2,b2). The particular driving force selected for generating the models drastically depend on the concentration of surface silanols on the support.

Impregnation in microporous Zeolite Y

In a perfect zeolite crystal, the internal pore surface is electrically neutral, and no silanols would be present. Hence, silane addition in this substrate would be considered as an impregnation process and emulated by performing GCMC simulations of the adsorption and desorption of nonhydrolyzed species.

Grafting on mesoporous silica gel

Silica gel materials are characterized by having a large number of reactive silanol groups on the internal pore surface. Therefore, for these materials, it was assumed that silane functionalization was primarily driven by surface reaction. The silane chains are expected to react with the silanols tethering to the support instead of simply impregnating the surface. This hybrid material was modeled by introducing silane groups to the pregenerated model of silica gel and linking them to a certain number of silanols existing on the surface. For comparison with experimental results, the values of grafting density used to model the hybrid (0.4 and 0.6 mmol g^{-1} for 1-SG_{40_S} and 3-SG_{40_S} samples, respectively) were similar to those obtained experimentally under two different working conditions (Tables 3.2 and 3.3). Each silane chain was built on the silica surface segment by segment. The oxygen atom bonded to the silica gel surface was considered as the first atom or segment in the chain (covalent grafting) after eliminating the H accompanying the silanol group, whereas the second atom was the silicon bonded to the organic chain. The silica material can be modeled as a rigid structure, but the adsorbed alkylsilane molecules should have certain mobility in regard to the torsion and bending of the chains. The torsion and bending angles in the surface groups were handled using a coupled-decoupled configurational bias (CDCB) algorithm [45]. Additionally, a pregenerated Gaussian distribution for the probabilities of generating the bending and torsion angles for the

grafted molecules was used [46].The full details of the functionalization method can be found elsewhere [17].

Table 3.3 Textural properties and silane grafting density for the experimental and modeled samples.

Sample	Silane	S_a[m^2g^{-1}]	V_p [cm^3g^{-1}]	V_{mp} [cm^3g^{-1}]	D_p [nm]	ρ_{graft} [$mmolg^{-1}$]
SG_{40}	-	556	0.47	-	3.4	
1-SG_{40}	a2	460	0.41	-	3.6	0.41
3-SG_{40}	a2	410	0.38	-	3.7	0.58
5-SG_{40}	b2	424	0.35	-	3.3	0.59
SG_{40_S}	-	475	0.44	-	3.7	
1-SG_{40_S}	a2	490	0.37	-	3.0	0.4
3-SG_{40_S}	a2	532	0.33	-	2.2	0.6
6-$SG_{40\_S0.2}$	a2	540	0.29	-	2.0	0.4
7-$SG_{40\_S0.2}$	a2	536	0.26	-	1.9	0.6
ZY	-	750	-	0.28	-	-
4-ZY	a1	360	-	0.17	-	0.6
ZY_S	-	740	-	Na	-	-
4-ZY_S	a1	360	-	Na	-	0.59

N_2 adsorption simulations

N_2 adsorption was studied in the pregenerated model materials, both pristine and hybridized with surface groups. Simulations were carried out using the Monte Carlo method, equilibrating the adsorbent with a reservoir of N_2 and exchanging and moving molecules in the grand canonical ensemble (GCMC). The adsorption isotherms were calculated by simulating the average number of adsorbed N_2 molecules at different sets of bulk pressure. The soft-SAFT equation of state was used to relate the pressure of the bulk fluid to the chemical potential of the adsorbate [47, 48].

Once the equilibrium was reached, the amount of adsorbed molecules at this bulk pressure was averaged over a number of GCMC trials. For each value of pressure, 2.0×10^7 trials were used for equilibration and 1.4×10^7 steps for data collection. The adsorption

simulations took into account that in the simulation cell, periodic in three dimensions, the only rigid parts of the modeled hybrid material were the silica spheres. Conversely, the adsorbed surface chains had one end positionally fixed to the silica surface, but bending and torsion movements during the N_2 adsorption were allowed. The positions of the different atoms of the silane chain were recalculated during the adsorbate equilibration using the CDCB algorithm. Finally, the adsorbate molecules were allowed to displace to new positions as well as to enter and leave the cell; this was simulated by the insertion and deletion of fluid molecules. To avoid N_2 molecules being adsorbed inside the dense silica skeleton, the insertion and deletion of fluid molecules was restricted to the open pore space using a cavity bias [49]. In addition to the atomic and geometrical considerations for the adsorption model, the intermolecular interactions among adsorbate molecules, silane chains, and silica surface were input parameters in the simulation. Further information on the N_2 adsorption simulations can be found elsewhere [17]. Information about the porosity, the pore size distribution, the surface area, and the surface chemistry of pristine and silanized materials is obtained from the adsorption data of the GCMC simulations.

Zeolite Y.

Silanol groups in crystalline zeolite Y are mostly present in the external surface as terminal groups. Experimentally, some internal silanols have been noticed and are taken as an indication of lattice defects. However, all together, the amount of silanols in 1-ZY sample could be considered very small in comparison with amorphous SG_{40}.

The adsorptive impregnation of zeolite Y with octyltriethoxysilane was simulated by GCMC. The maximum calculated loading was 0.59 mmol g^{-1} (sample 4-ZY_S), which is a value equivalent to the one obtained experimentally (sample 4-ZY). The maximum impregnation value was limited by sterical constrains related to the length and shape of the silane molecule and the geometry of the pores and channels. The simulated and experimental N_2 adsorption isotherms for the pristine and impregnated zeolite samples (Figure 3.8a,b respectively) showed an excellent agreement. The main effect of silane functionalization was the reduction of the pore volume and thus the zeolite adsorption capacity.

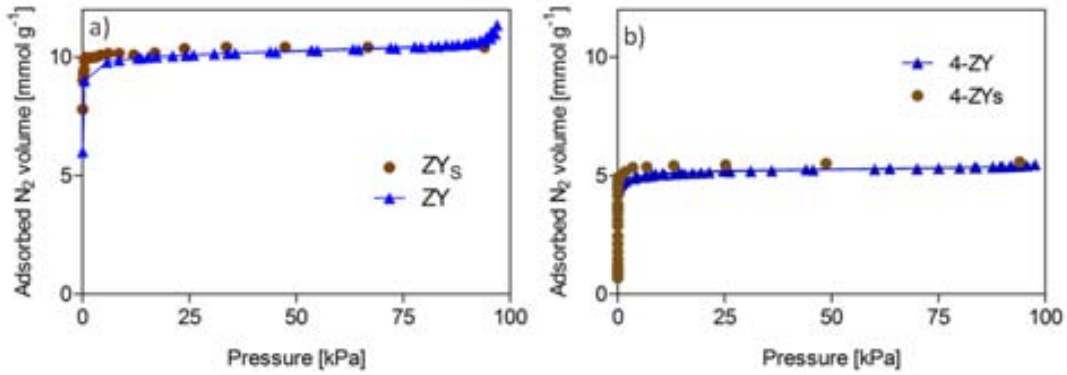

Figure 3.8 Results for zeolite Y: N2 adsorption isotherms for the (a) pristine and (b) impregnated samples for the experimental (blue) and simulated materials (brown).

Silica gel

i) Pristine silica gel

The model of the pristine silica gel was constructed with dimensions consistent with the structural properties of the mesoporous silica gel 40 (sample SG_{40} in Table 3.3). Owed to the broad range of parameters involved when modeling the pristine amorphous silica gel, it was necessary to impose restrictions on the solid phase by limiting the number of particles in the simulation cell to two. The low number of spheres used could affect the correct reproduction of the randomness of the void space in the silica gel. Nevertheless, this was required as a compromise between the CPU requirements for the simulation and a reliable estimation of the generated pore space in the unit cell. The capability of the method to accurately predict textural and adsorption properties was evaluated by comparing N_2 adsorption isotherms at -196 °C for pristine and impregnated materials obtained by either GCMC simulation or BET measurements. The validity of the silica gel model was first verified by comparing the silanol densities in the experimental and simulated materials. From the thermogravimetric measurement, a silanol density of 4.6 OH nm^{-2} was estimated for sample SG_{40}, which matches the calculated value in the model of 4.5 OHnm^{-2} for sample SG_T. Experimental and computed adsorption isotherms of the pristine material are

both of type IV (Figure 3.9a), exhibiting a well-pronounced stepwise character related to a two-stage mesoporous behavior [50-52].

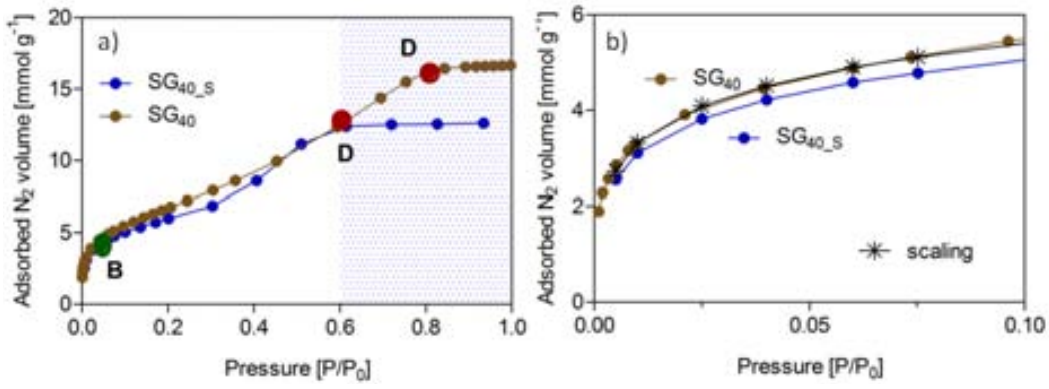

Figure 3.9 Experimental and simulated adsorption isotherms of N2 on pristine silica gel at -296 ºC for: (a) whole and (b) enlarged low pressure range.

In these systems, the convex part, representing the region from capillary condensation to pore filling (point D in Fig. 3.9a), is preceded by a concave wetting transition going from an empty state to intermediate conditions characterized by layer-by-layer growth on the pore walls. The simulation yielded the absolute adsorbed amount of N_2 straightforwardly correlated to the mesoporous volume inside of the cell because the model did not contemplate large mesopores or the macroporous interparticle volume. Hence, measured V_p values for the supercritically prepared samples were used for comparison with the model. The S_a (Table 3.3) of model materials was calculated from the simulated adsorption isotherm applying the BET equation. The point at which pore filling occurs is controlled by the accessible porosity, the pore geometry, the pore networking, and the tortuosity. In the studied systems, the total adsorbed amount at $P/P_0 = 1$ was higher for the synthesized material than for the simulated one (Fig. 3.9a). Moreover, the position of total pore filling (point D in Fig. 3.9a) occurred at lower pressure in the simulation (P/P_0 *ca.* 0.6) than in the experiment (P/P_0 *ca.* 0.8). Both facts indicate smaller pore size and total pore volume for the model (sample SG_{40_S}) with respect to the pristine material (sample SG_{40}), as reflected in the textural data (Table 3.3). This finding is on account of the practical limits of the simulation cell size, which did not allow the accurate replication of the complete pore size distribution (large pores). However, at $P/P_0 = 0.6$, similar adsorbed

amounts were found for the experimental and simulated isotherms. Therefore, to facilitate comparison, the adsorption at relative pressures higher than 0.6 will not be considered in further discussion, since the extra-adsorption at $P/P_0 > 0.6$ observed for the experimental material and related to that occurring in large mesopore and macropore voids could not be represented by the model material. The microscopic details of the silica should be reflected mostly in the low-pressure range ($P/P_0 < 0.1$) because adsorption in this region is determined by preferred adsorption sites. In mesoporous materials, the initial concave part of the adsorption isotherm is attributed to monolayer formation. Point B in Figure 3.9a is taken to indicate the stage at which monolayer coverage is completed and multilayer adsorption is about to begin. Figure 3.9b shows in more detail the low-pressure range of the isotherms. In this pressure region, the agreement between simulation and experimental data for adsorption on the pristine material was excellent. Still, the amount of adsorbed N_2 was slightly larger in the experimental sample than in the simulated one, which can be corrected by applying to the simulation isotherm a scaling factor (ϕ) [42, 53] based on the estimated porosity values for the experiment and the model (ϕ = 0.47/0.44 in Table 3.3). Thereafter, the validated model of simulated silica gel can be expanded to study functionalization by considering the grafting of the silane chains inside the material.

ii) Functionalized Silica Gel

The amount of octysilanetriol (Fig. 3.2a2) grafted on the surface of silica gel 40 following the supercritical procedure is shown in table 3.3. The calculated amounts of octyltrisilanol that reacted with the substrate at two different experimental pressures were 0.42 and 0.57 mmol g^{-1} for the samples 1-SG_{40} and 3-SG_{40}, respectively (Table 3.3 and 3.2 for experimental conditions). Experimental observations indicate that the highly reactive surface of amorphous silica gel might assist the formation of covalently bonded silanes, as surface reaction is the primary driving force for absorption versus impregnation. Moreover, the mesoporous space allows for the self-condensation reaction between adjacent silanols. Even though the steps of the experimental silanization process are well known, the complexity of the reaction makes it necessary to simplify the chemistry employed to model the functionalization. The most used generalization consists of not taking into account the formation of siloxane bridges between neighboring silane chains [42-44, 54]. This

assumption was also employed in this work. The hybrid simulated material was generated starting from the O atom covalently bonded to the silica surface, whereas the second atom was the Si bonded to the organic chain, which was added segment by segment. The molecules were always required to react in a monodentate covalent configuration with the surface and never with neighboring silane molecules. The designed algorithm is expected to allow analyzing and understanding simultaneously the surface of silica functionalized with both tri- and monoalkoxysilanes. Actually, monodentate bonding is the expected natural experimental behavior for trialkylmonoalkoxysilane molecules with a single hydrolyzable group (Figure 3.2b1). After hydrolysis, octyldimethylmethoxysilane generates the form b2, which reacts with the hydroxylated surface (#SiR_2−O− Si). For ease of comparison, a silanized 5-SG_{40} sample was prepared in the laboratory with a monoalkoxysilane, containing a grafting density of 0.59 estimated by TGA (Table 3.3). The adsorption isotherms of silica gel samples functionalized with silanes, measured for the synthesized products (a2 or b2) and calculated with GCMC for the simulated materials (a2), reflected many properties of the porous hybrid materials. The available space for N_2 adsorption, measured as the V_p, diminished with functionalization for all studied materials (Table 3.3). The reduction of mesopore volume was similar for the experimental (Fig. 3.10a) and model (Fig. 3.10b) materials.

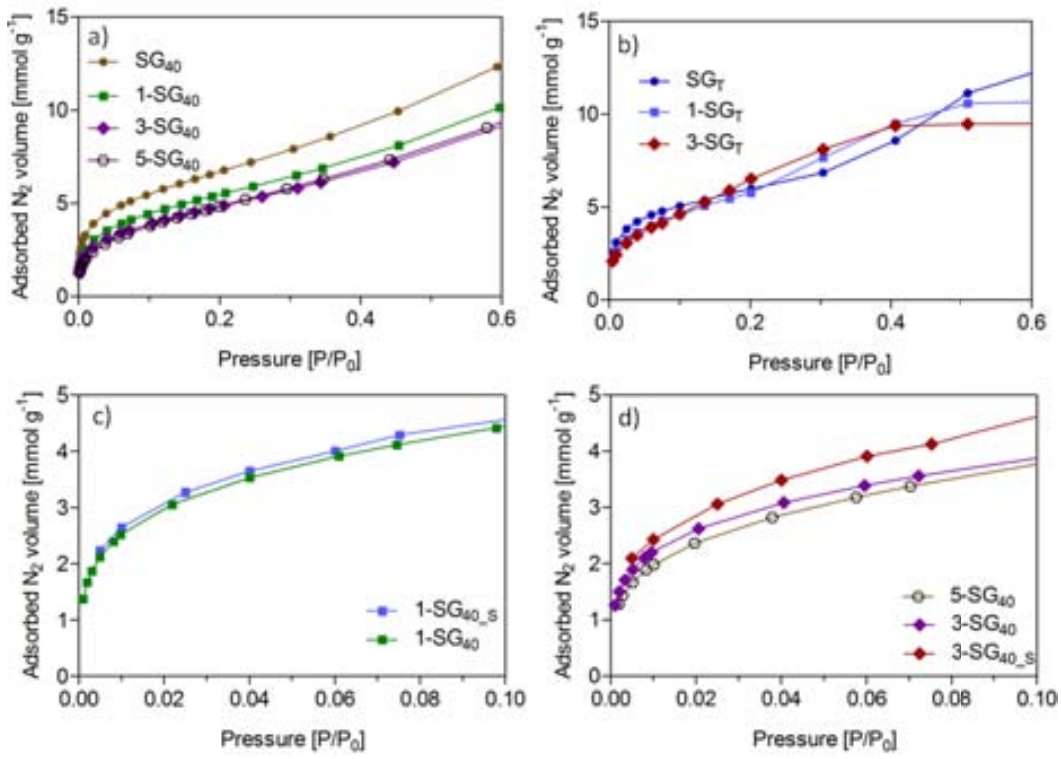

Figure 3.10 Experimental and simulated adsorption isotherms of N_2 on functionalized silica gel at -196 ºC for: (a) experimental materials, (b) modeled materials, and experimental and simulated materials loaded with (c) 0.4 mmol g−1 and (d) 0.6 mmol g−1 in the enlarged low-pressure range.

The V_p was reduced with respect to pristine silica gel in *ca.* 16% by functionalizing with ca. 0.4 mmol g^{-1} of silane, whereas a decrease of *ca.* 25% was estimated for deposited silane concentrations of ca. 0.6 mmol g^{-1}. Hence, the model was able to accurately simulate the reduction in the mesopores adsorption capacity due to the increasing void space occupied by hydrolyzed silane as the concentration increased. Conversely, the simulation slightly overpredicts the adsorption in the low-pressure region (Figure 3.10c,d for 0.4 and 0.6 mmol g^{-1} functionalization, respectively), which is the opposite behavior to that observed for the pristine materials (Figure 3.9b). For trialkoxysilanes, the overprediction likely reflects the absence of horizontal self-assembly in the simulated product, the importance of which increases with the functionalization degree. Whereas in the simulation the microvoids created among the randomly distributed chains can act as

strong adsorption sites (Figure 3.11a2), the chai ns in the ex perimental material ar e horizontally self-assembled, leading to a more compact packing (Figure 3.11a1).

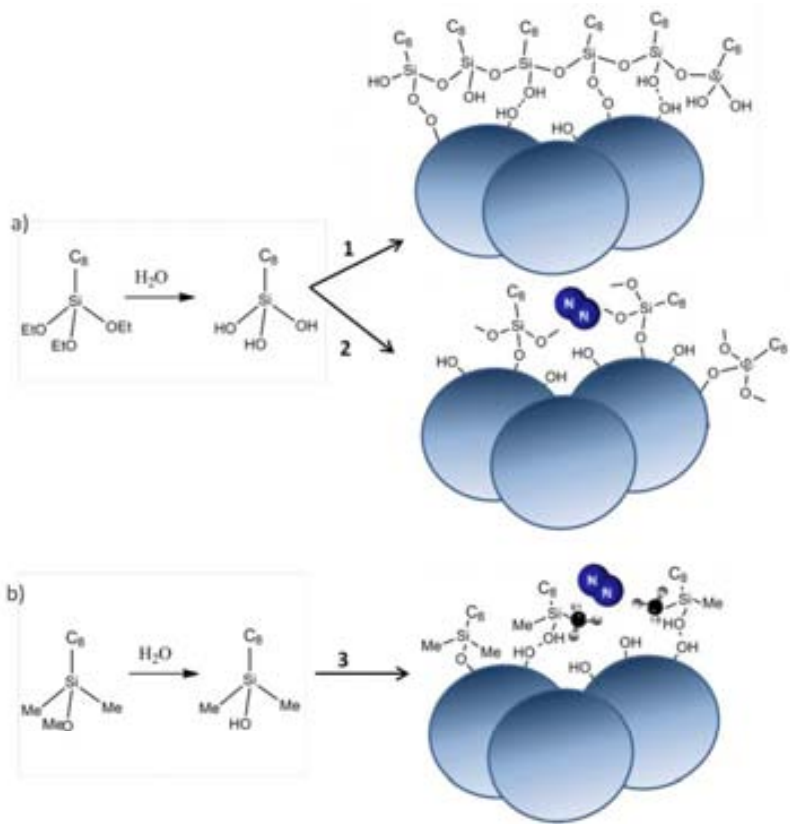

Figure 3.11. Schematic representation of the different functionalization possibilities for species: (a) a1 and (b) b1 from Fig.3.2.

Significant differences between the chemisorb ed monoalkoxyde and the m odel were also observed (Figure 3.10d). T he structu ral monodentate absorption of t he octyldmethylsilanol (Figure 3.2b2) could be considered to be similar to that adopted in the model (Fig ure 3.11b3 and a2, respectively). However, the oct yldimethylsilanol exposes lateral methyl gr oups (CH_3) am ong chains, which shield th e polar surface of the m etal oxide. Therefore, the methyl groups act as a structural barrier that prevents N_2 molecules interaction with the surface (Figure 3.11b3), resulting in low adsorption values in the low pressure rang e [34, 55]. The lateral silanol m oieties present in the model likely acted as

stronger adsorption sites than the CH_3 in the monoalkoxide. The macroscopic consequences found from this analysis were similar values of pore volume for both experimental and simulated materials but significant differences in the surface area (Table 3.3). The BET surface area decreased after silane adsorption for laboratory obtained samples and slightly increased for modeled compounds, indicating a large proportion of micropores in the simulated model. Geometrically the smallest pores have little contribution to the pore volume but a large contribution to the surface area. The extra micropores could be generated in the simulated material after functionalization of the mesopores. The reduction in the mean pore size was significant only for the simulated materials. In a different approach, and following the work of Schumacher et al. [42, 56] the order in the −Si−O-Si-O- horizontal polymerization observed experimentally for trialkoxysilanes was simulated by adding an extra layer of SiO_2 to the silica primary particles model, then building on the silica surface only the organic chain of the silane molecule. To compare both models, we calculated a new set of simulations, generating an additional amorphous silica gel model with the configuration of SG_{40_S} but with a radius 0.2 nm higher (the van der Waals radius of silicon and oxygen is 0.038 and 0.152 nm, respectively) than the original one. The alkyl chains were grafted in concentrations of either 0.4 or 0.6 mmol g^{-1} (samples 6-$SG_{40\_S0.2}$ and 7-$SG_{40\_S0.2}$, respectively) to the generated spheres of 3.7 nm radius. Schematic representations of the experimental and 0.2 nm model used are shown in Fig. 3.12a,b, respectively. For these samples, the reduction in adsorption capacity with respect to sample 1-SG_{40_S} was on the order of 33 and 38% for concentrations of silane chains of 0.4 and 0.6 mmol g^{-1}, respectively (Fig. 3.12c,d, respectively). These percentages are not comparable to the reductions observed in the experimental materials, which were on the order of 15 and 25% for samples 1-SG_{40} and 3-SG_{40}, respectively. Hence, the macroscopic adsorption behavior at different functionalization degrees was not accurately described by the silica gel model with a larger radius of the spheres. Using the approach of increasing the silica radius sphere in 0.2 nm, it was considered that the functionalized hybrid was constituted by a continuous film of −Si−O-Si-O- around all primary spheres (Figure 3.12b). Therefore, the accuracy of the results obtained using this approach would be higher for systems with high degrees of functionalization, that is, near a monolayer. Note that at grafting densities of 0.4 mmol g^{-1},

the dev iation between macroscopic adsorption values of th e experimental and th e simulated materia l was on the order of 55 % (co mpare samples 1-SG_{40} with 6-$SG_{40\_S0.2}$), whereas this value was reduced to 35 % by increasing the functionalization degree to 0.6 mmol g^{-1} (compare samples 3-SG_{40} with 7-$SG_{40\_S0.2}$). In contrast, the deviation was lower than 10 % for sa mples where eac h silane molecule was grafted entirely to the s ilane surface (compare samples 1-SG_{40} with 1-SG_{40_S} and 3-SG_{40} with 3-SG_{40_S}). The model with the larger spherical particle radiu s had less void volu me and a smaller pore diameter entering the region of micropore (D_p in Table 3.3).

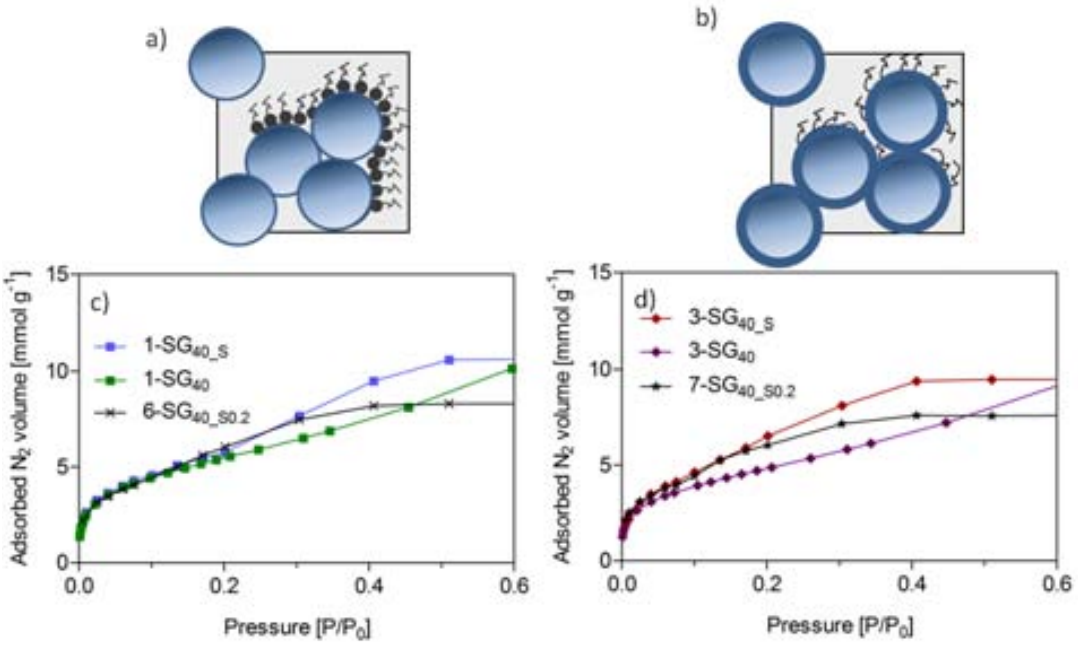

Figure 3.12 Schematic models used in samples: (a) 1-SGT and 3-SGT and (b) 6-$SG_{T0.2}$ and 6-$SG_{T0.2}$. Experimental and simulated adsorption isotherms of N_2 on silica gel at -196 ºC for samples functionalized with (c) 0.4 mmol g^{-1} and (d) 0.6 mmol g^{-1} of silane (species C in Figure 3.2).

3.3.2 Aminosilane

In a second approach an aminosilane containing a secundary amino group was used to functionalize the silica surface of the poro us substrates. 3-(Methylamino)propyltrimethoxysilane (MAP) (Fig. 3.13a), fro m Sigma–Aldrich, with a boiling po int of 106 º C, w as used as the grafting solu te. A si milar aminosilane,

aminopropylmethoxysilane (AP), with a primary amine was used for the simulations since more literature data is available for this system than for MAP. However, both compounds AP and MAP present almost an equivalent CO_2 adsorption capacity and efficiency, thus the results being comparable [57].

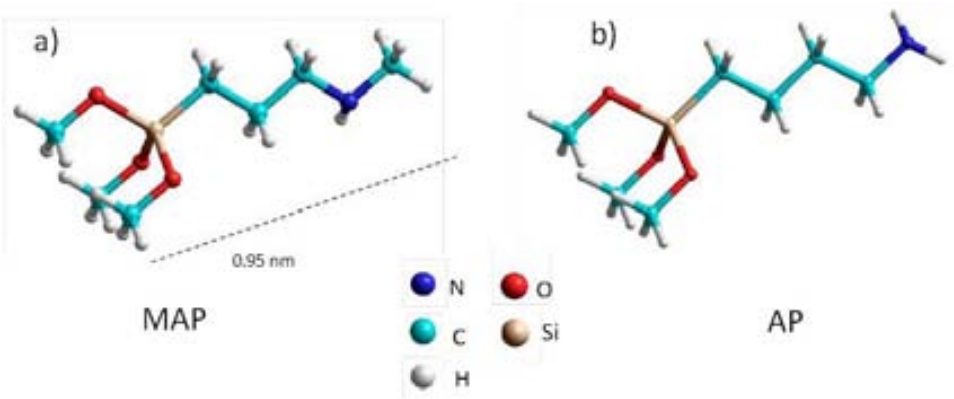

Figure 3.13. 3D conformation of aminosilanes MAP (a) and AP (b) used in this work obtained using HyperChem 8.03.

The use of the supercritical method for silanization requires an appreciable solubility of the solute molecules in $scCO_2$ to get them into the pores of the substrate. For alkylsilanes, the operating pressure and temperature determined the solute mole fraction in the fluid phase. Similar behavior is expected for the aminosilane, although for primary and secondary aminoalkylsilanes, an additional drawback is the formation of carbamate species with CO_2 giving place to an insoluble waxy solid. The reaction of CO_2 with primary and secondary amines is usually described by the zwitterion mechanism [58] (reaction 1a in Fig. 3.14). For the monoamine in an anhydrous environment, the zwitterion undergoes deprotonation by another amine molecule (reaction 1b), thereby resulting in carbamate formation. For the monoamine MAP, two amine molecules were thus needed to bind one molecule of CO_2. The carbamation is a reversible process for the studied amine and free aminosilane in solution can be obtained by selecting the appropriate conditions. In contrast to alkylsilanes, for this secondary alkylaminosilane, the solubility in $scCO_2$ cannot be

reported, since during the experimental determination it reacts with CO_2. Hence only the qualitative behavior of MAP with temperature and pressure in $scCO_2$ could be ascertained.

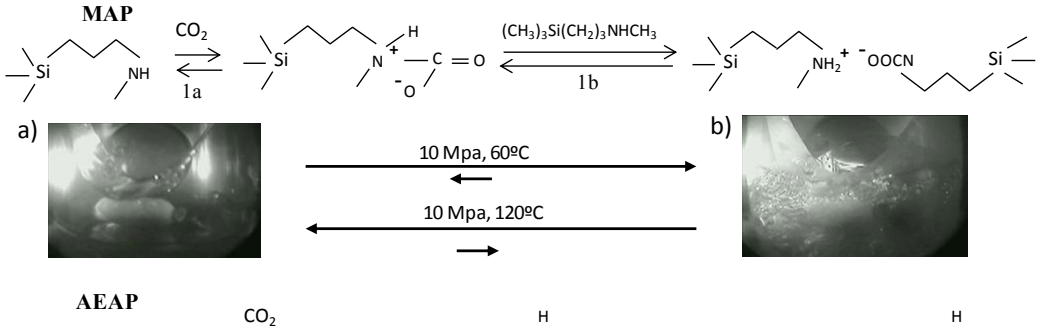

Figure 3.14 Reaction of the intermediate and the carbamate formation between the secondary alkylaminosilane MAP and CO_2. Images captured from the high pressure reactor window are shown as a function of temperature: (a) 120 ºC, and (b) 60 ºC . The observed interphase formed between the liquid MAP (a) or the waxy carbamate (b) and the $scCO_2$, since a large solute excess was added to the view cell to facilitate examen.

3.3.2.1 Behavior of the aminosilane in compressed CO_2

The behavior of MAP under $scCO_2$ was studied using the phase equilibrium analyzer (Thar Technologies Inc.). The procedure began by introducing compressed CO_2 (6 MPa) from the supply cylinder into the view cell previously heated at 45 ºC, which contained 1 mL of the aminosilane. The cell was then slowly heated to temperatures higher than 135 ºC. The pressure inside the solubility cell was kept constant in the range 7.5–9.0 MPa, either by pumping more CO_2 or by relaxing gas excess. Phase transitions occurring with temperature were visually determined in a video output by observing the phase conditions in the cell with stirring.

A white waxy solid was initially formed with the addition of pressurized CO_2 corresponding to carbamate formation (Fig. 3.14b at 60 ºC). Liquid amine was again visible when the temperature reached a value higher than 100 ºC (Fig. 3.14a, MAP at 120 ºC). Minimum working temperature was selected as 100 ºC. The release of CO_2 was hindered from MAP when the pressure of CO_2 was increased, since reactions 1a in Fig.3.14 were shifted to the right. Hence, experiments were mainly performed at relatively low pressures (7.5 and 9 MPa), close to the critical pressure of CO_2.

3.3.2.2 Functionalization procedure

For trifunctional aminosilanes ($NRSi(OR')_3$), compared to their monofunctional analogs ($NRSiR"_2OR'$), the possibility of bidentate covalent bonding and lateral condensation by crosslinking with vicinal silane molecules enhances the thermal stability of the grafted coatings. Hence, a trifunctional aminosilane was chosen in this work to synthesize the CO_2 adsorbents seeking relatively high temperature industrial applications. Trialkoxyaminosilanes are highly reactive and can polymerize in the bulk, being the extent of precursor oligomerization strongly affected by the presence of water. Therefore, solute and substrate were submitted to a drying treatment under vacuum previous to supercritical silanization.

The functionalization with MAP was performed on the 100 mL autoclave from Autoclave Engineers following a similar procedure to the one performed using alkylsilanes. Figure 3.15 illustrates the functionalization process. Prior to the addition of compressed CO_2 into the reactor, a moderate vacuum with the two stage oil rotatory vacuum pump (Edwards, E2M0.7, $3 \cdot 10^{-3}$ Mbar) was applied for 20 min to eliminate water from the system. In some of the experiments, a cosolvent chosen from methanol (Me), ethanol (Et) or diethyl ether (Eth) in a percentage of 2 - 5 v% of was added to the autoclave before CO_2 injection. 300 min was selected as the running time, keeping the stirring rate at 300 rpm. At the end of each experiment, the reactor was depressurized and led to cool to room temperature.

Figure 3.15. Schematic representation of the functionalization using aminosilane. The cartridge containing the porous matrix is placed in the upper part and liquid aminosilane is deposited at the bottom of the vessel.

Experimental conditions of each run are shown in Table 3.4, together with some products characteristics. Samples are labeled as x-MAP@substrate being x the sample number.

Table 3.4 Supercritical operating conditions and some obtained results: TGA estimated amount of deposited aminosilane, both total (ρ_{graft}) in the 100-600 ºC temperature interval and calculated at temperatures higher than 250 ºC ($\rho_{graft>250ºC}$), and aminosilane surface density ($\rho_{mgraft>250\ ºC}$), BET surface area (S_a) and BJH pore volume (P_v).

Sample	T [ºC]	P [MPa]	Cosolv [%v]	ρ_{graft} [mmol g^{-1}]	ρ_{graft} >250 ºC [mmol g^{-1}]	ρ_{mgraft} >250 ºC [molec nm^{-2}]	S_a [m^2 g^{-1}]	P_v [cm^3 g^{-1}]
1-MAP@CC	100	7.5	-	0.66	0.61	0.8	351	0.87
2-MAP@CC	100	9.0	-	0.83	0.79	1.1	342	0.86
3-MAP@CC	135	7.5	-	2.31	2.24	3.1	166	0.39
4-MAP@CC	135	9.0	-	2.37	2.30	3.2	142	0.37
5-MAP@CC	135	9.0	Mt2%	2.56	2.46	3.4	170	0.41
6-MAP@CC	135	9.0	Mt5%	3.24	3.14	4.3	117	0.26
1-MAP@SG_{40}	100	7.5	-	0.54	0.52	0.5	530	0.47
2-MAP@SG_{40}	100	9.0	-	0.53	0.51	0.5	555	0.48
3-MAP@SG_{40}	135	7.5	-	0.52	0.50	0.5	549	0.48
4-MAP@SG_{40}	135	9.0	-	0.53	0.51	0.5	532	0.47
1-MAP@MCM41	100	7.5	-	0.41	0.38	0.2	916	0.78
2-MAP@MCM41	100	9.0	-	0.48	0.43	0.2	902	0.77
3-MAP@MCM41	135	7.5	-	0.71	0.68	0.4	866	0.72
4-MAP@MCM41	135	9.0	-	0.88	0.82	0.4	858	0.74
5-MAP@MCM41	135	9.0	Mt2%	1.03	1.02	0.5	837	0.73
6-MAP@MCM41	135	9.0	Mt3%	4.17 4.14*	4.05	2.2	99	0.03
7-MAP@MCM41	135	9.0	Mt5%	4.29 3.80*	4.12	2.2	116	0.10
8-MAP@MCM41	135	9.0	Eth2%	1.56	1.51	0.8	457	0.40
9-MAP@MCM41	135	9.0	Eth3%	2.55	2.42	1.3	409	0.35
10-MAP@MCM41	135	9.0	Eth5%	5.59	5.39	2.9	10	0.01
11-MAP@MCM41	135	9.0	Et2%	2.08	2.02	1.1	681	0.57
12-MAP@MCM41	135	9.0	Et3%	2.94	2.83	1.5	554	0.47
13-MAP@MCM41	135	9.0	Et5%	4.53 4.50*	4.46	2.4	23	0.03
1-MAP@ZY	100	9.0	-	0.81	-	0.7	374	0.17
2-MAP@ZY	135	9.0	-	0.76	-	0.6	371	0.17

3.3.2.3 Infrared characterization

Fig. 3.16a shows the FTIR spectra of the studied MAP raw aminosilane and its respective carbamate c-MAP, obtained as a residue at the bottom of the reactor after the supercritical processing (9 MPa and 100 ºC). Relevant infrared bands were assigned following data compilation published by Bacsik et al. [59] on amine-modified silica contacted with CO_2. For the raw aminosilane (Fig. 3.16a), the bands corresponding to the CH_3 and/or CH_2 bending vibrations were detected in the range 3000–2750 cm^{-1}, and the characteristic peaks corresponding to –NH functional group at 1440 and 1458 cm^{-1}. For the precipitated carbamate, the band corresponding to N–C stretching was more visible than in the amine and appeared at 1540 cm^{-1} for the monoamine. Carbamate formation was evidenced by the turn up of the band corresponding to C=O stretching (hydrogen bonded) in the range 1700–1640 cm^{-1} (1645 and 1670 cm^{-1}) and the bands corresponding to COO^- symmetric stretching at 1433 and 1380 cm^{-1} (only band at 1384 cm^{-1} was visible in the recorded spectra). CO bands were difficult to determine in the c-MAP as only 0.5 CO_2 molecules can be attached to each monoamine. Fig. 3.16b shows some spectra of the as-recovered hybrid products, in which the development of the carbamate, as the main grafted specie, during system depressurization and cooling was expected. Ordered MCM-41 and disordered CC mesoporous silica are shown as examples. The two intense absorption bands at 3450 and 1640 cm−1 were assigned, respectively, to stretching and deformation vibrations of adsorbed water molecules. The presence of c-MAP in the prepared samples was confirmed by the occurrence of the three characteristic bands of the alkane part (CH_3, CH_2) of the aminosilane molecule, appearing in the interval 2955–2810 cm^{-1}. N–C and –NH bands appeared at 1550 and 1480 cm^{-1}, respectively. The band emerging in the range 1380–1390 cm^{-1} was assigned to COO^- symmetric vibration. Significant C=O stretching vibration band in C-MAP at ca. 1650 cm^{-1} could not be observed in the hybrid materials, since it was overlapped by the water band of the matrix.

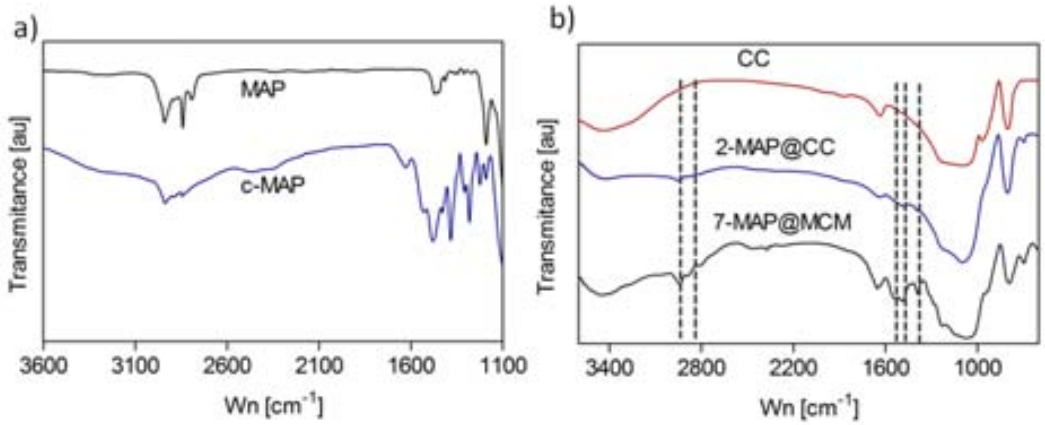

Figure 3.16. FTIR spectra of: (a) raw aminosilanes and precipitated carbamates, and (b) modified CC and MCM41 matrixes, where the vertical lines indicate CH3/CH2 groups in the 2955–2810 cm−1 range, COO− at 1385 cm−1, and N–C and –NH at 1550 and 1480 cm−1, respectively.

3.3.2.. Thermal analysis and grafting density

Raw MAP aminosilane and its correspondent carbamate,c-MAP, obtained as a residue at the bottom of the reactor, were studied by thermogravimetric analysis. Raw MAP evaporates or decomposes for the most part before 150 ºC (Fig. 3.17a). MAP and c-MAP, showed a similar TGA curves, indicating the low thermal stability of the carbamate. Under TGA experimental conditions, c-MAP lost the CO_2 at temperatures of 70-80 °C or even lower and acted then as MAP in the TGA profile. Representative thermogravimetric weight loss curves for the hybrid materials under study are shown in Fig. 3.17b. The different weight decay tendencies assigned from the TGA profiles of mesoporous amino loaded samples are shown in Table 3.4, together with the corresponding molecular weight. Samples 6, 7 and 13-MAP@MCM41 were also characterized regarding composition by elemental analysis (Table 3.4). The values of the total deposited amount (ρ_{graft}) obtained from elemental analysis (%wt of N) were consistent with the data estimated by TGA, indicating the validity of the selected intervals of temperature used to calculate the weight loss of the different species (100, 250 and 650 ºC for sorbed water/CO_2 and impregnated and grafted aminosilane, respectively). The high hydroxyl surface density of the studied mesoporous substrates promotes the chemisorption of aminosilane species as occurring with alkylsilanes. These compounds lost most of the deposited aminosilane at temperatures higher than 300-350 °C (Fig. 3.17b) indicating the high thermal stability of the prepared

hybrid sorbents. The stable grafted amine was considered, similar to the case of alkysilanes, as the amount resulting by estimating the amine density at temperatures higher than 250 °C (Table 3.4, ρ_{graft}> 250 °C), corresponded to the majority (>90 wt%) of the deposited silane.

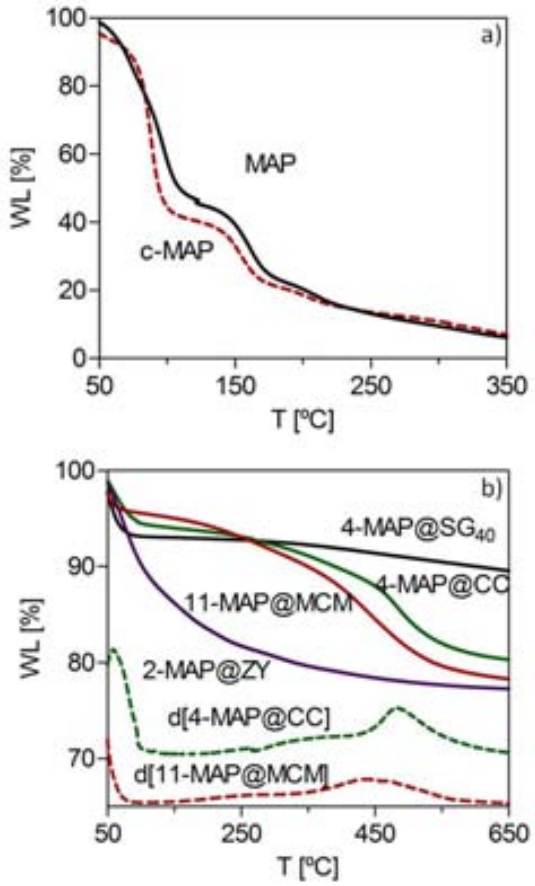

Figure 3.17 Recorded thermogravimetric profiles for: (a) raw MAP and its carbamate c-MAP, (b) selected treated samples with MAP and derivative curves d[sample].

Comparing samples 4-MAP@CC and 11-MAP@MCM41 (Table 3.4) with a similar grafting density (*ca.* 2 mmol g^{-1}), the derivatives of the weight loss curves (Fig. 3.17b) indicated a higher thermal stability for the aminosilane molecules grafted on CC than on MCM-41. As loadings are similar, the reason for this difference has been primarily related to the high grafting density per unit of surface area obtained for 4-MAP@CC sample (*ca.* 3

molec n m^{-2}) with respect to 11 -MAP@MCM41 sample (*ca.* 1 m olec nm^{-2}). For bo th studied mesoporous substrates, it is expected that the principal reaction occurs between the surface silanols on the silica and the alkoxy portion of the aminosilane molecule (not the amine). For the low surface grafting density estimated in the MCM-41 substrate, a high proportion of isolated grafted amines and surface silanol complexed amines are expected to take pl ace (Fig . 3.18a). Increasing t he surface grafting density, as occurs in th e CC substrate, the pendant amines cou ld grou p together close eno ugh to interact with th eir nearest neighbor by cross-linking through both side-silanols and side-amine functionalities (Fig. 3.18b). Additionally, the larger mesoporous space in CC compared to the narrower pore structure of MCM-41 could facilitate the siloxane self-condensation reaction between adjacent silanols, and th e highly hydroxy lated surface as sisted the chemisorption, thus resulting in highly stable and dense self-assembled monolayers.

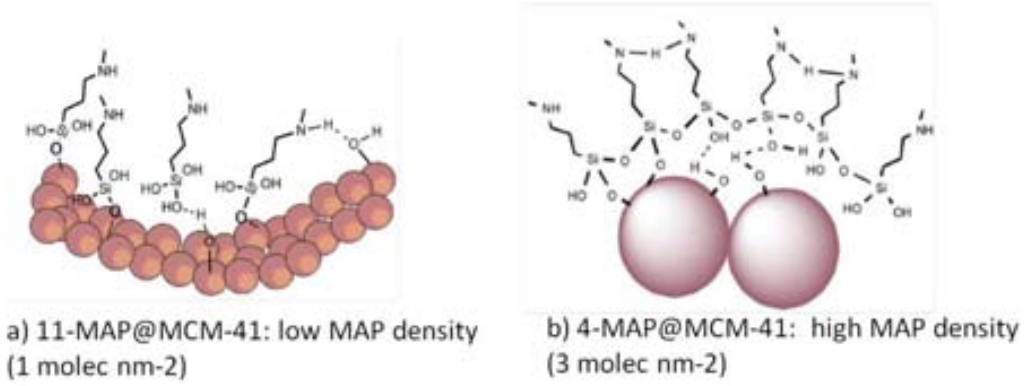

Figure 3.18. Schematic representation o f pote ntial aminosilane conf igurations grafted on amorphous silica surfaces: (a) one-dimensional channels in MCM-41, and (b) primary silica particles in disordered mesoporous silica gel CC.

The a minosilica samples prepared in th is work using the S CF technology have increased th ermal stability co mpared to results obtained by other auth ors us ing similar trialkoxyaminosilane molecules and mostly the sorbent MCM-41 [2], and the two weight drops corresponding to physi- and chemisorbed aminosilane were almost not observed in the TGA profiles (Fig. 3.17b), bein g practically all a minosilane stron gly bond ed to the surface. Conversely, it has been stated that deposition from toluene solutions often leads to the formation of lo w-quality film s because of th e difficulty i n controlling the amount of

water in the solvent mixture [38]. An overabundance of water produces an uncontrolled polymerization in the solvent phase and the deposition of condensed polysiloxanes, resulting in materials with high loading, but with an irreproducible configuration of amines. Contrarily, in a system with water deficiency, condensation with substrate hydroxyls has to be self-catalyzed by the amino moieties resulting in low loading and disordered assemblies. In the anhydrous supercritical method used in this work, only water physically adsorbed on the support pore walls was added to the system. However, the used silica supports adsorbed a considerable amount of water in the order of 4–8 %wt. Hence, previous to silanization, substrates were partially dehydrated at 100 ºC under vacuum with the purpose of reducing the amount of physisorbed water and the risk of amine solution polymerization. Because the solubility of water in $scCO_2$ is low, during the silanization reaction, a reasonable number of water molecules were expected to remain associated with the substrate surface rather than free in the bulk of the solution. Hence, the hydrolysis reaction, in which water reacts with the alkoxysilane ($NRSi(OR')_3$) to form the alkoxysilanol ($NRSi(OH)_3$), was expected to predominate near the substrate surface and not in the solution bulk, which limited the aminosilane molecules to primarily react at the substrate surface allowing for an homogeneous surface coverage. As the temperature was increased to 100-135 ºC, some water molecules were likely able to desorb and to enter the solvent phase leading to alkoxyaminosilane hydrolysis and condensation in the bulk. However, the solubility of aminosiloxane dimmers and oligomers in CO_2 was expected to be much lower as compared to that of single precursor molecules of aminosilane and would not participate in the silanization reaction. For the microporous substrate ZY, a continuous decay in the range 100-450 ºC was observed in the thermograph curve (Fig. 3.17b). For the zeolite Y chemisorption was not feasible due to the lack of a significant amount of internal hydroxyl groups. Moreover, for the narrow micropores cross-linking was sterically hindered due to the lack of space, which resulted in the fact that most of the weight loss (*ca.* 70 w%) occurred in the low temperature range (< 250 ºC). Hence, all deposited amount was considered as physisorbed and the loading was estimated from the weight loss in the interval 150-500 ºC.

3.3.2.5 Influence of processing parameters on the aminosilane uptake

In Fig. 3.19a, the obtained loading values are represented, expressed as mmol of N grafted per unit weight of dry support (T > 250 ºC, Table 3.4). For SG_{40}, the loaded amounts of MAP were similar to those previously obtained with alkylsilanes (*ca.* 0.5 mmol g^{-1} corresponding to a surface grafting density of ca. 0.5 molec nm^{-2}) and, under working conditions, independent of the experimental pressure or temperature. The MAP loaded amount for crystalline ZY substrate was in the order of 0.8 mmol g^{-1}, and again similar to that obtained using alkylsilanes as a solute (table 3.4) [60]. In absence of a cosolvent, MAP@MCM41 samples had grafting densities in the order of 0.4–0.8 mmol g^{-1}, which are values substantially lower than the ones presented by other authors using the liquid toluene processing method (1.5–2 mmol g^{-1}) [2, 61, 62]. Under working conditions, the low grafting density attained for MCM-41 samples was related to diffusion limitations. On one side, this mesoporous material does not possess interconnected channels, but has a hexagonal array of 4 nm pores arranged as one-dimensional parallel channels (Fig. 3.1). On the other side, it should be considered that primary and secondary amines are rather polar and pure $scCO_2$ is not sufficiently strong as a solvent in this case. Hence, at the low driving force for diffusion provided by the low concentration of solute in the CO_2 phase, it was concluded that modification of this substrate *via* 300 min of supercritical silanization was limited by intraparticle diffusion of the aminosilane. Certainly, under similar experimental conditions, the silica gel CC substrate with an interconnected network of large mesopores (9 nm) showed the highest loading values (2.3 mmol g^{-1}), indicating lower diffusion restrictions than in MCM-41.

For all the MAP@substrate studied samples, the loading was not affected by the pressure when increased from 7.5 to 9 MPa (Fig. 3.19a). An increase of the CO_2 pressure favored the acid-base reaction between the amine and CO_2 (reaction 1a sifted to the right in Fig. 3.14), and, consequently, the availability of the reactant amine in solutions was reduced. In contrast, by increasing the pressure at constant temperature, the CO_2 density increased together with the solubility of the free amine in $scCO_2$. These two opposite effects generated by the increase of pressure led to not significant consequences in the estimated grafting density values. A priori, the carbamate/amine ratio is expected to be

mainly dependent on temperature [63], since the formation of carbamate is reversible by heating. In the same way, the temperature was the main parameter affecting the loading values (Fig. 3.19a). This effect could be clearly noticed in MAP@CC samples, in which by rising the temperature from 100 to 135 ºC the loading was increased by a factor of *ca.* 3.5. Although less important, the influence of temperature was also appreciable in MAP@MCM41 samples. The addition of a small amount of a cosolvent to $scCO_2$ improves the solubility of polar species in the supercritical fluid. Therefore, 2–5 %v of protic cosolvents, Et and Me, and the non-protic Eth were utilized in an attempt of increasing the solubility of the aminosilane MAP in the supercritical solvent, and, thus, the impregnation efficiency of mesoporous MCM-41 and CC substrates. The use of a cosolvent significantly increased aminosilane loading with respect to the values obtained in pure CO_2 (Fig. 3.19b). In this case, the strongest cosolvent effect was noticed for the MAP@MCM41 samples, where loadings as high as 3.5 mmol g^{-1} were reached (Table 3.4). Similar effects were obtained with the three studied cosolvents.

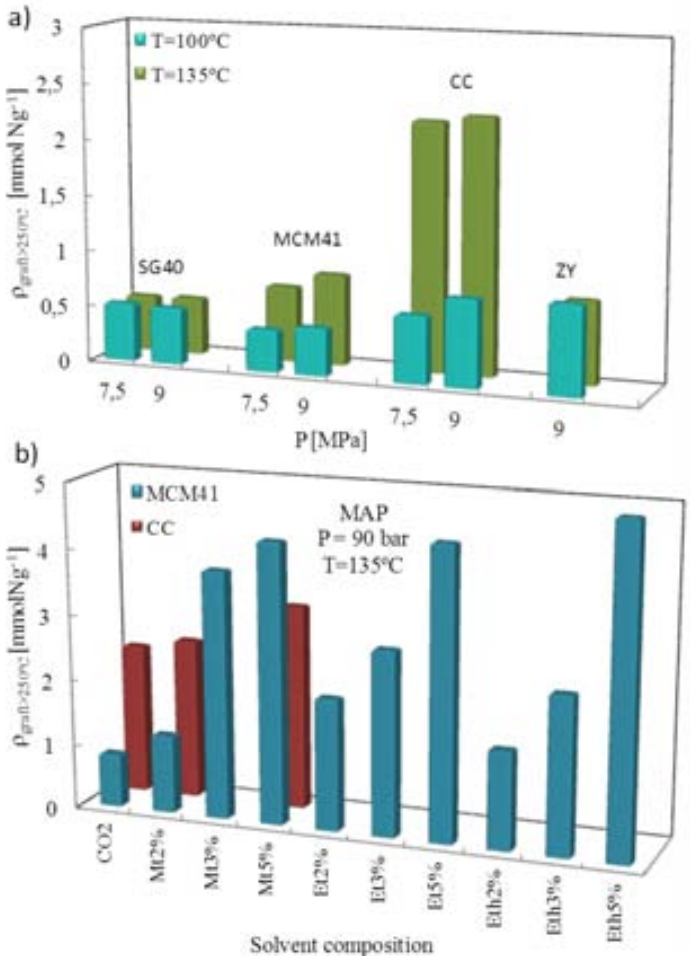

Figure 3.19 Loading, expr essed as mmol of incorporated nitrogen per unit weight of substrate, as a function of exp erimental conditions: (a) pre ssure and temperature, and (b) solvent composition.

3.3.2.6 Textural properties

Figure 3 .20 shows th e N_2 adsorption/desorption isotherms of the raw mesoporous adsorbents compared to the respective aminosilanized samples. For the mesoporous SG_{40}, CC and MCM-41 (Fig. 3.20a,b,c) bare ma terials, the gen erated isotherms were distributed into the type IV. CC and SG_{40} matrices displayed a H2 hysteresis loop, corresponding to mesoporous sy stems with not well-defined distribution of pore size and s hape. Th e

unmodified MCM -41 exh ibited a sharp step of capillary con densation in pr imary mesopores at the relative pressure of *ca.* 0.5, indicating a narrow pore size distribution of the material.

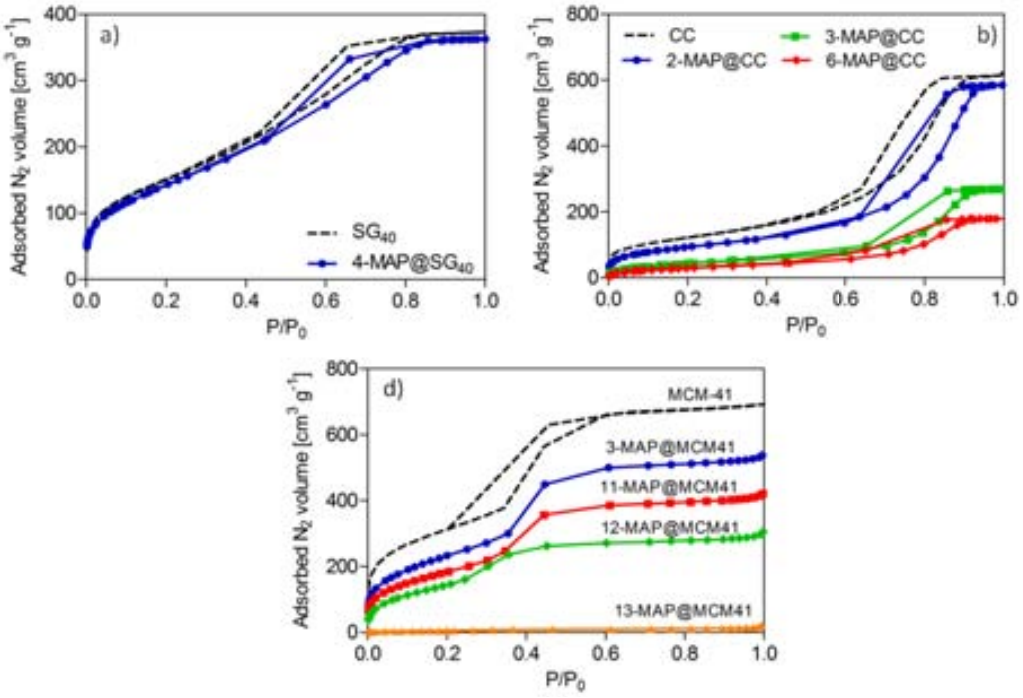

Figure 3.20 Recorded isotherms for pristine and treated mesoporous samples: (a) SG40, (b) CC and (c) MCM-41.

ZY adsorbent (Fig. 3.21) had a type I isotherm, indicative of microporosity. The BET surface area and pore volume of the raw and modified substrates are given in Table 3.4.

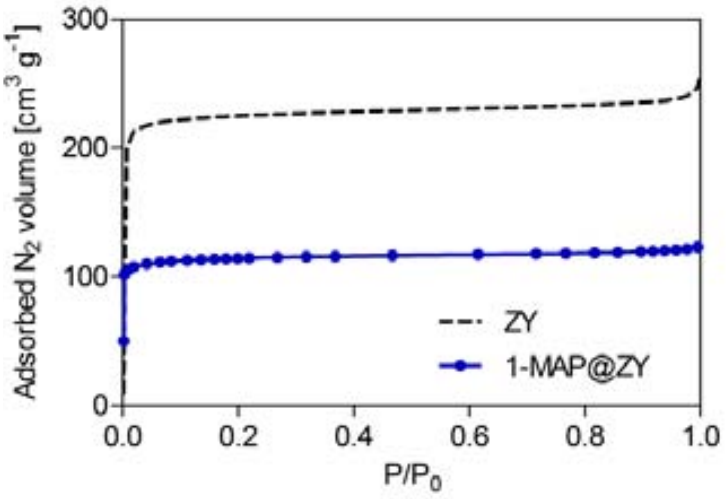

Figure 3.21 Isotherms for pristine and modified ZY.

For the studied supports, the surface area and pore volume decreased after modification [62] as a function of the grafting density, as it is represented in Fig. 3.22 for the P_v.

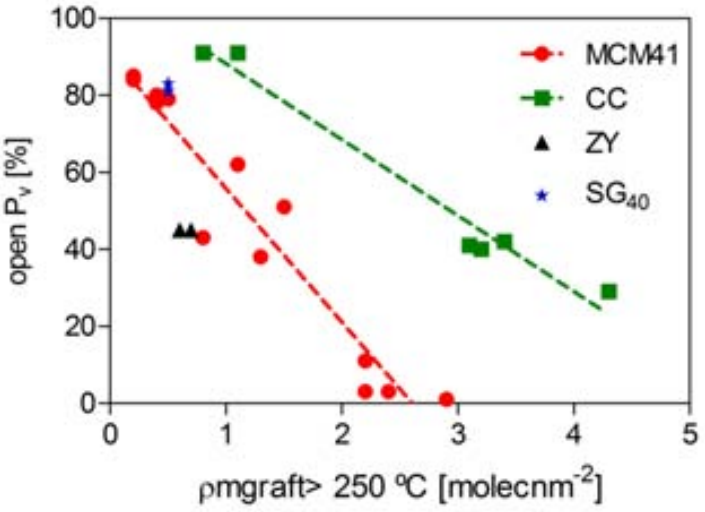

Figure 3.22 Influence of the grafting density in the percentage of available open pore volume for the four different studied substrates. Lines in CC and MCM-41 are tendency lines.

The microporous zeolite, with loadings in the order of 0.6–0.7 molec nm^{-2}, lost *ca.* 50 % of the micropore volume after silanization. For SG_{40}, the grafting density was relatively low, in the order of 0.5 molec nm^{-2} and, consequently, the pore volume only diminished in a 15% with respect to bare SG_{40}. A similar decrease in P_v was observed for CC samples loaded up to *ca.* 1 molec nm^2. Loadings of 3–4 molec nm^{-2} led to a decrease in the void space of CC samples of 60–70%, but the overall shape of the adsorption isotherms remained unchanged, indicating capillary condensation in mesopores (Fig. 3.20b). For MCM-41 matrixes, grafting densities in the order of 1–1.5 molec nm^{-2} decreased the available pore volume in ca. 50% while the hysteresis disappeared from the isotherm (Fig. 3.20c). Increasing the loading to 2–3 molec nm^{-2} implied a total drop off in sample pore volume, attributed to pore blocking at least for N_2 adsorption. Comparing mesoporous MCM-41 (4 nm pore diameter) and CC (9 nm pore diameter) samples at a similar loading (*ca.* 3 molec nm^{-2}, samples 3-MAP@CC and 10-MAP@MCM41), accessible pore volume was only noticed for the 3-MAP@CC sample. For mesoporous materials, surface densities of 3 molec nm^{-2} corresponded to values close to monolayer surface coverage. It was reasoned that mesoporous materials with large pore opening are more adequate to accommodate a monolayer of packed monoamine on the intrachannel surface, even if they have less total surface area for grafting. For the 4 nm pore diameter MCM-41, the absolute value of the slope of the tendency line indicating the decrease of the P_v with the loading was higher (35) than the value estimated for the tendency line in the 9 nm pore diameter CC (20), indicating that the pores were more easily blocked in the MCM-41 silica (Fig. 3.22).

3.3.2.7 Molecular simulation

3-aminopropylsilane (AP), with a terminal primary amine (-NH_2) (Fig. 3.13b, respectively) was used for the simulations. The option of grafting the complete hydrolyzed molecule ($NH_2(CH_2)_3Si(OH)_2O$-) [17] was preferred against the more common choice of adding only the organic part ($NH_2(CH_2)_3$-) [64]. The surface chemistry in the model was simplified by considering that all the functionalized chains are covalently tethered to the surface in a monodentate manner and that siloxane bridges are not formed between neighboring chains. The surface AP groups were introduced to the silica models by

randomly replacing a fixed amount of silanols by the first oxygen of the AP molecules, and then growing the rest of the AP molecule using a configurational bias algorithm [17]. For the MCM-41 model, amine loading concentrations of 1.0 and 2.0 mmol/g were studied. For the SG_{40} model, the support tolerated a maximum amine concentration of 0.5 mmol/g. This amine concentration was similar to the one obtained for experimental materials based on SG_{40} (sample 4-MAP@SG_{40}). Similar reasons to the functionalization using alkylsilanes are found for the apparently low values for the maximum amine concentration in the silica gel. Table 3.5 shows the textural properties of the raw and aminosilanized samples, obtained from analysis of the N_2 adsorption isotherms.

Table 3.5 Adsorption properties of the experimental samples and model materials. Amine loading, expressed as mmol of amine per gram of dry substrate (ρ_{graft}), pore diameter (P_d), pore volume (P_v) and surface area (S_a).

Sample	ρ_{graft} [mmol g^{-1}]	P_v [cm^3 g^{-1}]	S_a [m^2 g^{-1}]
MCM41	-	1.02	1137
5-MAP@MCM41	1.03	0.80	841
11-MAP@MCM41	2.08	0.40	411
$MCM41_S$	-	0.81	1134
5-AP@$MCM41_S$	1.0	0.67	961
11-AP@$MCM41_S$	2.0	0.47	573
SG_{40}	-	0.54	563
4-MAP@SG_{40}	0.53	0.54	538
SG_{40_S}	-	0.40	479
4-AP@SG_{40_S}	0.5	0.37	395

MCM-41

The N_2 adsorption isotherms obtained experimentally were compared to the predictions obtained by GCMC simulations. This comparison of the experimental and simulated adsorption isotherms for MCM-41 is shown in Figure 3.23a.

For the raw support, the shape of the isotherm was the same in the experimental and simulated materials, indicating mesoporosity in both cases. However, the accessible

volume of the experimental material was to some extent larger than that of the model. This underestimation in the simulated value was caused by a slightly smaller pore size in the MCM-41 model than in the experimental material (Table 3.5). This smaller pore size of the model with respect to the experimental material was reflected in the filling point. This point was found at a lower relative pressure for the model than for the experimental materials. However, it was consistent for both simulations and experiments, for all the samples, the higher the amount of loaded amine, the lower the relative pressure where this point appeared.

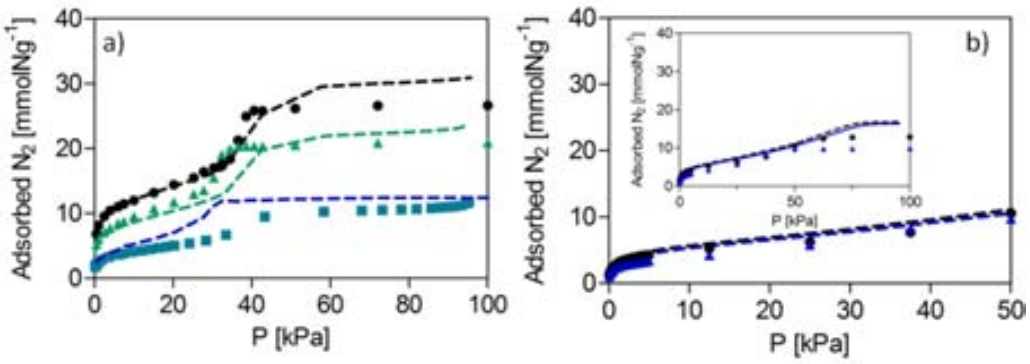

Figure 3.23 N_2 adsorption isotherms for synthesized and modeled MCM-41(a) and SG_{40} (b) samples. Symbols correspond to simulations while dashed lines to experimental isotherms. In (a) black color correspond to MCM-41 bare substrate, green to 5-MAP@MCM41 and 5-AP@MCM41, and blue to 11-MAP@MCM41 and 11-AP@MCM41. In (b) black color corresopnd to SG_{40} and SG_{4_S} bare substrate and blue to 4-MAP@SG_{40} and 4-AP@SG_{40_S}.

Figure 3.23a shows that after functionalization with *ca.* 1 mmol g^{-1} of aminosilane the reduction in the N_2 adsorption capacity for the model and the experimental materials was similar. At 50 kPa, the N_2 adsorption for both MCM41 and $MCM41_S$, functionalized with 1 mmol g^{-1}, was reduced in *ca.* 25 %. However, a decrease of *ca.* 55% and 65 % was estimated for deposited aminosilane concentrations of *ca.* 2 mmol g^{-1} in samples 11-MAP@MCM41 and 11-AP@$MCM41_S$, respectively. This difference is an artifact resulting of the low temperature of the measurements, in Monte Carlo simulations the molecules are adsorbed in the available pore space without considering the trajectory, thus pore blocking and diffusion problems are not present in this kind of simulations. At -196

ºC the grafted chains are in a solid state, therefore experimental blockage and diffusion problems are expected to occur and these experimental issues are highlighted in the materials with the highest amine loading. Thus the material with a higher loading of functionalized chains shows a larger influence of blocking and diffusion on the results.
Nevertheless, the MCM-41 models employed in this work accurately reproduce the adsorption behavior of the experimental materials and can be used to analyze and aid in the characterization of these mesoporous hybrid supports.

Silica gel

For the silica gel materials, the smaller pore size of bare silica gel in the model SG_{40_S} with respect to the experimental material SG_{40}, is reflected in the textural data (Table 3.5). The model of the pristine SG_{40_S} represents the microporous section and the smaller mesopores of the experimental adsorbents, and does not represent the larger mesoporous section of the silica gel materials. A more accurate replication in the silica gel model of the complete pore size distribution of the mesopores in SG_{40_S} was not practical, due to the computational constraints of the simulation cell size, and it was not justified for the present study. Nevertheless, qualitative information can be extracted from the SG_{40_S} model by comparing with the experimental adsorption data on the silica gel products at low pressures (< 50 kPa), since under these conditions the extra-adsorption observed for the experimental materials occurring in large mesopores and macropores is not significant. The N_2 adsorption isotherms for the model and experimental silica gel material are shown in Figure 3.23b. The inset in Figure 3.23b shows the full isotherm of the materials, it is seen that after 50 kPa saturates due to its smaller pore space available after functionalization.

For the experimental and simulated silica gel matrix, it was not possible to increase the aminosilane loading further of 0.5 mmol g^{-1}. This is because of a combination of the low surface area of the silica gel material, the number of silanols available for substitution, which are not as abundant on the surface as in MCM-41, and the internal shape of the pores, formed by the superposition of silica spheres, which hinder the grafting of amine moieties in the locations where two spheres connect.

The SG_{40_S} model gives an accurate representation of the experimental SG_{40} material at pressures below *ca.* 50 kPa. A similar N_2 adsorption behavior was observed for the models and experimental raw materials (Figure 3.23b). Although the capacity of the material was underpredicted by the model, its behavior was correctly captured, especially at low and intermediate partial pressures. This is seen in the 4-MAP@SG_{40_S}, although this model correctly reproduces the main features of 4-MAP@SG_{40} at P > 50 kPa, the lower capacity of this model means that after functionalization with aminosilane the available pore space decreased to a larger extent than it did for the experimental material. The effect of functionalization on the adsorption behavior of 4-MAP@SG_{40} was very low. The SG_{40} and 4-MAP@SG_{40} materials showed almost identical adsorption isotherms. The model materials showed very similar adsorption profiles as well.

For the experimental silica gel material the decrease in the pore volume after functionalization was relatively low. Sample 4-MAP@SG_{40} had an amine loading in the order of 0.5 mmol g^{-1} (0.6 molec nm^{-2}) and less than 1% of decrease in the pore volume with respect to SG_{40}. However, for MCM-41 samples with similar loading, the decrease in the pore volume of the samples was more dramatic. This difference is attributed to the smaller pore diameter of the former material. For samples 5-MAP@MCM41 and 5-AP@$MCM41_S$, with aminosilane surface densities in the order of 1.0 mmol g^{-1} (0.5-0.6 molec nm^{-2}) the decrease in the available pore volume was *ca.* 20 %. This decrease in the pore volume observed in the experimental and model of MCM-41 was similar to the decrease observed in the model silica gel, 4-AP@SG_{40_S}, where P_v decreased *ca.* 8 % respect to the raw material, SG_{40_S}. In general, mesoporous materials with larger pore opening are more adequate to accommodate a monolayer of packed monoamine chains on the intra-channel surface than materials with smaller pore size, even if their total surface area available for grafting is relatively low. Thus, the model silica gel is a correct representation of the micropores and the smaller mesopores of the experimental silica gel, as seen from the adsoption isotherms and the maximum amine loading obtained. However, the larger mesopores and macropores of the experimental material are responsible for a small effect of the loading of the chains on the total pore volume.

At lower relative pressures the results of the silica gel model are similar to those of the experimental material. For instance, for the experimental and model functionalized samples (samples 4-MAP@SG_{40} and 4-AP@SG_{40_S}, respectively), the N_2 adsorbed amount at 50 kPa was reduced by less than 10 % (Fig. 3.23b) with respect to the raw materials. As aforementioned, functionalization of the silica gel materials has a less marked effect on the experimental materials due to its larger pore volume, thus, the effect of pore obstruction and diffusion limitations after functionalization is less noticeable.

The N_2 adsorption results demonstrate that, even though the model of hybrid materials required simplifications related to the cell size and aminosilane polymerization modes for practical computational reasons, it is possible to obtain an adequate insight of what happens in the macroscopic systems at low pressures. The models were able to accurately capture the reduction in the N_2 adsorption capacity as the concentration of grafted aminosilane molecules increased.

3.4 POLYMERIZATION OF ETHYLENEIMINE UNDER COMPRESSED CO_2

Polymers containing amino groups (aminopolymers) are used to impregnate porous silica to obtain materials for CO_2 adsorption and separation processes. Grafted hyperbranched aminopolymers are preferred as modifiers versus aminosilanes, as they have a higher amine density, which is considered advantageous in CO_2 adsorption applications [65].

The incorporation of aminopolymers into porous silica can be carried out by two synthetic routes. The first method consists on introducing a constituted polymer directly into the porous silica. Polyethyleneimine is a common polymer used in this approach [66-70]. The second method is based on the in situ functionalization of a monomer inside the silica pores to obtain the aminopolymer. Ring-opening polymerization of cyclic monomers occurring on the support surface is a method applied for various polymers, including polypeptides and polyethyleneimine [71-75]. Ethyleneimine has been used to obtain hyperbranched polyethyleneimine by ring-opening polymerization with very high yields [1, 70, 74, 76-78]. Such polymerization has been conventionally carried out by the liquid phase route, requiring the use of organic solvents, small amounts of acetic acid as a

catalyst and high temperatures [1, 70, 77, 79, 80]. A free-solvent process, based on a vapor phase transport route, has been recently described [76]. Although the use of organic solvents was avoided in this process, still long reaction times of 24 h and temperatures close to 80 ºC were required to obtain significant loadings. In this thesis, an effective and fast procedure was developed for the in situ ring-opening polymerization of aziridine into porous silica, using compressed CO_2 both as a reaction medium and catalyst.

3.4.1 Functionalization procedure

Ethyleneimine monomer was polymerized inside of the mesoporous susbtrates CC and MCM-41 using compressed CO_2 as a solvent, reaction medium and catalyst. The ring-opening polymerization of ethyleneimine (aziridine) into mesoporous silica was promoted by using compressed CO_2 above and below the critical point (Fig. 3.24). Experiments were performed on the 100 mL high pressure autoclave (ThaDesign), using a similar set up to the one used for organosilane. 0.3 g of the porous silica substrate, enclosed in a cartridge, were placed in the stainless steel support. Then, 1mL of aziridine was carefully added to the bottom of the reactor. (*Aziridine is a hazardous compound that must be handled with the corresponding safety precautions: work in a fume cupboard using rubber gloves and protection glasses*). The vessel was slowly pressurized with CO_2 at ambient temperature. At *ca.* 1 MPa, the formation of a dense vapor cloud was visually observed together with a simultaneous increase on the temperature of 4-6 ºC, evidencing the exothermic character of the ring-opening polymerization of aziridine. Operating temperature and reaction time were set at 45 ºC and 10 min, respectively, while the pressure was varied between 6 and 10 MPa. Pressure conditions of each run are shown in Table 3.6, together with some products characteristics. A blank supercritical polymerization experiment was performed under similar conditions, but without the addition of the solid support (Table 3.4). The polymer recovered from this experiment was labeled as PEI.

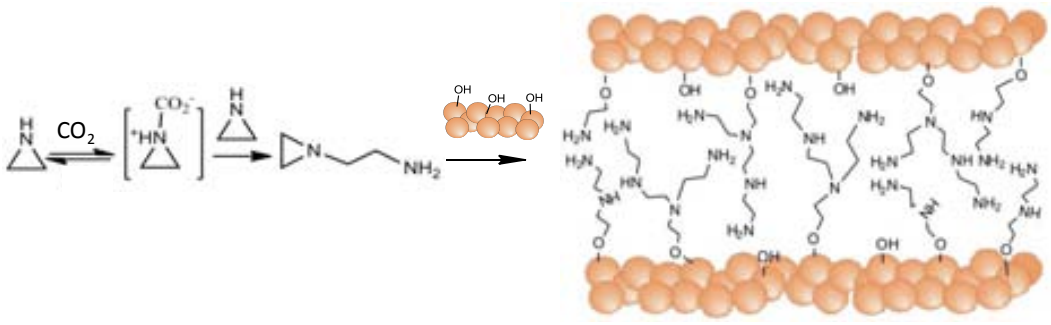

Figure 3.24 Schematic represenation of the ring -opening polymerization m echanism of ethyleneimine using compressed CO_2. Polymeriation is ca rrie out in situ inside a mesoporous silica substrate.

Table 3.6 Pressure conditions for some of the obtained samples and their characteristic values of amine loading (ρ_N), specific surface area (S_a) and pore volume (V_p).

Sample	P [MPa]	ρ_N [mmol N g^{-1}]	ρ_{mgraft} [molecnm^{-2}]	S_a [m^2g^{-1}]	V_p [cm^3g^{-1}]
MCM-41	-	-	-	1127	0.92
1- PEI_{CO2}@MCM41	8.5	4.6	2.5	530	0.40
2-PEI_{CO2}@MCM41	6.0	6.0	3.2	306	0.25
3- PEI_{CO2}@MCM41	10	8.0	4.2	50	0.07
CC		-		440	0.96
1- PEI_{CO2}@CC	8.5	3.0	4.1	307	0.70
2- PEI_{CO2}@CC	6.0	3.3	4.5	251	0.61
3- PEI_{CO2}@CC	10	4.3	5.9	234	0.54
PEI	6.0	-	-	-	-

4.2 Polymerization mechanism

PEI is a water soluble cationic polymer that can take both linear and branched forms [81]. The random branched structure is commonly produced by acid-catalyzed polymerization of aziridine monomers in aqueous or alcoholic solution [82, 83]. The polymerization is activated by aziridine protonation, followed of nucleophilic attack by a second aziridine molecule [Fig. 3.25a]. The ring opening polymerization can also be

initiated by a Lewis acid, such as CO_2 (Fig. 3.25b) [84]. It has been stated that unsubstituted aziridine reacts with CO_2 to give a homopolymer in the absence of catalyst, i.e., CO_2 is not incorporated into the polymer [85]. Unsubstituted aziridine reversibly generates the corresponding carbamic acid derivative in equilibrium with the corresponding ammonium carbamate [86]. The CO_2 sorbed into the synthesized PEI polymer is easily eliminated at temperatures of 80–100 ºC [87]. Therefore, it is expected that the polymerization of aziridine in compressed CO_2 would lead to a hyperbranched polyethyleneimine [Fig. 3.25a].

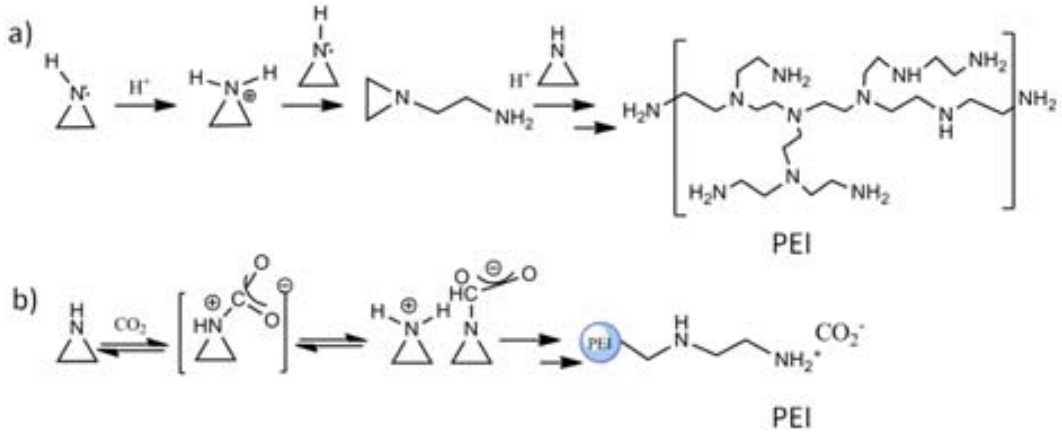

Figure 3.25 Schematic representation of different mechanisms established for the formation of hyperbranched PEI from aziridine under: (a) acid, and (b) CO_2 catalysis.

3.4.3 Polymer molecular weight and structure

For PEI polymers, the average molecular weight achieved following the conventional liquid synthesis mode is typically within the range of 20–50 kDa [85]. The molecular weight of a compressed CO_2 polymerized ethyleneimine sample (labeled as PEI) was first determined using a SLS method. The estimated value was in the order of 8±2 kDa, which corresponds to a low PEI molecular weight. To contrast the results, the PEI sample was also characterized by using the MALDI-ToF equipment. Significant amounts of 0.2–1 kDa chains were detected in the PEI by this technique (Fig. 3.26a), indicating a low molecular weight for the synthesized polymer, in agreement with the results obtained by SLS.

Discrepancies on the absolute mass estimated using different characterization techniques are typical for such a low-molecular weight polymers, shifting the molecular weight distribution to lower masses for MALDI-ToF analysis [88]. The maximum peak intensity was centered at 132–304 Da, corresponding to 3 (129 Da) to 7 (301 Da) repeating units (CH_2CH_2NH) in the protonated PEI molecule. The process of PEI polymerization in aqueous or alcoholic solution occurs in a homogeneous mixture, because of the high solubility of the monomer, the polymer, and the acid initiator in the continuous liquid phase. Solubilization of the polymer during polymerization results in the formation of high-molecular weight PEI. In contrast, due to the limited solubility of polymers in compressed CO_2, low molecular weight polymers are frequently obtained in supercritical and compressed CO_2 in the absence of surfactants [89]. The ring opening polymerization process carried out in the compressed fluid occurs at high reaction rates, since aziridine undergoes exothermic polymerization in contact with CO_2 [90]. The quick heat release vaporized the monomer resulting in a visually observed vapor cloud, occurring at about 5 MPa. Hence, the process featured an initially homogeneous vapor phase reaction, where monomer and initiator (in this case, the Lewis acid CO_2) are homogeneously mixed. During polymerization, the system became rapidly heterogeneous once the growing oligomeric chains reach a critical molar mass that exceeds the solubility limit in the compressed CO_2 vapor phase. Polymer precipitation would significantly reduce the molecular weight of the recovered PEI. In addition, polymer chains grafted on silica surface are expected to have a lower molecular weight than the value found for PEI in bulk, due to factors related to strong steric hindrance occurring between the pendant polymer chains [91]. The high density of chains grafted onto the porous silica surface would interfere with the propagation of the hyperbranched tree-like structure, resulting in the decrease of the apparent molecular weight [92, 93].

XRD analysis of synthesized PEI indicated that the polymer has an amorphous structure (Fig. 3.26b), which suggested a highly branched configuration. Amorphous PEI synthesized in CO_2 exhibited a glass transition step between 50 and 90 ºC (Fig. 3.26c), which is similar to the one described for the 25 kDa commercial PEI centered at about 65 ºC [94].

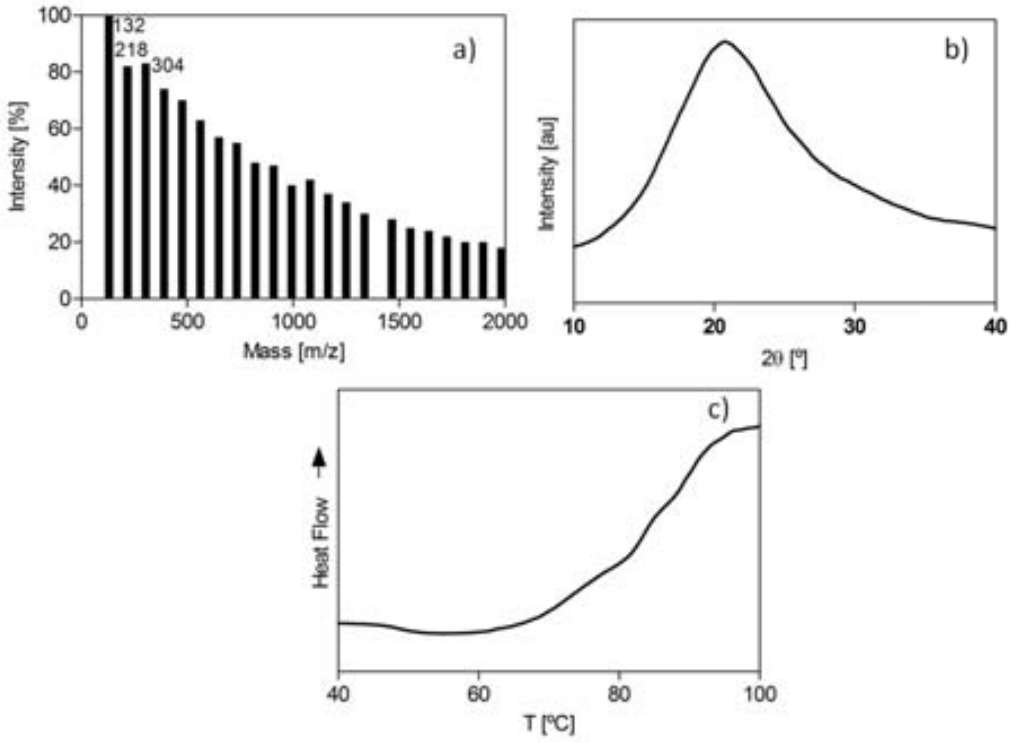

Figure 3.26 Characterization of synthesized PEI polymer: (a) MALDI-ToF mass spectrum, (b) Xray diffractogram, and (c) DSC curve.

3.4.4 Thermal analysis and grafting density

Mesoporous substrates MCM-41 and CC were in situ functionalized with ethyleneimine following the described polymerization method using CO_2. Table 3.4 shows the values of the amine loading and the textural properties of the prepared samples.

The thermal behavior and the loadings of functionalized samples were determined by thermogravimetric analysis. The amine content was calculated from the TGA weight loss in the temperature range of 200–500 ºC (Table 3.6). Besides, data were corroborated by elemental analysis for samples 2-PEI@MCM41 and 2-PEI@CC giving loading values of 5.4 and 3.4 mmol g^{-1}, respectively, consistent with the values estimated by TGA (Table 3.6).

Figure 3.27a,b shows the thermogravimetric profiles of PEI functionalized MCM-41 and CC supports. For both supports, the first weight decay occurring up to 150 ºC

corresponded to the loss of water and CO_2. A second weight loss occurred between 200-500 ºC and was associated to the loss of PEI.

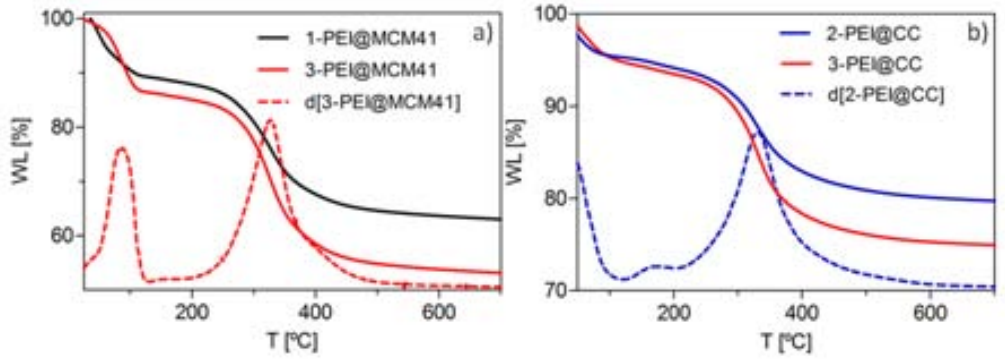

Figure 3.27 Thermogravimetric profiles of PEI functionalized samples. MCM-41 suppport loaded with 4.6 and 8.0 mmolNg^{-1} of PEI (samples 1- and 3-PEI@MCM41, respectively) (a) and CC support loaded with 3.3 and 4.3 mmolNg^{-1} of PEI (samples 2- and 3-PEI@CC, respectively). Weight derivatives are represented by discontinuous lines.

3.4.5 Comparison of the thermal behavior with similar samples from literature

Fig. 3.28 illustrates the normalized derivative curves of the TGA weight loss profiles measured for 2- and 3-PEI@MCM samples. Derivative curves were compared with literature data of similar products involving PEI and mesoporous SBA-15, with loadings ranging from 4-9 mmol g^{-1} (Table 3.7), prepared by ring-opening polymerization following the liquid [77, 78] or the vapor diffusion route [76]. Samples prepared using conventional routes decomposed at temperatures of 200–250 ºC, while samples synthesized in this work attained a temperature of *ca.* 340 ºC before significant decomposition. Hence, the maximum in the derivative of the decomposition profiles of samples prepared using compressed CO_2 was shifted more than 100 ºC, indicating notable higher thermal stability than similar products reported in the literature.

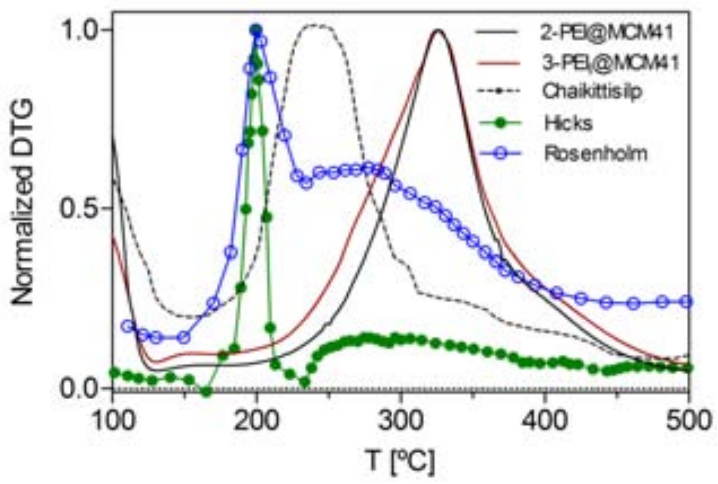

Figure 3.28 Normalized derivative profiles obtained from the TGA weight loss curves of 2- and 3-PEI@MCM samples and literature data [76-78].

Table 3.7 Comparison of the amine content and pore volume of samples from this work with similar samples from the literature.

Sample	ρ_N [mmol g^{-1}]	V_p [$cm^3 g^{-1}$]	Ref
2-PEI_{CO2}@MCM41	6	0.21	This work
3- PEI_{CO2}@MCM41	8	0.07	This work
MCM-41	6	0.01	[80]
SBA-15	7-9	0.33-0.07	[76]
SBA-15	4	0.36	[80]
SBA-15	7.4	1.19	[95]

3.4.6 Textural properties

Figure 3.29 illustrates the N_2 adsorption isotherms for bare and modified MCM-41 and CC substrates. A decrease in the available surface area and BJH pore volume is observed for both substrates (Table 3.6). The highest decrease in these values was found for samples with increasing aminopolymer loading. For sample 1-PEI@MCM41, containing 4.6 mmol

g^{-1}, the pore volume and surface area values decreased in *ca.* 55 %. Sample 3-PEI@MCM41, with 8 mmol g^{-1}, exhibited almost no N_2 adsorption (Fig. 3.21a) with a 73 % decrease in the pore volume.

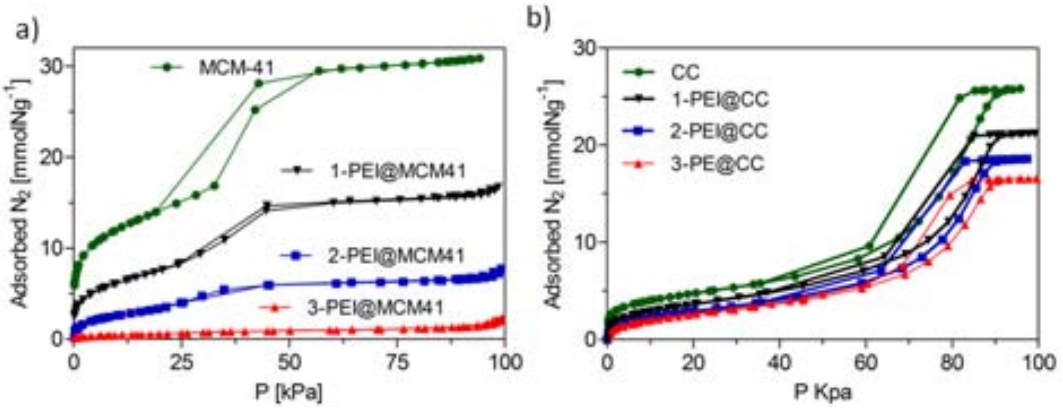

Figure 3.29 N_2 adsorption isotherms for PEI modified MCM-41 (a) and CC substrates (b).

Functionalized CC supports exhibited a decrease in the N_2 adsorption with respect to the bare support CC (Fig. 3.29b). The shape of the isotherm remained similar, even for the highest loaded sample 3-PEI@CC. This sample, containing 4.3 mmol g^{-1}, exhibited a decrease of 44 % in the pore volume. Comparing the grafting densities (molec nm^{-2}) of MCM-41 and CC samples (Table 3.6), sample 3-PEI@CC showed the highest grafting value, with *ca.* 6 molec nm^{-2}. However, the decrease in the pore volume for this sample was not as dramatic as in the highest loaded sample for MCM-41 support, the 3-PEI@MCM41 (4.2 molec nm^{-2}). This can be explained by the higher pore diameter in CC samples (9 nm) when comparing to the 4 nm pore diameter of MCM-41. Pore blocking consequently occurs at lower aminopolymer loadings for MCM-41 samples.

3.5 CONCLUSIONS

The internal surface of porous silica was successfully modified with organic functional groups, i.e. alkylsilanes, aminosilanes and aminopolymers, using supercritical CO_2 as the reaction media. Operating conditions were chosen according to the solubility or reactivity of the functional molecules in CO_2. Low pressures and temperatures of 10 MPa and 45 ºC

were sufficient to attain high solubility of alkylsilanes in $scCO_2$. The functionalization with the aminosilane required a previous study to determine the best operating conditions to avoid the formation of unsoluble carabamate species. Those conditions were found to be low pressures (7.5-9.0 MPa) and temperatures of 100-135 ºC, using either pure CO_2 or CO_2 plus a cosolvent.

Thermogravimetric analysis revealed the thermal stability of the synthesized material as well as the grafting densities achieved.

Alkylsilanes and aminosilanes covalently attached to the silica surface were lost at temperatures higher than *ca.* 300 ºC. Grafting densities up to c*a*. 0.85-1.0 molec nm^{-2} were achieved for the mesoporous and microporous substrates CC, SB and ZY functionalized with alkylsilanes. Lower values of ca.0.5 molec nm^{-2} were found for SG_{40} due to steric constrictions of the narrow sterical pores. Only physical deposition was confirmed in the case of zeolite Y, due to the absence of silanol groups.

For aminosilanes, the mesoporous substrate CC, with the largest pore diameter, exhibited the highest grafting density values of *ca.* 4.0 molec nm^{-2}. The highest grafting density for MCM-41 was *ca.* 3 molec nm^{-2}. The smaller pores of *ca.* 4 nm as in MCM-41 are easily blocked. Similar to the alkylsilanes case, low grafting values of *ca.* 0.5 molec nm^{-2} were found for SG_{40}.

Molecular simulations were performed on some of the bare and functionalized substrates and compared with the obtained experimental data. The accuracy of the models for bare zeolite, mesoporous silica gel 40 and MCM-41 were corroborated by comparing the N_2 adsorption simulations with experimental data. A realistic model was obtained for SG_{40} and MCM-41 by grafting the organic chain to the substrate. Next, the experimental and simulated N_2 adsorption isotherms of postsynthesis funtionalized materials were compared to insight the behaviour of the functionalized chains. For the zeolite matrix impregnated with alkylsilane, the simulations accurately predicted the experimental adsorption isotherms in which silane physisorption was expected. For covalently bonded organosilane-functionalized SG_{40} and MCM-41, the organosilane molecules were grafted entirely to the silica surface. Although the model of hybrid materials required simplifications related to the cell size, the models were able to simulate accurately the reduction in the adsorbent capacity due to the increasing pores space occupied by the

hydrolyzed silane as the concentration increased, with a deviation of < 10% with respect to experimental values. In contrast, for a model where only the alkyl chain was grafted to the silica substrate, deviations as high as 55% were found. Moreover, it was shown that the simulation method for covalent functionalization of silica gel described in this work is more realistic in regards to the prediction of the adsorption capacity at different grafting densities than the models that consider only the organic tail of the silane chain as the grafting moiety, at least for concentrations lower than those corresponding to monolayer formation.

In a last approach, ethyleneimine monomer was in situ polymerized into mesoporous silica by using compressed CO_2 as the reaction media and the catalyst of the ring-opening reaction. Low pressures between 6-10 MPa and temperatures of 45 ºC were sufficient for the polymerization reaction. Aminopolymer loadings in mesoporous MCM-41 and CC were as high as 5 and 8 mmol g^{-1}, respectively. The thermal stability of the prepared PEI@MCM-41 samples were compared with similar samples from the literature revealing that samples from this work decomposed at temperatures 100 ºC higher. N_2 adsorption isotherms showed that the decrease in the pore volume at similar aminopolymer densities for MCM-41 and CC substrates was more dramatic for MCM-41than for CC. This is due to the difference in their pore diameters which are two times larger for CC.

3.6 REFERENCES

1. J.H. Drese, S. Choi, R.P. Lively, W.J. Koros, D.J. Fauth, M.L. Gray, and C.W. Jones, *Synthesis–Structure–Property Relationships for Hyperbranched Aminosilica CO2 Adsorbents.* Advanced Functional Materials, 2009, 19(23), 3821.
2. M.R. Mello, D. Phanon, G.Q. Silveira, P.L. Llewellyn, and C.M. Ronconi, *Amine-modified MCM-41 mesoporous silica for carbon dioxide capture.* Microporous and Mesoporous Materials, 2011, 143(1), 174.
3. A.S.M. Chong, X.S. Zhao, A.T. Kustedjo, and S.Z. Qiao, *Functionalization of large-pore mesoporous silicas with organosilanes by direct synthesis.* Microporous and Mesoporous Materials, 2004, 72(1-3), 33.
4. X. Ji, Q. Hu, J.E. Hampsey, X. Qiu, L. Gao, J. He, and Y. Lu, *Synthesis and characterization of functionalized mesoporous silica by aerosol-assisted self-assembly.* Chemistry of Materials, 2006, 18(9), 2265.
5. C.P. Jaroniec, M. Kruk, M. Jaroniec, and A. Sayari, *Tailoring Surface and Structural Properties of MCM-41 Silicas by Bonding Organosilanes.* The Journal of Physical Chemistry B, 1998, 102(28), 5503.
6. K. Sing, *The use of nitrogen adsorption for the characterisation of porous materials.* Colloids and Surfaces A: Physicochemical and Engineering Aspects, 2001, 187–188(0), 3.
7. a rows ki, *Adsorption - From theory to practice.* Advances in Colloid and Interface Science, 2001, 93(1-3), 135.
8. P.H. Emmett and S. Brunauer, *The Use of Low Temperature van der Waals Adsorption Isotherms in Determining the Surface Area of Iron Synthetic Ammonia Catalysts.* Journal of the American Chemical Society, 1937, 59(8), 1553.
9. S. Brunauer, P.H. Emmett, and E. Teller, *Adsorption of Gases in Multimolecular Layers.* Journal of the American Chemical Society, 1938, 60(2), 309.
10. G. Fagerlund, *Determination of specific surface by the BET method.* Mat. Constr., 1973, 6(3), 239.
11. G.E. Romanos, O.C. Vangeli, K.L. Stefanopoulos, E.P. Kouvelos, S.K. Papageorgiou, E.P. Favvas, and N.K. Kanellopoulos, *Methods of evaluating pore morphology in hybrid organic–inorganic porous materials.* Microporous and Mesoporous Materials, 2009, 120(1–2), 53.
12. J.E.S. S. Lowell, *Characterization of porous solids and powders: surface area, pore size and density*2004The netherlands: Kluwer Academic Publishers.
13. E.P. Barrett, L.G. Joyner, and P.P. Halenda, *The Determination of Pore Volume and Area Distributions in Porous Substances. I. Computations from Nitrogen Isotherms.* Journal of the American Chemical Society, 1951, 73(1), 373.
14. B.C. Lippens and J.H. De Boer, *Studies on pore systems in catalysts: V. The t method.* Journal of Catalysis, 1965, 4(3), 319.

15. E.C. Moloy, L.P. Davila, J.F. Shackelford, and A. Navrotsky, *High-silica zeolites: A relationship between energetics and internal surface areas.* Microporous and Mesoporous Materials, 2002, 54(1-2), 1.
16. A. Software, *Materials Studio*, 2010: San Diego.
17. S. Builes and L.F. Vega, *Understanding CO 2 capture in amine-functionalized MCM-41 by molecular simulation.* Journal of Physical Chemistry C, 2012, 116(4), 3017.
18. J.M.D. Macelroy and K. Raghavan, *Adsorption and diffusion of a Lennard-Jones vapor in microporous silica.* The Journal of Chemical Physics, 1990, 93(3), 2068.
19. J.M.D. Macelroy and K. Raghavan, *Transport of an adsorbing vapour in a model silica system.* Journal of the Chemical Society, Faraday Transactions, 1991, 87(13), 1971.
20. S. Gavalda, K.E. Gubbins, Y. Hanzawa, K. Kaneko, and K.T. Thomson, *Nitrogen adsorption in carbon aerogels: A molecular simulation study.* Langmuir, 2002, 18(6), 2141.
21. L.N. Ho, J. Perez Pellitero, F. Porcheron, and R.J.M. Pellenq, *Enhanced CO2 solubility in hybrid MCM-41: Molecular simulations and experiments.* Langmuir, 2011, 27(13), 8187.
22. L.N. Ho, J. Perez Pellitero, F. Porcheron, and R.J.M. Pellenq, *Enhanced CO 2 solubility in hybrid MCM-41: Molecular simulations and experiments.* Langmuir, 2011, 27(13), 8187.
23. S. Builes and L.F. Vega, *Effect of immobilized amines on the sorption properties of solid materials: Impregnation versus grafting.* Langmuir, 2013, 29(1), 199.
24. E. Loste, J. Fraile, M.A. Fanovich, G.F. Woerlee, and C. Domingo, *Anhydrous supercritical carbon dioxide method for the controlled silanization of inorganic nanoparticles.* Advanced Materials, 2004, 16(8), 739.
25. C.A. García-González, J. Fraile, A. López-Periago, and C. Domingo, *Preparation of silane-coated TiO2 nanoparticles in supercritical CO2.* Journal of Colloid and Interface Science, 2009, 338(2), 491.
26. C Garćia-González, J. Saurina, J.A. Ayllón, and C. Domingo, *Preparation and characterization of surface silanized TiO2 nanoparticles under compressed CO2: Reaction kinetics.* Journal of Physical Chemistry C, 2009, 113(31), 13780.
27. K. Kaneko, *Micropore filling mechanism in inorganic sorbents*, in *Studies in Surface Science and Catalysis*1996. p. 573.
28. C Garc a-Gon e , Fraile, e -Periago, J. Saurina, and C.N. Domingo, *Measurements and Correlation of Octyltriethoxysilane Solubility in Supercritical CO2 and Assembly of Functional Silane Monolayers on the Surface of Nanometric Particles.* Industrial & Engineering Chemistry Research, 2009, 48(22), 9952.
29. J. Chrastil, *Solubility of solids and liquids in supercritical gases.* The Journal of Physical Chemistry, 1982, 86(15), 3016.
30. C.A. García-Gon a Íe , Fraile, o ṕez-Periago, J. Saurina, and C. Domingo, *Measurements and correlation of octyltriethoxysilane solubility in supercritical CO2 and assembly of functional silane monolayers on the surface of nanometric particles.* Industrial and Engineering Chemistry Research, 2009, 48(22), 9952.

31. P. López-Aranguren, J. Saurina, L.F. Vega, and C. Domingo, *Sorption of tryalkoxysilane in low-cost porous silicates using a supercritical CO2 method.* Microporous and Mesoporous Materials, 2012, 148(1), 15.
32. Y. Liu, R. Yang, J. Yu, and K. Wang, *Investigation of interfacial structure of coupling agent treated fillers by Fourier transform infrared spectroscopy and attenuated total reflection-FTIR spectroscopy.* Polymer Composites, 2002, 23(1), 28.
33. A.Y. Fadeev, R. Helmy, and S. Marcinko, *Self-assembled monolayers of organosilicon hydrides supported on titanium, zirconium, and hafnium dioxides.* Langmuir, 2002, 18(20), 7521.
34. J. Mcelwee, R. Helmy, and A.Y. Fadeev, *Thermal stability of organic monolayers chemically grafted to minerals.* Journal of Colloid and Interface Science, 2005, 285(2), 551.
35. C.A. García-González, J.M. Andanson, S.G. Kazarian, C. Domingo, and J. Saurina, *Application of principal component analysis to the thermal characterization of silanized nanoparticles obtained at supercritical carbon dioxide conditions.* Analytica Chimica Acta, 2009, 635(2), 227.
36. R.P.W. Scott, *Physical Chemistry Resources*. Vol. Book V, Thermal Analysis.
37. M.B. Smith, K. Efimenko, D.A. Fischer, S.E. Lappi, P.K. Kilpatrick, and J. Genzer, *Study of the packing density and molecular orientation of bimolecular self-assembled monolayers of aromatic and aliphatic organosilanes on silica.* Langmuir, 2007, 23(2), 673.
38. A.Y. Fadeev and T.J. Mccarthy, *Self-assembly is not the only reaction possible between alkyltrichlorosilanes and surfaces: monomolecular and oligomeric covalently attached layers of dichloro- and trichloroalkylsilanes on silicon.* Langmuir, 2000, 16(18), 7268.
39. R. Mueller, H.K. Kammler, K. Wegner, and S.E. Pratsinis, *OH surface density of SiO2 and TiO2 by thermogravimetric analysis.* Langmuir, 2003, 19(1), 160.
40. C. Cao, A.Y. Fadeev, and T.J. Mccarthy, *Reactions of organosilanes with silica surfaces in carbon dioxide.* Langmuir, 2001, 17(3), 757.
41. S. Marcinko, R. Helmy, and A.Y. Fadeev, *Absorption properties of SAMs supported on TiO2 and ZrO2.* Langmuir, 2003, 19(7), 2752.
42. C. Schumacher, J. Gonzalez, M. Pérez-Mendoza, P.A. Wright, and N.A. Seaton, *Design of hybrid organic/inorganic adsorbents based on periodic mesoporous silica.* Industrial and Engineering Chemistry Research, 2006, 45(16), 5586.
43. J.J. Williams, A.D. Wiersum, N.A. Seaton, and T. Düren, *Effect of surface group functionalization on the CO2/N 2 separation properties of MCM-41: A grand-canonical Monte Carlo simulation study.* Journal of Physical Chemistry C, 2010, 114(43), 18538.
44. J.J. Williams, N.A. Seaton, and T. Düren, *Influence of surface groups on the diffusion of gases in MCM-41: A molecular dynamics study.* Journal of Physical Chemistry C, 2011, 115(21), 10651.
45. M.G. Martin and J.I. Siepmann, *Novel configurational-bias Monte Carlo method for branched molecules. Transferable potentials for phase equilibria. 2. United-atom description of branched alkanes.* Journal of Physical Chemistry B, 1999, 103(21), 4508.

46. M.G. Martin and A.L. Frischknecht, *Using arbitrary trial distributions to improve intramolecular sampling in configurational-bias Monte Carlo.* Molecular Physics, 2006, 104(15), 2439.
47. F.J. Blas and L.F. Vega, *Thermodynamic behaviour of homonuclear and heteronuclear Lennard-Jones chains with association sites from simulation and theory.* Molecular Physics, 1997, 92(1), 135.
48. S. Builes, T. Roussel, and L.F. Vega, *Optimization of the separation of sulfur hexafluoride and nitrogen by selective adsorption using monte carlo simulations.* AIChE Journal, 2011, 57(4), 962.
49. R.Q. Snurr, A.T. Bell, and D.N. Theodorou, *Prediction of adsorption of aromatic hydrocarbons in silicalite from grand canonical Monte Carlo simulations with biased insertions.* Journal of Physical Chemistry, 1993, 97(51), 13742.
50. K.S.W. Sing, D.H. Everett, R.a.W. Haul, L. Moscou, R.A. Pierotti, J. Rouquerol, and T. Siemieniewska, *Reporting Physisorption Data for Gas/Solid Systems*, in *Handbook of Heterogeneous Catalysis*,2008, Wiley-VCH Verlag GmbH & Co. KGaA.
51. G.M. Davies and N.A. Seaton, *Development and validation of pore structure models for adsorption in activated carbons.* Langmuir, 1999, 15(19), 6263.
52. K. Kaneko, *Determination of pore size and pore size distribution. 1. Adsorbents and catalysts.* Journal of Membrane Science, 1994, 96(1-2), 59.
53. C. Schumacher, J. Gonzalez, P.A. Wright, and N.A. Seaton, *Generation of atomistic models of periodic mesoporous silica by kinetic Monte Carlo simulation of the synthesis of the material.* Journal of Physical Chemistry B, 2006, 110(1), 319.
54. J.P. Dacquin, H.E. Cross, D.R. Brown, T. Düren, J.J. Williams, A.F. Lee, and K. Wilson, *Interdependent lateral interactions, hydrophobicity and acid strength and their influence on the catalytic activity of nanoporous sulfonic acid silicas.* Green Chemistry, 2010, 12(8), 1383.
55. R. Helmy and A.Y. Fadeev, *Self-assembled monolayers supported on TiO2: Comparison of C18H37SiX3 (X = H, Cl, OCH3), C18H37Si(CH3)2Cl, and C18H37PO(OH)2.* Langmuir, 2002, 18(23), 8924.
56. C. Schumacher, J. Gonzalez, P.A. Wright, and N.A. Seaton, *Packing of adsorbed molecules in microporous polymorphs aluminium methylphosphonates α and β.* Physical Chemistry Chemical Physics, 2005, 7(11), 2351.
57. V. Zelenak, D. Halamova, L. Gaberova, E. Bloch, and P. Llewellyn, *Amine-modified SBA-12 mesoporous silica for carbon dioxide capture: Effect of amine basicity on sorption properties.* Microporous and Mesoporous Materials, 2008, 116(1–3), 358.
58. V.V. Mahajani and J.B. Joshi, *Kinetics of reactions between carbon dioxide and alkanolamines.* Gas Separation and Purification, 1988, 2(2), 50.
59. Z. Bacsik, N. Ahlsten, A. Ziadi, G. Zhao, A.E. Garcia-Bennett, B. Martín-Matute, and N. Hedin, *Mechanisms and kinetics for sorption of CO 2 on bicontinuous mesoporous silica modified with n-propylamine.* Langmuir, 2011, 27(17), 11118.
60. H.R. Baker, E.G. Shafrin, and W.A. Zisman, *The adsorption of hydrophobic monolayers of carboxylic acids.* Journal of Physical Chemistry, 1952, 56(3), 405.

61. H. Yoshitake, T. Yokoi, and T. Tatsumi, *Adsorption of chromate and arsenate by amino-functionalized MCM-41 and SBA-1.* Chemistry of Materials, 2002, 14(11), 4603.

62. F.Y. Chang, K.J. Chao, H.H. Cheng, and C.S. Tan, *Adsorption of CO2 onto amine-grafted mesoporous silicas.* Separation and Purification Technology, 2009, 70(1), 87.

63. Z.J. Dijkstra, A.R. Doornbos, H. Weyten, J.M. Ernsting, C.J. Elsevier, and J.T.F. Keurentjes, *Formation of carbamic acid in organic solvents and in supercritical carbon dioxide.* Journal of Supercritical Fluids, 2007, 41(1), 109.

64. S. Builes, P. López-Aranguren, J. Fraile, L.F. Vega, and C. Domingo, *Alkylsilane-functionalized microporous and mesoporous materials: Molecular simulation and experimental analysis of gas adsorption.* Journal of Physical Chemistry C, 2012, 116(18), 10150.

65. S. Choi, J.H. Drese, and C.W. Jones, *Adsorbent Materials for Carbon Dioxide Capture from Large Anthropogenic Point Sources.* ChemSusChem, 2009, 2(9), 796.

66. X. Xu, C. Song, J.M. Andresen, B.G. Miller, and A.W. Scaroni, *Novel polyethylenimine-modified mesoporous molecular sieve of MCM-41 type as high-capacity adsorbent for CO2 capture.* Energy and Fuels, 2002, 16(6), 1463.

67. X. Xu, C. Song, B.G. Miller, and A.W. Scaroni, *Influence of moisture on CO2 separation from gas mixture by a nanoporous adsorbent based on polyethylenimine-modified molecular sieve MCM-41.* Industrial and Engineering Chemistry Research, 2005, 44(21), 8113.

68. W.J. Son, J.S. Choi, and W.S. Ahn, *Adsorptive removal of carbon dioxide using polyethyleneimine-loaded mesoporous silica materials.* Microporous and Mesoporous Materials, 2008, 113(1-3), 31.

69. X. Xu, C. Song, B.G. Miller, and A.W. Scaroni, *Adsorption separation of carbon dioxide from flue gas of natural gas-fired boiler by a novel nanoporous "molecular basket" adsorbent.* Fuel Processing Technology, 2005, 86(14-15), 1457.

70. J.C. Hicks, J.H. Drese, D.J. Fauth, M.L. Gray, G. Qi, and C.W. Jones, *Designing adsorbents for CO2 capture from flue gas-hyperbranched aminosilicas capable of capturing CO2 reversibly.* Journal of the American Chemical Society, 2008, 130(10), 2902.

71. C. Gao and D. Yan, *Hyperbranched polymers: from synthesis to applications.* Progress in Polymer Science, 2004, 29(3), 183.

72. J. Cheng and T.J. Deming, *Synthesis of polypeptides by ring-opening polymerization of α-Amino acid N-carboxyanhydrides*, in *Topics in Current Chemistry*2012. p. 1.

73. C. Chen, D. Wu, W. Fu, and Z. Li, *Peptide Hydrogels Assembled from Nonionic Alkyl-polypeptide Amphiphiles Prepared by Ring-Opening Polymerization.* Biomacromolecules, 2013, 14(8), 2494.

74. H.J. Kim, J.H. Moon, and J.W. Park, *A hyperbranched poly(ethyleneimine) grown on surfaces.* Journal of Colloid and Interface Science, 2000, 227(1), 247.

75. Y. Ito, Y. Ochiai, Y.S. Park, and Y. Imanishi, *pH-Sensitive Gating by Conformational Change of a Polypeptide Brush Grafted onto a Porous Polymer Membrane.* Journal of the American Chemical Society, 1997, 119(7), 1619.

76. W. Chaikittisilp, S.A. Didas, H.-J. Kim, and C.W. Jones, *Vapor-Phase Transport as A Novel Route to Hyperbranched Polyamine-Oxide Hybrid Materials.* Chemistry of Materials, 2013, 25(4), 613.
77. J.M. Rosenholm, A. Penninkangas, and M. Lindén, *Amino-functionalization of large-pore mesoscopically ordered silica by a one-step hyperbranching polymerization of a surface-grown polyethyleneimine.* Chemical Communications, 2006(37), 3909.
78. J.C. Hicks, *Organic/inorganic hybrid amine and sulfonic acid tethered silica materials: synthesis, characterization and application*, in *School of Chemical & Biomolecular Engineering*2007: Georgia Institute of Technology.
79. J.M. Rosenholm and M. Lindén, *Wet-chemical analysis of surface concentration of accessible groups on different amino-functionalized mesoporous SBA-15 silicas.* Chemistry of Materials, 2007, 19(20), 5023.
80. J.H. Drese, S. Choi, S.A. Didas, P. Bollini, M.L. Gray, and C.W. Jones, *Effect of support structure on CO 2 adsorption properties of pore-expanded hyperbranched aminosilicas.* Microporous and Mesoporous Materials, 2012, 151, 231.
81. R. Kircheis, L. Wightman, and E. Wagner, *Design and gene delivery activity of modified polyethylenimines.* Advanced Drug Delivery Reviews, 2001, 53(3), 341.
82. S. Minakata, Y. Okada, Y. Oderaotoshi, and M. Komatsu, *Lewis base catalyzed ring opening of aziridines with silylated nucleophiles.* Organic Letters, 2005, 7(16), 3509.
83. P. Kubisa and S. Penczek, *Cationic activated monomer polymerization of heterocyclic monomers.* Progress in Polymer Science (Oxford), 1999, 24(10), 1409.
84. T. Sakakura, J.C. Choi, and H. Yasuda, *Transformation of carbon dioxide.* Chemical Reviews, 2007, 107(6), 2365.
85. K. Soga, S. Hosoda, and S. Ikeda, *Copolymerization of carbon dioxide and ethyleneimine.* Die Makromolekulare Chemie, 1974, 175(11), 3309.
86. D. Belli Dell'amico, F. Calderazzo, L. Labella, F. Marchetti, and G. Pampaloni, *Converting Carbon Dioxide into Carbamato Derivatives.* Chemical Reviews, 2003, 103(10), 3857.
87. M.J. Schladt, T.P. Filburn, and J.J. Helble, *Supported amine sorbents under temperature swing absorption for CO 2 and moisture capture.* Industrial and Engineering Chemistry Research, 2007, 46(5), 1590.
88. E. Rivera-Tirado and C. Wesdemiotis, *Characterization of polyethylenimine by electrospray ionization and matrix-assisted laser desorption/ionization.* Journal of Mass Spectrometry, 2011, 46(9), 876.
89. F. Rindfleisch, T.P. Dinoia, and M.A. Mchugh, *Solubility of Polymers and Copolymers in Supercritical CO2.* The Journal of Physical Chemistry, 1996, 100(38), 15581.
90. O.C. Dermer, G. E. Ham, *Ethyleneimine and other aziridines, chemistry and applications*1969New York: Academic Press.
91. M. Khan and W.T.S. Huck, *Hyperbranched Polyglycidol on Si/SiO2 Surfaces via Surface-Initiated Polymerization.* Macromolecules, 2003, 36(14), 5088.

92. Y. Kaneko, Y. Imai, K. Shirai, T. Yamauchi, and N. Tsubokawa, *Preparation and properties of hyperbranched poly(amidoamine) grafted onto a colloidal silica surface.* Colloids and Surfaces A: Physicochemical and Engineering Aspects, 2006, 289(1–3), 212.

93. Y. Yu, M.Z. Rong, and M.Q. Zhang, *Grafting of hyperbranched aromatic polyamide onto silica nanoparticles.* Polymer, 2010, 51(2), 492.

94. M.M. Mady, W.A. Mohammed, N.M. El-Guendy, and A.A. Elsayed, *Interaction of DNA and polyethylenimine: Fourier-transform infrared (FTIR) and differential scanning calorimetry (DSC) studies.* International Journal of Physical Sciences, 2011, 6(32), 7328.

95. Y. Kuwahara, D.Y. Kang, J.R. Copeland, N.A. Brunelli, S.A. Didas, P. Bollini, C. Sievers, T. Kamegawa, H. Yamashita, and C.W. Jones, *Dramatic enhancement of CO 2 uptake by poly(ethyleneimine) using zirconosilicate supports.* Journal of the American Chemical Society, 2012, 134(26), 10757.

CHAPTER IV

ADSORPTION PROPERTIES

In Chapter III, it was described the functionalization of silica with organic molecules, and general results pertaining to the functionalization were presented. This chapter focuses on the study of the adsorption properties of the prepared porous sorbents. At the beginning of the chapter both experimental and simulation characterization tools applied are described in detail. The following sections are focused on the adsorption properties of the prepared sorbents: water adsorption in alkylsilane hydrophobic samples and CO_2 adsorption in amino functionalized substrates. A deep characterization combining experimental and simulation tools was performed to this last group of materials in order to evaluate their adsorption properties at different temperatures and using pure CO_2 or a mixture of gases in cyclic adsorption/desorption measurements.

4.1 INTRODUCTION

Gas adsorption is an important characteristic of the synthesized materials. Adsorption is the enrichment of one or more components in an interfacial layer and the adsorption isotherm is the relation between the quantity adsorbed and the composition of the bulk phase (or the partial pressure in the gas phase) under equilibrium conditions at constant temperature. When a species diffusing in a porous solid is adsorbed to some extent, the ratio of adsorbed molecules to gas molecules in the pores may be very high if there is a large surface area associated with the pores and the material is very attractive to this molecule [1]. Depending upon the strength of the interaction, all adsorption processes can be divided into the two categories of chemical and physical adsorption [2]. Chemisorption is adsorption in which the forces involved are valence forces of the same kind as those operating in the formation of chemical compounds. The problem of distinguishing between chemisorption and physisorption is the same as that of distinguishing chemical and physical interaction in general. No absolutely sharp distinction can be made and intermediate cases exist, for example adsorption involving strong hydrogen bonds or weak charge transfer.

Physisorption is adsorption in which the forces involved are intermolecular forces (van der Waals forces) of the same kind as those responsible for the imperfection of real gases and the condensation of vapors, and which do not involve significant change in the electronic orbital patterns of the species involved [3].

Examples of both chemisorption and physisorption are found in this work. For instance, physisorption occurs in the water adsorption in functionalized alkylsilane samples where the water merely shows physical interaction with the silica surface. The adsorption of CO_2 in amino functionalized substrates is a good example of chemisorption, where carbamate species are formed as the result of the interaction between amino groups and CO_2 molecules. This makes amino functionalized substrates potential candidates to be applied as CO_2 adsorbents. To evaluate the performance of the supercritically prepared CO_2 adsorbents, detailed understanding of CO_2 and CO_2/N_2 separation is crucial [4]. Hence, the present chapter scrutinizes the adsorption capacity and the effectiveness of the prepared hybrid products, which are compared to literature data for similar materials prepared using

conventional methods. The influence of the materials surface area and pore characteristics in the long-term performance is also discussed, as well as the adsorption and desorption rates.

The underlying mechanism of the CO_2 adsorption processes occurring in highly complex amino-functionalized hybrid materials is not yet fully understood. This incomplete understanding limits the possibilities of designing ad-hoc optimal sorbents for specific applications, highlighting the interest of performing complementary experimental-simulation studies. In this Chapter, computational models for MCM-41 and silica gel functionalized with monoamine molecules were created and evaluated for CO_2 adsorption. The goal of the adsorption simulation studies was to provide new insights into the CO_2 adsorption mechanism in those porous materials. The simulated results are discussed and compared to data obtained experimentally.

4.2 ADSORPTION CHARACTERIZATION TOOLS

4.2.1 Karl Fischer method: water uptake

The hydrophobic behavior of porous silica samples functionalized with octyltriethoxysilane was studied through the adsorption and desorption of water molecules following well established methods [5-7]. In order to evaluate the hydrophobicity of functionalized samples, the amount of adsorbed water with time up to saturation was measured using the Karl Fischer (KF) tritation method. It is an analytical method that uses coulometric or volumetric tritation to determine amounts of water in a sample. Tritation is defined as a technique to determine the concentration of a substance in solution by adding to it a standard reagent of known concentration in measured amounts until a reaction of known proportion is completed. A color change or an electrical measurement indicates the end of the reaction. Then the unknown concentration can be calculated. With the KF tritation method both free and bound water can be determined, e.g. surface water on crystals or the water contained inside them. The method works over a wide concentration range from ppm to 100% and supplies reproducible results [8]. Reactants for KF coulometric and volumetric methods are composed by an alcohol and I_2. In the coulometric system the I_2 is generated in situ while in the volumetric it is introduced to the reaction.

In this work, a 633 Karl Fischer-Automat (Methrohm AG, Zofingen, Switzerland) equipped with a 715 Dosimat burette and a 703 Ti Stand stirrer was used to measure the adsorbed water content following the KF volumetric method. Reagents for H_2O determination comprised the Karl Fischer's Reagent compounds (RV, 1 mL reagent ~0.005 g H_2O) and methanol (RE, according to KF), both from Panreac.

For the water adsorption step, the silica samples were exposed to a relative humidity of either 60-65% (ambient conditions) or 90% (controlled atmosphere incubator at 20 ºC) during 7 or 30 days, respectively. Prior to this, samples were first dried at 120 ºC in an air oven for 20 h. At such temperature no significant hydrolysis of siloxane bonds was expected. Approximately 20 mg of each hydrated material was suspended in anhydrous methanol with the aid of magnetic stirring and titrated in a closed vessel using the Karl Fischer's reagent (Fig. 4.1). The water adsorption of each sample was measured three times and the arithmetic mean was given as the adsorbed value. Standard deviations lower than 5 % were found as error. A sharp indication of the end point was obtained by amperometric detection. For the porous materials under study, the kinetics of water desorption were monitored at diverse preselected times of 2, 4, 6, 8, 10, 15, 20 and 30 min. The water desorption to the methanol phase was considered to be completed after this period.

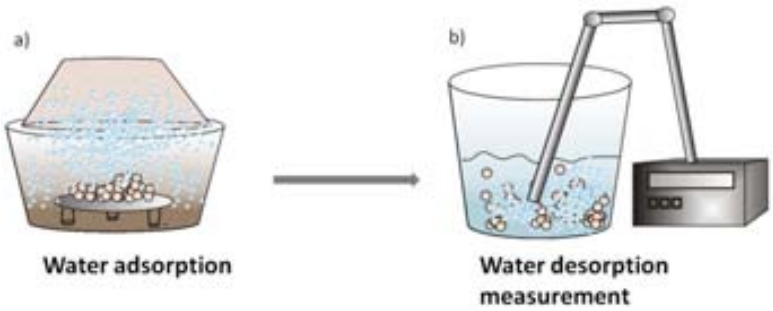

Figure 4.1 Study of the hydrophobicity of porous silica modified with octyltriethoxysilane: (a) water adsorption, followed by (b) water desorption measurements using the Karl-Fischer tritation method.

4.2.2 Gas adsorption analyzer: CO_2 adsorption isotherms

Sorption isotherms of CO_2 were obtained using a Micromeritics ASAP 2020 analyzer in the interval 0-100 kPa. Prior to measurements, samples were outgassed under reduced pressure at 120 ºC for 20 h, following the same procedure than for N_2 adsorption. A circulator bath containing heated oil was used to obtain the isotherms at different temperatures.

4.2.3 Microbalance: CO_2/N_2 adsorption/desorption cycles

The study of the CO_2 adsorption/desorption cyclic behavior was performed using a microelectronic recording balance (IMS HP HT Microbalance, based on a magnetically coupled Rubotherm GmbH microbalance) with a cell of 100 mL (Fig. 4.2). The measuring cell containing the sample holder is covered with a heating jacket that allows working at temperatures up to 450 ºC. The Rubotherm balance is a magnetic suspension balance able to detect weight changes of 10^{-5} g.

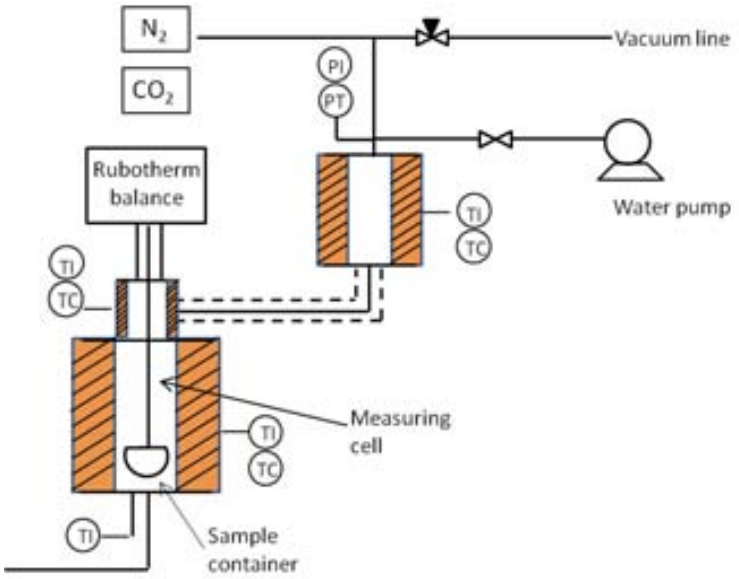

Figure 4 .2 Schematic diagram of the IMS HP HT Microbalance with a magnetically coupled Rubotherm GmbH.

Measurements were performed at atmospheric pressure and with a total flow of 200 scc min^{-1}. Figure 4.3 summarizes the main steps of the process: (a) the samples were first dried and decarbamated by passing N_2 at 105 ºC during 180 min. Then, they were cooled to the desired adsorption temperature (T_{ads} = 25 or 45 ºC) and (b) CO_2 adsorption was initiated by switching the N_2 purge gas to a CO_2/N_2 mixture (10/90 v%) maintained during 60 min. The desorption step (c) was carried out at 105 °C in a flow of N_2 for 90 min. A minimum of 10 cycles was applied to each sample.

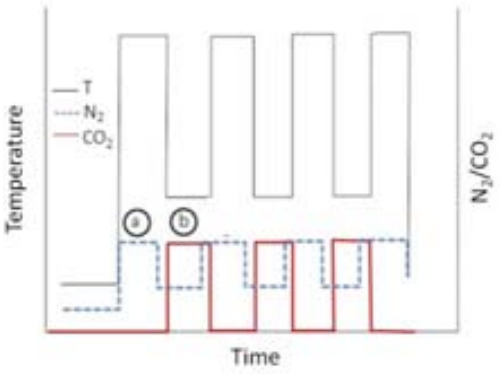

Figure 4.3 Schematic re presentation of the cyclic CO_2/N_2 adsorption/desorption steps: (a) CO_2 adsorption and (b) CO_2 desorption.

4.2.4 CO_2 adsorption molecular simulations

Adsorption simulations were carri ed out using the gr and can onical Monte Carlo (GCMC) method, equilibrating the chemical potential of the sorbent and a reservoir of gas by exchan ging and moving the adsorbed molecules. CO_2 adsorption isot herms were generated for the studied substrates at different degrees of functionalization and compared with the obtained experimental data. Similar potentials to N_2 adsorption simulations were used for the case of CO_2. However, for the spec ific cas e of CO_2 both physisorption and chemisorption were con sidered as feasible pr ocesses. CO_2 adsorption isoth erms were generated considering chemisorption at low CO_2 pressure and physisorption at all pressures [9]. Chemisorption is included in the molecular simulation calcu lations by add ing during functionalization a predefined number of carba mate and pr otonated amine chain s in addition to the non-reacted amine chains, instead of including only the aminosilane chains. The full details of th e method can be found elsewhere [10]. The inclusion of the

carbamates at zero coverage simulated the low pressure conditions at which the CO_2-amine reaction mainly occurs. Based on experimental data of supercritically functionalized systems, the amount of CO_2 chemisorbed in the system was fixed at the stoichiometric molar ratio of 0.5 moles of CO_2 per mole of functionalized amine. That is, half of the amine molecules were replaced by carbamates and the other half by protonated amines. However, for systems with a low degree of amine functionalization, the amine density was considered insufficient to allow the formation of carbamates and only non-reacted aminosilane chains were considered.

4.3 WATER UPTAKE IN HYDROPHOBIC POROUS MATERIALS

The functionalization of porous silica with octyltriethoxysilane carried out in this work is expected to increase the hydrophobicity of the samples. Table 4.1 shows the grafting alkylsilane values for each studied sample together with the adsorbed water values after 1 month and one week of hydration at 20 ºC at 90 % and 60-65 % of relative humidity, respectively.

Table 4.1 Adsorbed water (A_w) expressed as grams of water per gram of dry matrix [$g_w\, g_m^{-1}$], after one month (A_w) of hydration at 90 % relative humidity and after one week (A_{w_1}) of hydration at 60-65 % relative humidity.

Sample	ρ_{graft} [molec nm^{-2}]	A_w [$g_w\, g_m^{-1}$]	A_{w_1} [$g_w\, g_m^{-1}$]
b-CC	-	1.33	0.06
1-CC	0.85	0.33	-
2-CC	0.82	0.3	-
5-CC	1.02	-	0.04
3-CC	0.75	0.38	-
4-CC	0.7	0.33	-
b-SB	-	0.28	0.17
1-SB	1.02	0.17	-
2-SB	0.95	0.16	-
5-SB	1.16	-	0.07
3-SB	0.94	0.19	-
4-SB	0.94	0.2	-
b-SG_{40}	-	0.37	0.11
1-SG_{40}	0.43	0.26	-
2-SG_{40}	0.44	0.23	0.06
3-SG_{40}	0.57	0.21	-
4- SG_{40}	0.50	0.20	-
b-ZY	-	0.33	0.23
2-ZY	0.96	0.21	-
5-ZY	1.02	0.18	0.18
3-ZY	1.13	0.20	-
4-ZY	1.05	0.21	-

Figure 4.4 shows a comparison of the water uptake of the meso- and microporous samples hydrated under ambient conditions during 1 week. The percentage of water uptake for mesoporous samples was reduced to *ca.* 50 % after silanization.

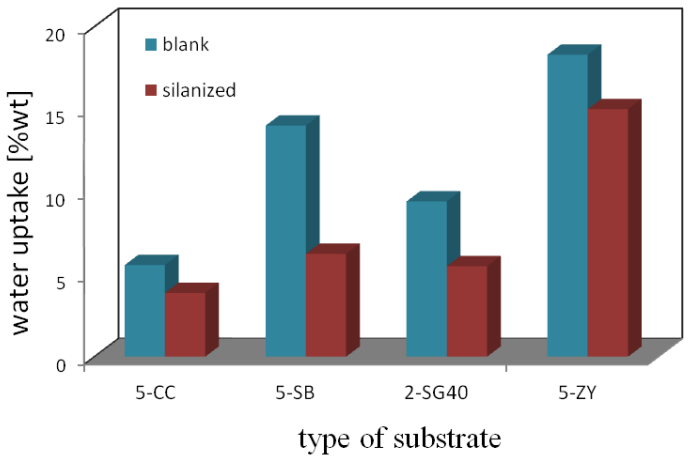

Figure 4.4 Water uptake, expressed as the weight of adsorbed water per total weight of sample, after one week of hydration under ambient conditions (20-21 ºC and 60-65 % relative humidity).

In the SB samples, the modification of the water adsorption capacity was evidenced qualitatively from the color change of the moisture indicator from blue (dry) to pink (moisturized). As shown in Fig. 4.5, after 1 h of moisture adsorption under ambient conditions, the pink color was more evident for the blank than for the treated samples and the persistence of the blue color increased with the processing time from 90 to 420 min.

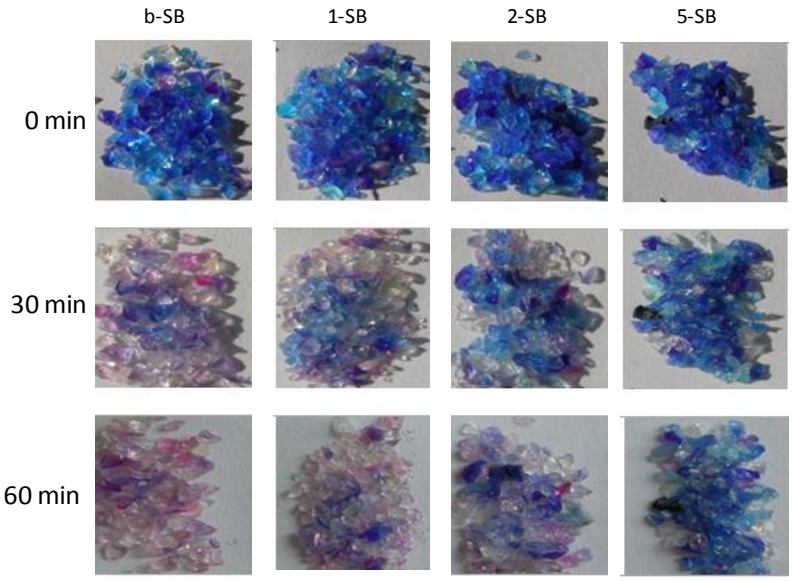

Figure 4.5 Optical pictures of the modification of the color (from blue to pink) of raw and silanized silica gel blue samples exposed to ambient conditions (64% relative humidity at 20-21 ºC). Samples were first dried in an air oven at 120 ºC during 20h.

After silanization, the water adsorption drop was less important for microporous zeolite samples than for mesoporous matrices (Fig. 4.4). For amorphous mesoporous silica, residual uncondensed hydroxyl groups from the original polymeric silicic acid remained on the surface of each primary silica particles, conferring upon silica gel its polar properties. Hence, the replacement of some Si–OH groups by hydrolytically stable C_8Si- hydrophobic groups (chemisorption) prevented, in part, water penetration. Conversely, the zeolite is a crystalline hydrated aluminosilicate whose framework structure encloses cavities occupied by water molecules linked to the surface by electrostatic forces. Silane physisorption in such a pore network did not prevent effectively the adsorption of polar water. The water desorption kinetic curves for several examples of the different blank and treated substrates left during 1 month (Table 4.1) in a closed recipient under controlled moisture (90 %) are shown in Fig. 4.6. The water uptake was reduced by a 10-fold factor for CC silanized materials and by a factor of *ca.* 1.5–2 for the rest of the meso- and microporous substrates. For the studied porous matrices, with extremely high surface areas, the amount of silane incorporated after supercritical treatment was not enough to completely coat the internal surface with a monolayer, as indicated by TGA. Hence, residual hydrophilic silanols were

still present on modified surfaces together with adsorbed and grafted hydrophobic silane molecules.

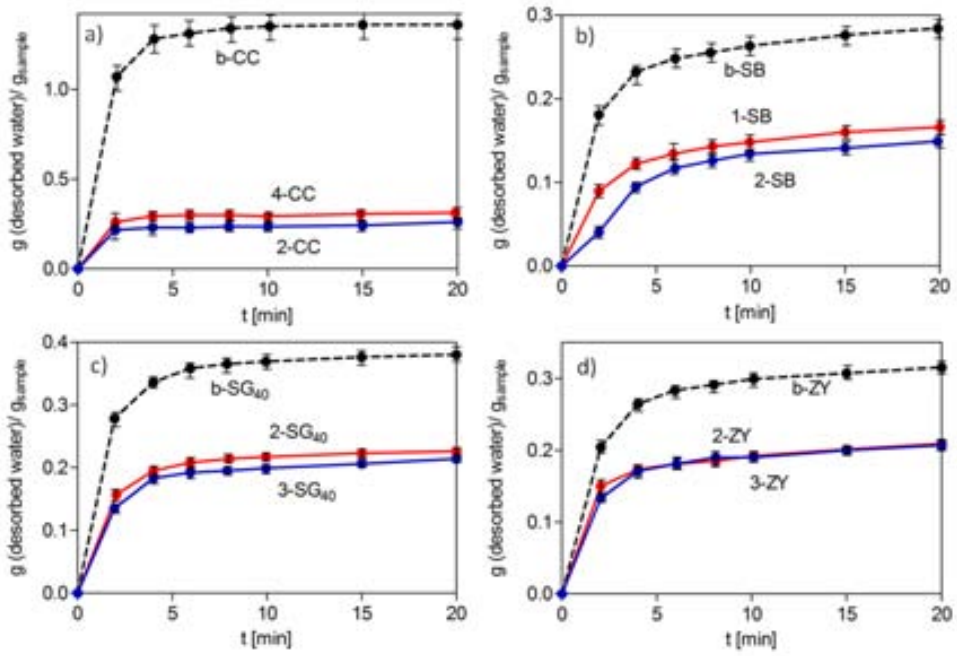

Figure 4.6 Curves of desorbed water, obtained using the Karl Fischer analytical method, for meso- and microporous bare and silanized selected samples after hydration during one month in a closed humid environment: (a) CC, (b) SB, (c) SG_{40} and (d) ZY. Symbols represent experimental data and the lines are a guide to the eyes.

4.4 CO_2 ADSORPTION ON AMINOSILANE FUNCTIONALIZED SILICA

The capacity of supercritically prepared aminosilica hybrid products for CO_2 adsorption and its separation from mixtures with other gases is here analyzed. The CO_2 adsorption capacity under dry conditions of mesoporous silica gel and MCM-41 functionalized with the monoaminosilane MAP was first evaluated by recording CO_2 adsorption isotherms and next by performing microbalance cyclic adsorption/desorption experiments at 25 and 45 ºC. CO_2 adsorption and desorption rates were also studied as a function of the amine loading. CO_2 adsorption results were compared to similar data available in the literature, showing improved performance for the compressed CO_2 prepared products related to the CO_2 adsorption efficiency and cyclic regenerability.

4.3.1 CO_2 adsorption isotherms

Data on the amine loading and pore structure of the synthesized materials are required to study in detail their CO_2 adsorption capacity. These parameters, determined from thermogravimetric analysis and low-temperature N_2 adsorption/desorption experiments are summarized in Table 3.4 Chapter III, section 3.3.2.2. CO_2 adsorption isotherms for the prepared materials were recorded up to pressures of 100 kPa at 25 ºC (Fig. 4.7). Pure silica surfaces do not interact very strongly with carbon dioxide because the residual hydroxyl groups are not able to induce strong enough interactions. For this material, the adsorption could be represented by a linear equation characteristic of physisorption. Adsorption values for raw silica gel, MCM-41 and CC materials were in the order of 0.05 and 0.11 mmol g^{-1} at 10 kPa.

CO_2 adsorption increased to values of 0.3-0.4 for SG_{40} (Fig. 4.7a) and CC (Fig. 4.7b) and of 0.7 for MCM41 (Fig. 4.7c) by increasing the adsorption pressure to 100 kPa. For SG_{40} samples, the MAP uptake was relatively low, in the order of 0.5 molec nm^{-2}. This density was too small to allow for carbamate formation between two different aminosilane molecules. Hence, CO_2 sorption, even at low pressure, was only due to physisorption, as shown by the shape of the isotherm (Fig. 4.7a). Adsorption values were lower than those obtained for the raw material, since some of the CO_2 adsorption sites were already occupied by aminosilane molecules and less empty volume was available for adsorption. The effect of chemisorption in the shape of the isotherms was evident for samples with medium and high loading degrees (> 1 molec nm^{-2}). These samples had a high initial CO_2 uptake at very low pressures (< 5 kPa) that was the contribution of the chemical reaction. For CC materials with a high amine uptake, the CO_2 sorption values increased. In Fig. 4.7b, the behavior of sample 6-MAP@CC, with an amine loading of 3.14 mmol g^{-1}, is compared to the profile recorded for raw CC. At very low pressures (10 kPa) the amount of adsorbed CO_2 for the hybrid material was of 0.92 mmol g^{-1}, which was significantly higher than the value obtained for raw CC. This behavior can be explained by the great affinity of the acid CO_2 for the basic amine sites, i.e., by chemisorption [11, 12]. Increasing the pressure up to 100 kPa the sorption in 6-MAP@CC increased to a value of 1.2 mmol g^{-1}, but this increase was mainly due to physisorption.

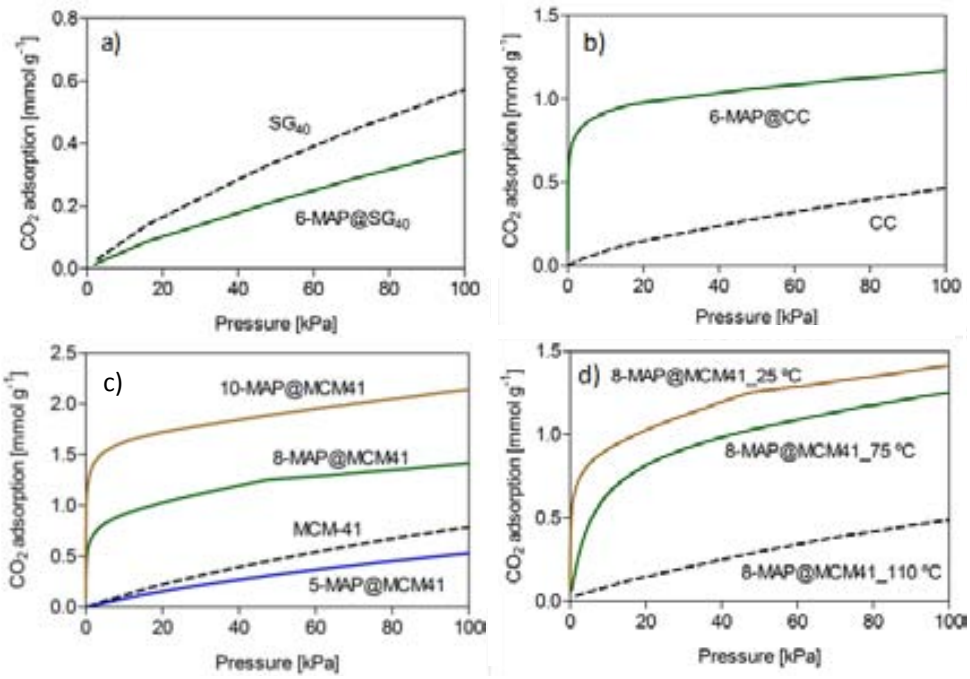

Figure 4.7 CO_2 isotherms of amine grafted porous substrates at 25 ºC for: (a) $SG_{40,}$ (b) CC and (c) MCM-41; and (d) sample 8-MAP@MCM41 at 25, 75 and 110 ºC.

In Fig. 4.7c, functionalized MCM-41 samples are compared to the bare substrate. Sample 5-MAP@MCM41 with a low functionalization degree (< 1 molec nm^{-2}) exhibit a lower adsorption than the raw MCM-41. Considering that the supercritical functionalization method produces a uniform distribution of the amine chains on the surface, at low amine surface densities, carbamate formation between two neighboring aminosilane molecules is hindered by substantial distance between them. For samples 8- and 10-MAP@MCM41, with loadings of 1.56 and 5.59 mmol g^{-1}, respectively, the CO_2 sorption increased with the amount of amine loaded. At 10 kPa, the CO_2 adsorption values were of 0.82 and 1.62 mmol g^{-1} for 8- and 10-MAP@MCM41 samples, respectively. By further increasing the CO_2 pressure up to 100 kPa, the empty pore volume was filled by physisorption and the uptake values were increased to 1.43 and 2.13 mmol g^{-1} for 8- and 10-MAP@MCM41 samples, respectively.

The presence of open porosity in the sorbent after amine functionalization has been described as an important characteristic that makes the material particularly attractive for adsorption at ambient temperature [13]. From N_2 adsorption/desorption isotherms, it was noted a significant reduction of pore volume for the studied substrates, to values of 40 % of the original values in samples 6-MAP@CC and 8-MAP@MCM41, and to a value of only 0.01 $cm^3 g^{-1}$ for sample 10-MAP@MCM41 (Table 3.4, Chapter IV, section 3.3.2.2). The loss of porosity seems not to totally hinder CO_2 accessibility, since a high performance was observed even at a very low pressure. This apparent contradiction with the N_2 adsorption results is explained by the higher temperature used during the CO_2 adsorption measurements (25 ºC) compared to the - 196 ºC employed for the N_2 adsorption tests. At the low N_2 temperature, the grafted amine chains are expected to behave as rigid materials, thus, limiting gas diffusion. Carbamate formation involves two nitrogen atoms from amine groups close enough to allow the reaction. Hence, under dry conditions, the maximum efficiency of a monoamine adsorbent is 0.5 mol of CO_2 per mol of N (Fig. 3.14, Chapter IV, section 4.3.2). At the very low pressures of 10 kPa, where physisorption was considered insignificant, efficiency values, calculated as mmol g^{-1} of sorbed CO_2 / $mmolg^{-1}$ of loaded amine, were estimated as 0.5 and 0.3 for samples 8-MAP@MCM41 (P_v=0.40 cm^3g^{-1}) and 10-MAP@MCM41 (P_v=0.01 cm^3g^{-1}), respectively. Therefore, diffusion restrictions due to high loading were noticed in sample 10-MAP@MCM41. At similar loadings, other authors have reported the influence of the aminosilane grafting method on the effective CO_2 uptake [14, 15]. In general, the use of anhydrous solvents with water traces and low silane concentration is desirable for the preparation of smooth densely amino-derived silane layers that maintain enough open porosity for CO_2 chemisorption. The use of the anhydrous supercritical method seems to produce ordered and densely anchored aminosilane layers, which affords amine pairs and results in a larger fraction of amine being available for CO_2 adsorption, even at low apparent porosity.

Fig. 4.7d shows the CO_2 adsorption isotherms of 8-MAP@MCM41 measured at different temperatures (25, 75 and 110 ºC). The best performance occurred at room temperature (25 ºC), with the maximum theoretical adsorption efficiency of 0.5 reached. When the temperature was elevated to 75 ºC, the adsorption efficiency dropped to 0.38. By further increasing the temperature to 110 ºC, the chemisorption process at low pressure

was not observed any more, and the adsorption profile was similar in shape to that of the raw material (Fig. 4.7c). Similar results have been reported for aminosilanes grafted on MCM-41 and other porous supports [16-18]. The formation of carbamate is favored at low temperature due to the exothermic character of the reaction between the amine and the CO_2, whereas carbamate dissociation prevails at elevated temperatures [19]. Hence, the CO_2 adsorption capacity decreased with temperature. Nevertheless, the influence of temperature in the CO_2 sorption behavior is complex and in some of the literature published data, the CO_2 sorption capacity increases as the temperature is increased, particularly for highly loaded polymeric samples. For instance, the strong diffusion limitations to CO_2 adsorption generated at room temperature by polymer PEI-impregnated in MCM-41 has been widely reported [20, 21]. For those materials, as the temperature is increased, enhanced CO_2 diffusivity and accessibility of vacant adsorption sites result in an increase of CO_2 sorption capacity.

The behavior of the crystalline zeolite was completely different to that of amorphous porous silicas and it is discussed separately. Zeolites have been widely used in separation applications mainly because of their unique ability of molecular sieving. CO_2 molecules are known to be physisorbed to its surface through electrostatic interactions. An example of a commercialized adsorbent for CO_2 removal from gas streams is the zeolite 13X [4]. In a pure CO_2 atmosphere and at a relatively low temperature, this zeolite has an adsorption capacity of 1.5-2 mmol g^{-1} at low pressure, which increases to 5 mmol g^{-1} at 100 kPa. However, the substantial decrease in CO_2 uptake at elevated temperatures or under humid conditions limits the efficacy of zeolites. Moreover, they are inefficient in the separation of CO_2 from other light gasses, since N_2 and other nonpolar gases are also easily adsorbed in the micropores. In this work, we have studied the behavior of a zeolite type Y, with a similar structure than zeolite X, but a slightly higher silica-to-alumina ratio. In a pure CO_2 atmosphere, raw ZY physisorbed 2.9 mmolg^{-1} at 100 kPa (Fig. 4.8). However, this amount was reduced by impregnating the pores with the aminosilane to a value of 2.4 mmolg^{-1} at 100 kPa. The low diameter of the ZY channels made impossible for the amine molecules to land together in a vertical position suitable for carbamate formation. Therefore, the presence of amines did not assist CO_2 sorption, at least under dry conditions in which two molecules of amine were needed to graft one CO_2 molecule. On the contrary, the pore

filling produced by the amine molecules reduced the available pore space for CO_2 physisorption [22].

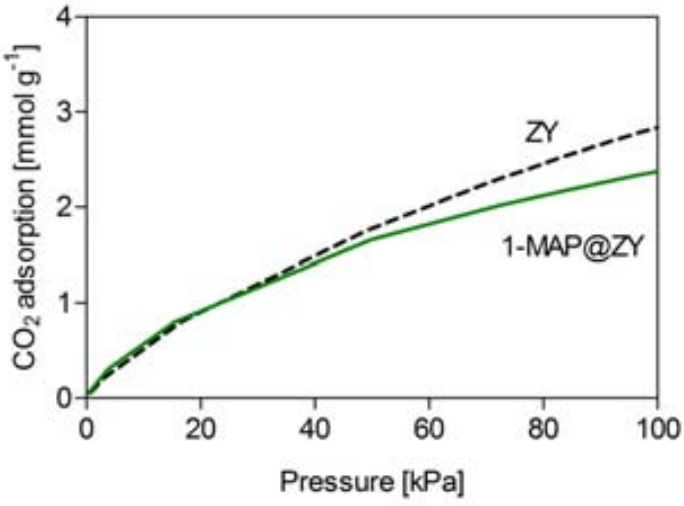

Figure 4.8 CO_2 isotherms of raw and amine impregnated microporous zeolite substrate at 25 ºC.

4.3.2 Molecular simulation

Some of the supercritically functionalized MCM-41 and SG_{40} samples were selected for comparison with the reproduced modeled materials. Table 3.5 from Chapter III, section 3.3.2.7, show the textural properties of the raw and aminosilanized materials or both experimental and model samples (labeled with the "s" subindex).

4.3.2.1 MCM-41

The addition of the amino functional group is expected to modify surface properties by increasing the gas-sorbent interaction at low pressures. Although the N_2 adsorption capacities of the MCM-41 samples decreased with increasing functionalization (Fig. 3.20, chapter III), in an optimal functionalized material for CO_2 capture, the inherent high physisorption capacity of porous silica materials at high pressures should be preserved and merged with chemisorption trend of the amine groups at low pressures [23]. However, the behavior of both experimental and model samples with a low functionalization degree (1

mmol g^{-1}) was similar to that of the raw materials (Fig. 4.9a). The adsorption values were even slightly lower than those obtained for the raw materials, since less void space was available for adsorption after functionalization. The simulations accurately predict for 5-AP@MCM41$_S$ sample the decrease of the adsorption capabilities with respect to the raw material, supporting the hypothesis that amines do not significantly react with CO_2 on the 5-MAP@MCM41 sample. Differences between CO_2 adsorption values for 5-AP@MCM41$_S$ and 5-MAP@MCM41 samples can be attributed to experimental errors in the adsorption measurements for the experimental product. These materials, functionalized with 1 mmol g^{-1} of amine, have a low density of amine groups grafted on the surface, which was considered insufficient for the CO_2-amine reaction. At low grafting densities the molecules supercritically added distribute in a homogeneous way, which impedes the proximity of pairs of amines necessary for carbamate formation under dry conditions. Hence, CO_2 adsorption was only due to physisorption, as shown by the shape of the isotherms in Fig. 4.9a.

The chemisorption effect was evident for the samples with a relatively high degree of amine functionalization, i.e. 2 mmol g^{-1} for 11-MAP@MCM41 and 11-AP@MCM41$_S$. In those cases, the CO_2 adsorption equilibrium values increased considerably due to chemisorption at low pressures. The CO_2 adsorption isotherms of experimental 11-MAP@MCM41 and model 11-AP@MCM41$_S$ samples were very similar (Fig. 4.9a), indicating that the assumption employed in the simulations, related to the chemical reaction occurring at low pressure, is correct. For the models 5-AP@MCM41$_S$ and 11-AP@MCM41$_S$, the average shortest distance between N atoms of the grafted amino groups was calculated during GCMC simulations. This distance is used as an indicative of the average separation between amino groups inside the porous support. The results indicate that this distance was of 0.57 nm (standard deviation of 0.37 nm) for 5-AP@MCM41$_S$ and 0.26 nm (standard deviation of 0.13 nm) for 11-AP@MCM41$_S$. Hence, the size of the CO_2 molecules (0.23 nm), is comparable to the average shortest distance between N atoms in 11-AP@MCM41$_S$. Therefore, it is consequent with the behavior of the latter material, which, unlike 5-AP@MCM41$_S$ exhibits a significant CO_2 chemisorption.

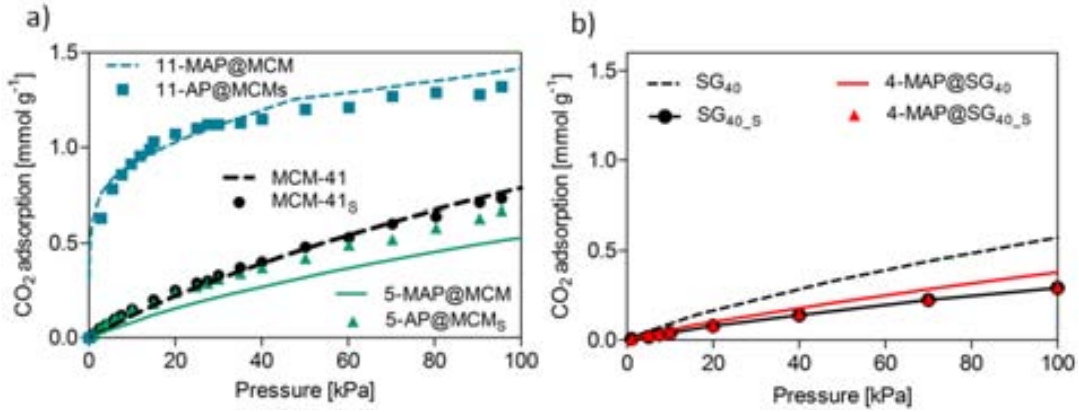

Figure 4.9 CO_2 adsorption isotherms for synthesized and simulated: (a) MCM-41 and (b) SG_{40} samples.

4.3.2.2 SG_{40}

The CO_2 adsorption of the experimental and simulated silica gel materials (marked with the sub index s) is depicted in Fig. 4.9b. It is seen that the functionalization of the SG_{40} substrate slightly decreases the adsorption capacity of the experimental 4-MAP@SG_{40} material, whereas the simulated SG_{40_S} and 4-AP@SG_{40_S} products show an almost identical behavior between the support and the functionalized material. All the measured and calculated CO_2 adsorption isotherms indicated physisorption with very small or almost null CO_2-amine or CO_2-silica interactions. Due to the low CO_2 loading values obtained for the experimental silica gel materials, either pristine or functionalized, the adsorption differences found between SG_{40} and 4-MAP@SG_{40} could be ascribed to measurements inaccuracy.

4.3.3 Cyclic performance and separation from N_2

For the supercritically prepared samples, the ability of selectively adsorbing CO_2 from a mixture with N_2 was examined at 25 and 45 ºC in an integrated microbalance system (Table 4.2). Adsorption values were taken from the first adsorption/desorption cycle.

Table 4.2 CO_2 adsorption values obtained from a cyclic CO_2/N_2 adsorption/desoprtion process performed at 25 and 45 ºC.

Sample	T_{ads} [ºC]	CO_2 ads [mmol g^{-1}]	molar ratio CO_2/amine
MCM-41	45	0.07	-
1-MAP@MCM41	45	0.05	0.13
5-MAP@MCM41	45	0.05	<0.1
11-MAP@MCM41	25	0.9	0.50
	45	0.6	0.33
12-MAP@MCM41	25	1.0	0.41
13-MAP@MCM41	45	1.1	0.32
10-MAP@MCM41	25	1.0	0.25
	45	1.3	0.33
CC	45	0.04	-
1-MAP@CC	45	0.04	<0.1
4-MAP@CC	45	0.72	0.36
6-MAP@CC	45	0.87	0.33

4.3.3.1 Influence of amine loading

At 25 ºC, the CO_2 adsorption values for MAP@MCM-41 products was almost independent of the specific amine loading or amine surface density in the studied ranges (solid lines in Fig. 4.10). Conversely, at 45 ºC the CO_2 adsorption capacity was a function of the amine loading degree or the surface density for both kinds of studied supports (dashed lines in Fig. 4.10). The trend in the increase of the CO_2 adsorption capacity with the specific amine loading was similar for MCM-41 and CC supports (Fig. 4.10a). Thus, medium loaded samples had relatively high CO_2 adsorption values in the order of 0.6-0.7 mmol g^{-1}, while CO_2 adsorption values as high as 1.3 and 0.9 mmol g^{-1} were obtained for the highly loaded 10-MAP@MCM41 and 6-MAP@CC samples, respectively. By representing CO_2 adsorption data as a function of the amine surface density (Fig. 4.10b), it can be observed that the slope of the trend line for CC/MAP adsorbents turns to be significantly smaller than the one draw for the MAP@MCM41 products. Thus, at a similar amine surface density, adsorbents prepared using MCM-41 were more effective for CO_2 capture than the ones obtained from CC substrate.

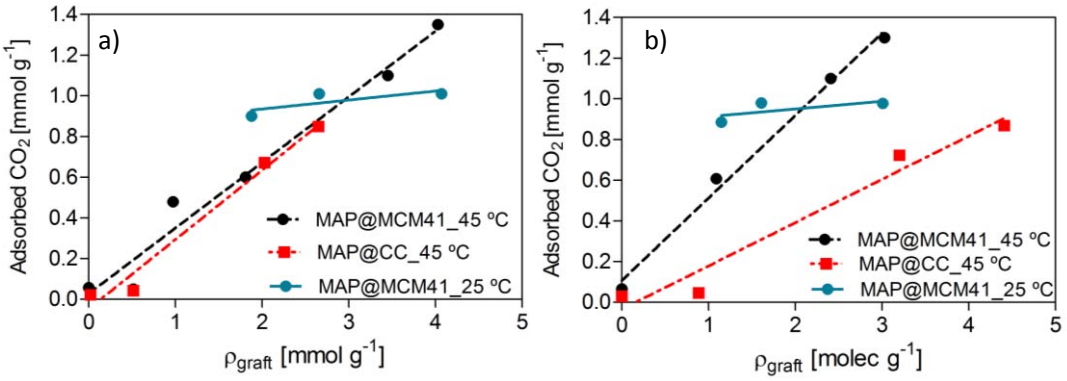

Figure 4.10 Representation of the CO_2 adsorption capacity of MAP modified porous supports as a function of: (a) amine concentration, and (b) amine surface density.

4.3.3.2 Influence of the temperature

The influence of temperature was studied in the medium and highly loaded MAP@MCM41 samples (Table 4.2). The effect of increasing the temperature in the CO_2 adsorption behavior is two-fold. First, carbamate dissociation, associated with CO_2 desorption, is favored due to the exothermic character of the amine-CO_2 reaction. Second, CO_2 diffusivity and accessibility to amine adsorption sites is enhanced, together with amine chains mobility that reduces pore blocking and, thus, CO_2 adsorption is favored. For materials maintaining a significant open pore volume after functionalization (11-MAP@MCM41 sample in Table 3.4 Chapter III, section 3.3.2.2), the adsorption capacity decreased from 0.9 to 0.6 mmol g^{-1} by increasing the temperature from 25 to 45 ºC, indicating that the effect of the shift to the free amine in the carbamate reaction prevailed over the increase in CO_2 diffusivity. On the contrary, the increase in the CO_2 diffusivity seemed to be the predominant effect occurring in the highly loaded sample 10-MAP@MCM41, in which the CO_2 adsorption values increased from 1.0 to 1.3 mmol g^{-1} at 25 and 45 ºC, respectively.

4.3.3.3 Comparison to literature data

Data on CO_2 adsorption/desorption up to 10 cycles were measured and used to determine the stability of the supercritically prepared hybrid products. Fig. 4.11 shows the

measured values for pristine substrates and low, medium and high amine loaded hybrid MAP@MCM41 and MAP@CC products. Obtained records revealed that the performance of the hybrid products was fairly stable and no significant loss in efficiency was observed for the studied supports.

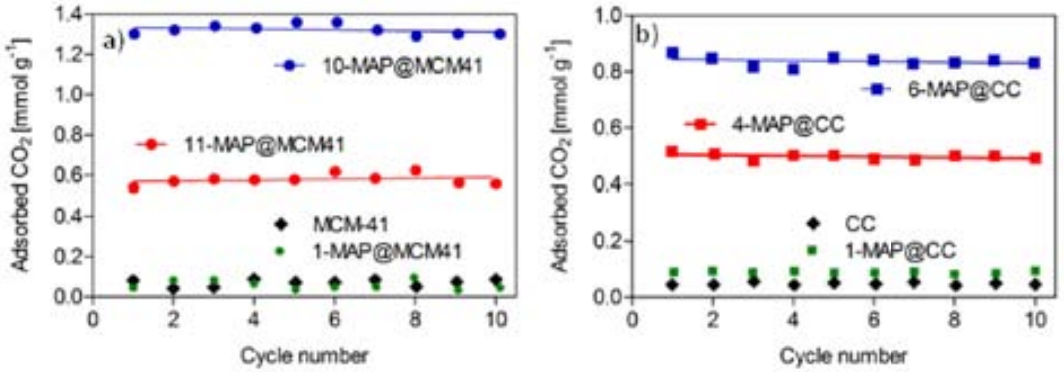

Figure 4.11 CO_2 adsorption at 45 ºC in cycles 1-10 for: (a) raw MCM-41, low 1-MAP@MCM41, medium 11-MAP@MCM41 and high 6 -MAP@MCM41 amine loadings, and (b) raw CC, low 1-MAP@CC, medium 4-MAP@CC and high 6-MAP@CC amine loadings

The CO_2 adsorption capacity of supercritically prepared materials was compared with published adsorption data for grafted monoaminosilanes synthesized using the organic-liquid approach (Table 4.3).

Table 4.3 CO_2 adsorption data compiled from the literature for products involving monoamine loaded into diverse porous supports: loading degree, reported textural properties of pristine supports and adsorption values (best reported result) together with adsorption efficiency.

Substrate	ρ_{graft}[1] [mmol g_p^{-1}]	ρ_{molec}[1] [molec nm^{-2}]	P_d[3] [nm]	P_v[3] [$cm^3 g^{-1}$]	CO_2[4]@T_{ads} [mmol g^{-1}]@[ºC]	Ratio CO_2/amine	Ref.
Hexagonal silica	1.7	1.0	3	1.0	0.9@20	0.53	[24]
Silica xerogel	1.7	1.3	3	0.7	0.5@25	0.30	[13]
Mesocaged Silica	1.6 1.6	1.0 1.0	1-4	0.5	0.2@25 0.8@70	0.13 0.50	[12]
Silica gel 40	1.1	1.2	4	0.7	0.7@20	0.64	[11]
Silica gel Davisil	3.6	4.0	6	0.9	0.92@23	0.25	[25]
Silica gel	1.2 1.2	2.1 2.1	12	1.4	0.3[5]@25 0.2[5]@50	0.25 0.17	[26]
Aerogel	3.7	2.2	20	3.5	0.5@22	0.14	[27]
Doble-wall silica nanotubes	2.2[2] 2.2[2]	3.8[2] 3.8[2]	3-40	1.1	1.0@25 0.8@50	0.45 0.36	[26]
MCM-48	2.5 2.5	1.2 1.2	2.6	1.1	0.7[5]@25 0.6[5]@45	0.28 0.24	[28]
MCM-48	2.3	1.0	2.5	1.1	1.1@25	0.55	[29]
SBA-12	2.1 2.2[2]	0.9 1.0[2]	3.5	0.8	1.0@25 1.0@25	0.48 0.45	[30]
MCM-41	2.5	1.4	4	0.9	0.6@30	0.24	[18]
MCM-41	2.0	1.4	4	0.6	0.4@30	0.20	[18]
SBA-15	1.9	1.5	6	0.7	0.5@30	0.26	[26]
SBA-15	2.6	1.7	6	1.1	0.5@60	0.19	[31]
SBA-15	3.4 3.1[2]	2.3 2.1[2]	6	1.1	1.0[5]@25 0.8[5]@25	0.29 0.26	[32]
SBA-15	2.6	2.7	8.5	1.0	0.9@25	0.32	[33]
Pore expanded SBA-15	1.6	2.6	13	1.7	0.2@30	0.13	[33]
Pore expanded MCM-41	4.3	2.3	10	2.3	2.1@25	0.49	[34]

[1]AP aminosilane, [2]MAP aminosilane, [3]pristine supports, [4]CO_2 atmospheric adsorption from a mixture of 5-10 v% of CO_2 in N_2, [5]CO_2 atmospheric adsorption at 5-10 kPa.

Data for 3-aminopropylsilane (AP) and MAP were compiled together, since they lead to similar adsorption results [31]. Most of the literature reported aminosilane loading values are within the range 1-4 mmol g^{-1}, corresponding to CO_2 adsorption values between *ca.* 0.4 and 1 mmol g^{-1}. In Fig. 4.12 the CO_2 adsorption value for each material in Table 4.3 is represented as a function of the amine loading (Fig. 4.12a) or the surface amine density (Fig. 4.12b), as well as the CO_2 adsorption results (Table 4.2) of the best performing products synthesized in this work (samples 6-MAP@CC and 10-MAP@MCM41 at 25 and 45 ºC). The theoretical adsorption efficiency under dry conditions is limited to 0.5 mol_{CO2}/mol_{amine}[35, 36], which is represented by a solid line in Fig. 4.12a. This value was calculated for each sample presented in Tables 4.2 and 4.3 (molar ratio CO_2/amine) and represented as a dashed trend line in Fig. 4.12a. Most of the published adsorption efficiency values are lower than 0.5, as also occurs with the values estimated in this work. Moreover, Fig. 4.12a points out that the higher the amine loading the higher the separation between the measured and the theoretical efficiency values. Reasons are related to diffusion limitations and intra molecular bonding occurring at high amine concentrations, both decreasing the adsorption efficiency. Analyzing the CO_2 adsorption data *vs.* the amine surface density (Fig. 4.12b), it can be observed that the CO_2 adsorption for products with surface densities in the range 1-1.3 molec nm^{-2} was only significant for substrates with very small pore size (*ca.* 2.5-3 nm). For these materials, the interaction of amine pairs for carbamate formation would be favored by the narrow pore size, even at a low surface density. For materials with pore diameters larger than 3 nm, a high amine surface density was required to have an appreciable CO_2 adsorption [33].

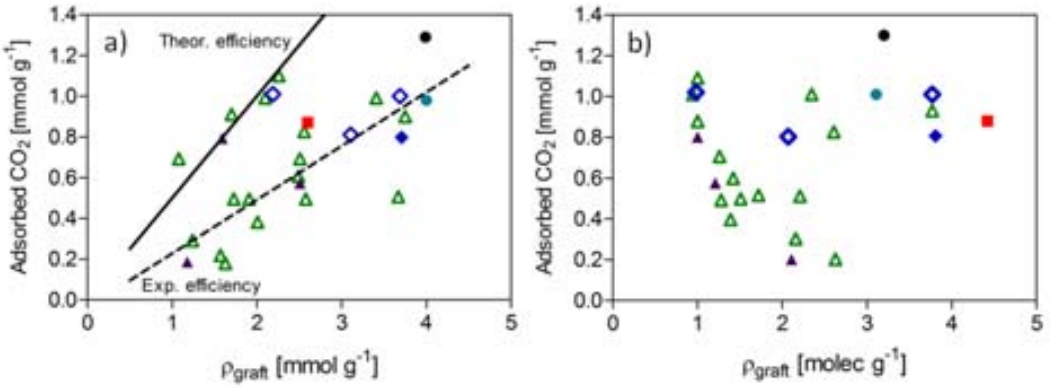

Figure 4.12 Summary of this work (Table 4.2) and literature data (Table 4.3) of the best CO_2 adsorption values obtained as a function of: (a) amine specific concentration, and (b) amine surface density. The open and filled symbols represent data obtained at low (25-30 ºC) and high (≥ 45 ºC) temperature, respectively. Green triangles represent AP products while blue diamonds correspond to MAP samples. Samples prepared in this work are represented following the same color code than in Fig. 4.10

.

4.3.3.4 CO_2 adsorption and desorption rates

A fast adsorption rate is one of the most important characteristics expected in any efficient CO_2 solid adsorbent. Most of the studies on CO_2 adsorption kinetics are based on the analysis of CO_2 adsorption isotherms measured under equilibrium conditions by fitting the data to semi-empirical models [37]. However, CO_2 sorption and separation carried out in realistic conditions is a dynamic process involving both adsorption, with simultaneous chemisorption and physisorption, and desorption processes. Moreover, it is usually performed in the presence of other light gases. In this work, an estimation of the CO_2 adsorption and desorption rates for the supercritically synthesized products was performed by examining the first recorded curve in the microbalance adsorption/desorption cycles. First, the data was smoothed by fitting it to empirical correlations, thus, eliminating fluctuations due to measurement instabilities. Figure 4.13 shows as an example the recorded curves and the fitted lines for 5 cycles in samples 10-MAP@MCM41 and 6-MAP@CC. The cyclic profiles can be divided in three different steps: fast adsorption occurring in empty adsorbents, slow adsorption occurring close to adsorption equilibrium and desorption. The slopes of the three different steps were calculated for the samples of interest and denoted as s_1, s_2 and s_3.

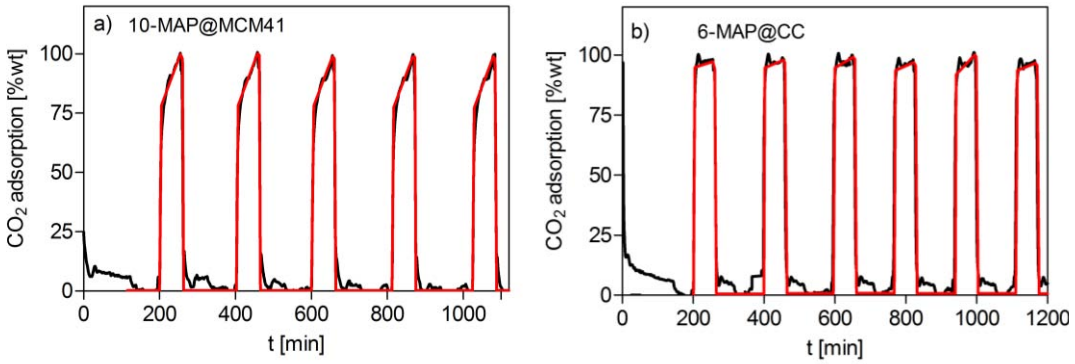

Figure 4.13 Cyclic behavior of representative synthesized materials: (a) MAP@MCM41 and (b) MAP@CC samples. The black lines corresponds to the original recorded curves, while the red lines are the fitted profiles. Numbers indicate the CO_2 fast (1) and slow (2) adsorption and desorption (3) steps.

The influence of the aminosilane loading in the adsorption and desorption rates is shown in Fig. 4.14a,b for samples MCM-41/MAP and CC/MAP, respectively. The adsorption rate in the empty hybrid adsorbents increased with the amine loading for both type of porous substrates. Moreover, it can be observed that, under similar experimental conditions, adsorption rates in the fast adsorption region for MAP@CC hybrid products were slightly higher than those found for MAP@MCM41 compounds. The reason of this behavior is linked with the larger pore diameter of CC silica gel with respect to MCM-41 support, which would facilitate gas diffusion. Contrarily, the slow adsorption rate in the second step was one order of magnitude higher in MAP@MCM41 samples than in MAP@CC composites. Indeed, adsorption in this region was only significant for MAP@MCM41 hybrid products. Analyzing the desorption rate, faster kinetics were observed for the highly loaded samples, regardless of the used support. Fig. 4.14c shows the influence of the temperature in the s_1, s_2 and s_3 values for the 10-MAP@MCM41 sample. Remarkably, the adsorption rate in step 1 was significantly faster at 45 than at 25 ºC, with s_1 values of 0.22 and 0.05 mmol g^{-1} min^{-1}, respectively. For this sample, with a low open porosity (0.01 cm^3 g^{-1}), an increase in the temperature favored CO_2 diffusion, enhancing the adsorption rate. The slow adsorption and desorption profiles had similar slopes at both studied temperatures.

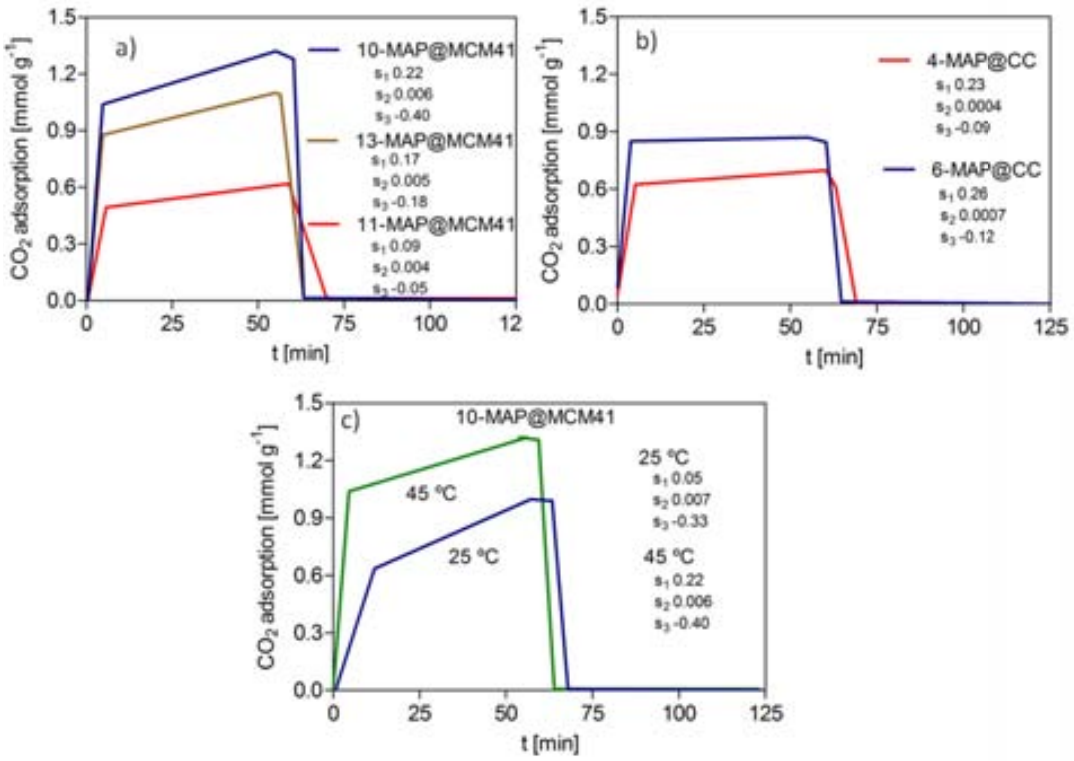

Figure 4 .14 Comparison of the adsorption/desorption pro files of sam ples prepared or m easured under different experimental conditions: (a) MAP@MCM41 and (b) MAP@CC products with different loadings at 45 ºC, and (c) 10-MAP@MCM41 sample at two different temperatures. Slopes s_1, s_2 and s_3 are given in mmol g^{-1} min^{-1}.

4.5 CO_2 ADSORPTION O N POLYETHYLENEIMINE FUNCT IONALIZED SILICA

4.5.1 CO_2 adsorption isotherms

The p orous sub strates functionalized following t he polymerization of eth yleneimine under compressed C O_2 are enumerated in the Table 3.6, Chap ter III , sec tion 3.4, which gives the amine loading va lues and the textural pr operties. Figure 4 .15 sho ws the CO_2 adsorption isotherms at 25 ºC for PEI@MCM41 and PEI@CC samples and bare substrates. For the functionalized samples there is an increase in the overall adsorption of CO_2 at 100 kPa higher than 40 % with respect to the bare substrates. Sample 1-PEI@CC in Fig. 4.15b is an exception fo r which adsorption is only enh anced by *ca.* 15 %. For the rest of th e

functionalized samples there is a noticeable adsorption at low pressures evidencing the chemisorption due to the interaction between CO_2 and the amine groups of the polymer.

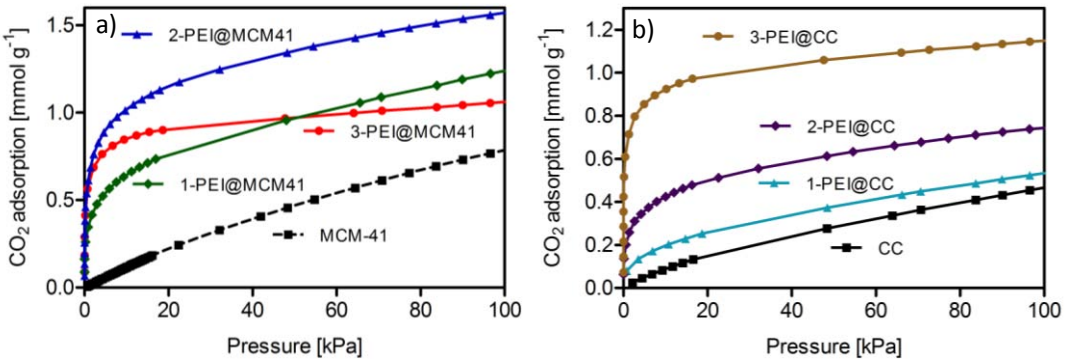

Figure 4.15 CO_2 adsorption isotherms of (a) PEI_{CO2}@MCM41 and (b) PEI_{CO2}@CC substrates at 25 ºC.

Figure 4.15a shows the adsorption isotherms of several PEI@MCM41 samples. Sample 1-PEI@MCM41 with the lowest aminopolymer loading (4.6 mmol g^{-1}) exhibited the lowest adsorption in the chemisorption region. The adsorption is increased for sample 2-PEI@MCM41 with a medium aminopolymer loading of 6 mmol g^{-1}. The situation is different for sample 3-PEI@MCM41, containing 8 mmol g^{-1} of aminopolymer. Sample 3-PEI@MCM41 was expected to present higher CO_2 adsorption than sample 2-PEI@MCM41. However, the isotherm of sample 3-PEI@MCM41 revealed a lower adsorption value. It is also very noticeable the decrease in the slope of the physisorption region. This effect points out the diffusion limitations for CO_2 molecules occurring in samples with high aminopolymer loadings, such as sample 3-PEI@MCM41, which partially block the pores of the substrate hindering the reaction between CO_2 and the amines. Consequently, the adsorption by chemisorption is reduced. Moreover, a reduction in the physisorption induced by pore blocking in the highly loaded sample 3-PEI@MCM41 can be observed by comparison with sample 2-PEI_{CO2}@MCM41. The adsorption isotherms of PEI@CC samples (Fig. 4.15b) show a trend in which the adsorption values increased with the increase of polymer loading. Sample 3-PEI@CC, with the highest aminopolymer loading (4.3 mmol g^{-1}), exhibits the highest CO_2 adsorption value (1.2 mmol g^{-1}). Studied PEI@CC samples presented a similar slope in the

physisorption cure, indicating that the polymer is not blocking the access of CO_2 molecules to the pores

Differences found on the behavior of both studied substrates MCM-41 and CC rely on their pore diameter. Sample 3-PEI@CC, with the highest aminopolymer loading achieved for the CC substrate, do not show pore blocking due to its large pore diameter (8.8 nm). The situation is different for PEI@MCM41 samples, where the pores have only 3.8 nm in diameter and are easily blocked at high aminopolymer loadings, as occurs with sample 3-PEI@MCM41.

4.4.1.1 Effect of the temperature on the adsorption

Figure 4.16a shows the CO_2 adsorption isotherms of high and medium loaded PEI@MCM41 samples at 25 and 75 ºC. Sample 2-PEI@MCM41, containing 6 mmol g^{-1} of aminopolymer, exhibits an overall adsorption of 1.56 mmol g^{-1} at 100 kPa at 25 ºC, which is nearly twice the capacity of the 3-PEI@MCM41 sample (0.89 mmol g^{-1}) with 8 mmol g^{-1} of aminopolymer. Increasing the temperature to 75 ºC resulted in a significant enhancement in the CO_2 adsorption of the highly loaded sample 3-PEI@MCM41 to a value of 1.43 mmol g^{-1}. The opposite behavior was observed for sample 2-PEI@MM41, in which the adsorption capacity was reduced to 0.89 mmol g^{-1} by increasing the temperature. The increase of the temperature is expected to affect CO_2 adsorption in two mutually divergent ways. First, the adsorption capacity is enhanced by increasing polymer mobility and therefore CO_2 diffusivity. Second, adsorption is hindered by shifting the equilibrium of the carbamate formation in the exothermic reaction. For sample 3-PEI@MCM41, with the pores blocked by the polymer, the increase in CO_2 diffusivity with temperature seemed to be the principal effect and, thus, CO_2 adsorption was enhanced by increasing the adsorption temperature. In contrast, for sample 2-PEI@MCM41, CO_2 adsorption diminished with a similar temperature increase, which fundamentally worked against the formation of carbamate molecules.

The effect of the temperature on the CO_2 adsorption was also studied in PEI@CC samples (Fig. 4.16b). For both samples 2- and 3-PEI@CC with medium and high loading

aminopolymer values, the overall CO_2 adsorption decreased when the temperature was increased from 25 to 50 ºC. As shown by the N_2 adsorption isotherms of these samples, there is no pore blocking from the aminopolymer that limits the diffusion of CO_2 molecules. Therefore the increase on the temperature reduces the formation of carbamates, hence, the chemisorption of CO_2.

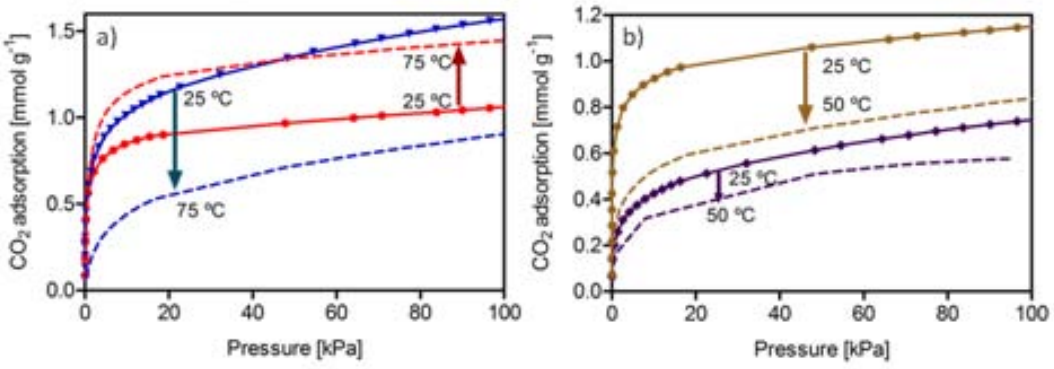

Figure 4.16 CO_2 adsorption isotherms of: (a) PEI@MCM41 and (b) PEI@CC. Isotherms at 25 ºC represented by a continuous line, at 50 and 75 ºC by a dashed line. Colors and symbols same as in Fig. 4.15

4.4.1.2 Differences on the CO_2 adsorption by CC and MCM-41 samples

The amount of aminopolymer loadings on CC and MCM-41 samples, expressed in mmol g^{-1} and in molec nm^{-2} s shown in Table 4.4.

Table 4.4 Amine loadings and textural properties of aminopolymer functionalized MCM-41 and CC substrates.

Sample	[mmol g^{-1}]	ρ_{mgraft} [molecnm^{-2}]	S_a [m^2g^{-1}]	V_p [cm^3g^{-1}]
MCM-41	-	-	1127	0.92
1-PEI@MCM41	4.6	2.5	530	0.40
2-PEI@MCM41	6.0	3.2	306	0.25
3-PEI@MCM41	8.0	4.2	50	0.07
CC	-		440	0.96
1- PEI@CC	3.0	4.1	307	0.70
2- PEI@CC	3.3	4.5	251	0.61
3- PEI@CC	4.3	5.9	234	0.54

Samples 1-PEI@MCM41 and 3-PEI@CC have been chosen for comparison. These samples have similar concentration of the aminopolymer, with values of 4.6 and 4.3 mmol g^{-1}, respectively. However, they have different grafting densities, with values of 2.5 and 4.9 molec nm^{-2}, respectively. Figure 4.17 shows the isotherms for both samples recorded at 25 ºC, together with the ones of the bare substrates MCM-41 and CC. It can be observed that the chemisorption at pressures between 0 and 10 kPa is similar for both samples. The differences in the overall CO_2 adsorption comes out from the physisorption step (pressures above 10 kPa), which for sample 1-PEI@MCM41 is slightly higher than for sample 3-PEI@MCM41. The difference in the adsorption by physisorption is clearly evidenced by the isotherms of bare MCM-41 and CC substrates. As both samples contain similar amounts of aminopolymer in mmol g^{-1} it can be pointed out that the reaction between CO_2 molecules and amine groups from the aminopolymer is independent of the surface area of the substrate, i.e. grafting density (mmol nm^{-2}).

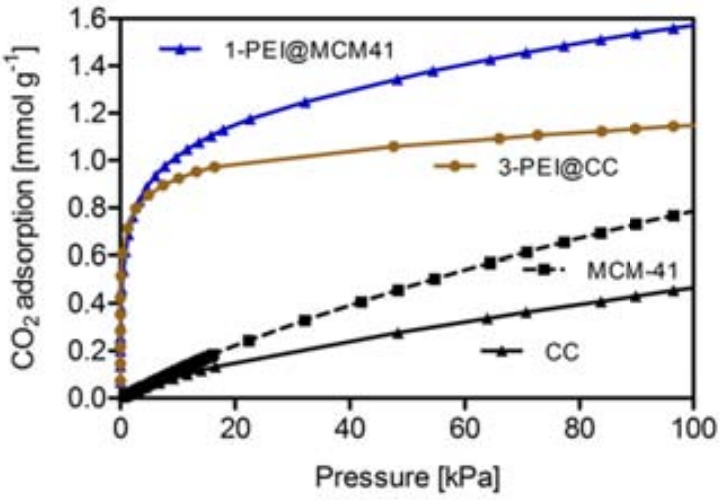

Figure 4 .17 CO_2 adsorption isothe rms of 1-PEI@MCM41 and 3-PEI_{CO2}@CC samples with loadings of 4.6 mmol g^{-1} and 4.3 mmol g^{-1}, respectively.

4.4.2 Cyclic performance and separation from N_2

Data on CO_2 adsorption/desorption up to 10 c ycles were measured and used to determine th e stabili ty of the pr epared aminopolymer pr oducts. Fig. 4.18 sho ws the measured valu es for pristine substrates and fo r some synthesized sa mples. Obtained records revea led that th e performance of th e hybrid products was fairly stable and no significant loss in efficiency was observed for the studied supports.

The beh avior observed fo r sa mples PEI@MCM41(Fig. 4. 18a) showe d was similar to that described in the CO_2 isotherms (Fig. 4.15a). The cyclic adsorption temperature was 45 ºC instead of the 25 ºC used to record the adsorption isotherms, which reduced the overall adsorption va lues. Sample 1 -PEI@MCM41 with the lo west lo ading exhibited th e lowest adsorption. Samples 2- and 3-PEI@MCM41 exhibited similar adsorption values.

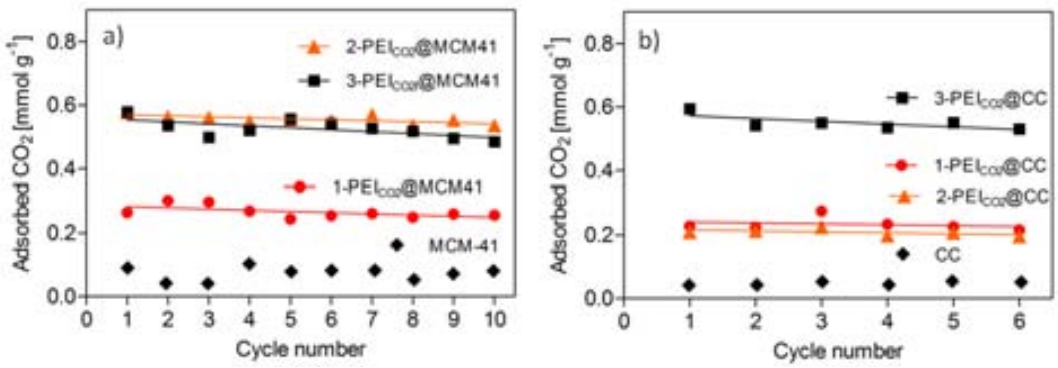

Figure 4.18 CO_2 adsorption cycles for: (a) PEI@MCM41 and (b) PEI@CC samples performed at 45 ºC.

Table 4 .5 provides the adso rption values for the first adsorption/desorption cycle together with the a mine efficiency for each sample. Amine eff iciencies a re lower, in general, than for aminosilane functionalized samples. A feasible explanation is related to the presence of tertiary amines in the PEI polymer, which do not interact with CO_2 at given conditions as primary and secondary amines.

Table 4.5 CO_2 adsorption values obtained from cyclic CO_2/N_2 adsorption process performed at 45 ºC.

Sample	T_{ads} [ºC]	CO_2 ads [mmol g^{-1}]	molar ratio CO_2/amine
MCM-41	45	0.07	-
1-PEI@MCM41	45	0.26	0.06
2-PEI@MCM41	45	0.56	0.09
3-PEI@MCM41	45	0.53	0.07
CC	45	0.04	-
1- PEI@CC	45	0.23	0.08
2- PEI@CC	45	0.21	0.06
3- PEI@CC	45	0.55	0.13

4.4.2.1 CO_2 adsorption and desorption rates

Figure 4.19 shows the CO_2 adsorption and desorption cyclic behavior for some of the functionalized MCM -41 and CC sub strates. The data was smoothed by fi tting it to empirical correlations, similar to the curves shown in Fig. 4.13. The cyclic profiles were

also divided in three different steps: fast adsorption occurring in empty adsorbents, slow adsorption occurring close to adsorption equilibrium and desorption. Slopes of the three different steps were calculated for the samples of interest and denoted as s_1, s_2, and s_3.

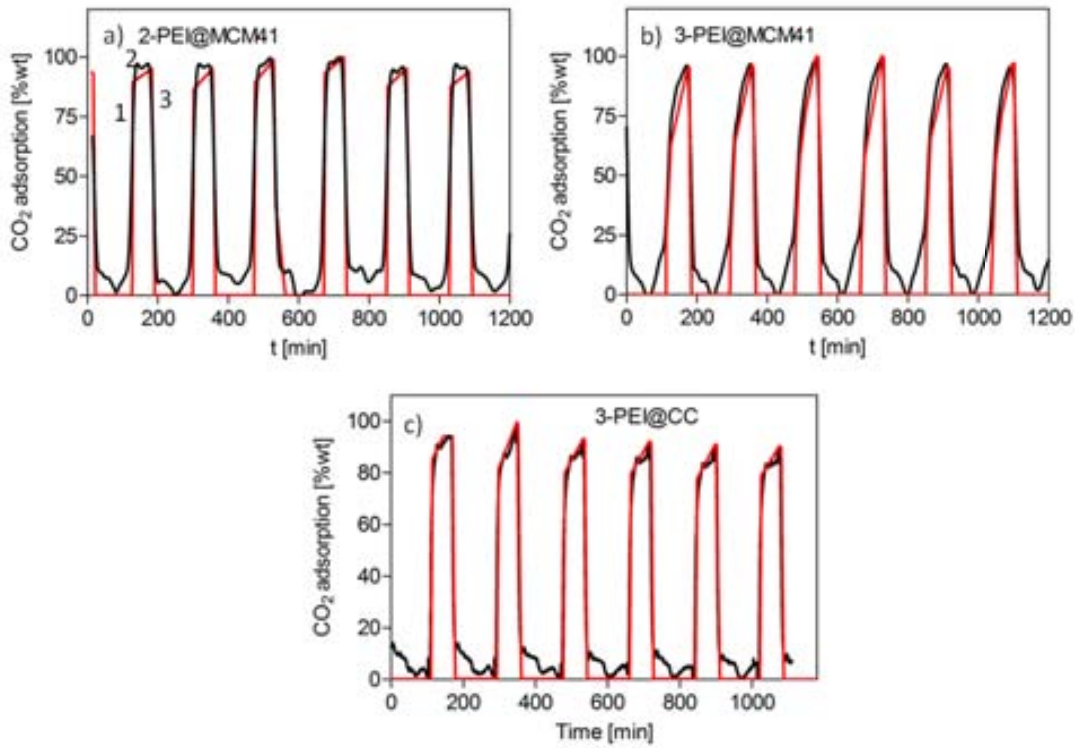

Figure 4 .19 Cyclic behavior of representative synthesized materials: (a) 2-PEI@MCM41, (b) 3-PEI@MCM41, and (c) 3-PEI@CC samples. The black lines correspond to the original recorded curves, while the red straight lines are the fitted profiles. Numbers indicate the CO_2 fast (1) and slow (2) adsorption and desorption (3) steps.

The influence of the PEI loading in the adsorption and desorption rates is shown in Fig. 4.20a,b for samples PEI@MCM41 and PEI@CC, respectively. The adsorption rate in the empty hybrid adsorbents increased with the amine loading for both type of porous substrates. Figure 4 .20a compares the adsorption and desorption for samples 2 -PEI@MCM41 and 3-PEI@MCM41, with loadings of 6 and 8 mmol g^{-1} of aminopolymer, respectively. It can be observed that, under similar experimental conditions, the adsorption rate in the fast adsorption region for sample 2-PEI@MCM41 was more than two times higher than for sample 3-PEI@MCM41, as shown by comparing the s_1 slopes. The reason

of this behavior is linked to the CO_2 diffusion limitations occurring in the highly loaded sample 3-PEI@MCM41. Contrarily, the s_2 slopes, corresponding to the adsorption rate in the second step, was four times higher for sample 3-PEI_{CO2}@MCM41 than for sample 2-PEI_{CO2}@MCM41, which exhibited an almost null adsorption. As shown in Fig. 4.20a, sample 2-PEI@MCM41, with a lower amount of aminopolymer than sample 3-PEI@MCM41,adsorbed higher amounts of CO_2 in a faster way than sample 2-PEI@MCM41. Contrarily, the s_2 slopes, corresponding to the adsorption rate in the second step, was four times higher for sample 3-PEI@MCM41 than for sample 2-PEI@MCM41, which exhibited an almost null adsorption. After the fast adsorption step, sample 2-PEI@MCM41 exhibited an almost null adsorption. Sample 3-PEI@CC in Fig. 4.20b showed a high adsorption rate in the fast adsorption region, even higher than MCM-41 samples. The following regions have slopes similar to sample 2-PEI@MCM.

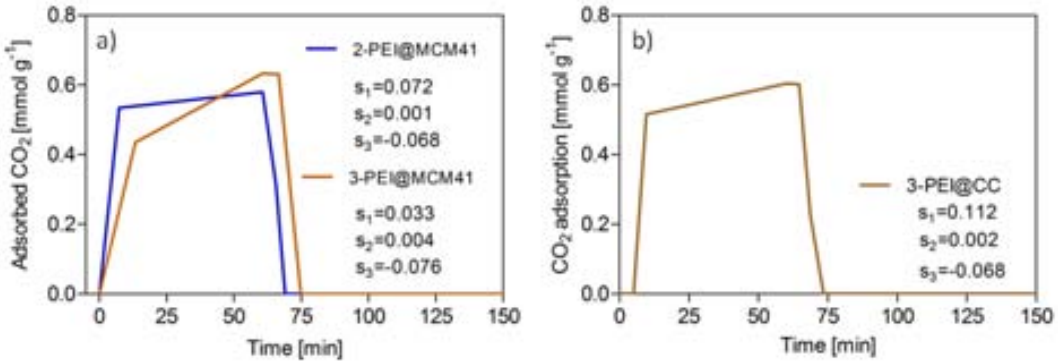

Figure 4.20 Comparison of the adsorption/desorption profiles of samples prepared or measured under different experimental conditions: (a) PEI@MCM41 and (b) PEI@CC products with different loadings at 45 ºC. Slopes s_1, s_2 and s_3 are given in mmol g^{-1} min^{-1}.

4.4.2.2 Comparison to literature data

The CO_2 adsorption capacity of the materials prepared in this thesis was compared with published adsorption data for loaded PEI substrates synthesized using the organic-liquid approach [38, 39] and the chemical vapor deposition [40] (Table 4.6). Samples from the literature were selected with a wide range of PEI loading values between 2 and 15 mmol g^{-}

[1]. However, in some samples these values have not been reported and are estimated from the amount of PEI used for the synthesis. Values of CO_2 adsorption from gas mixtures at temperatures in the range of 25 to 45 ºC are found to be between *ca.*0.11 and 0.70 mmol g^{-1}.

The adsorption under pure CO_2 at atmospheric pressure was between *ca.*0.44 and 2.5 mmol g^{-1}. The wide range of these values is due to the differences in sample loadings and the adsorption temperature.

The adsorption value of pure CO_2 at 100 kPa at 75 ºC of the sample 3-PEI@MCM41 was 1.45 mmol g^{-1}, which is comparable to the value for the sample MCM-41-PEI-30 from ref. [39], 1.56 mmol g^{-1}, with a similar PEI loading. The comparison of our samples with the literature for cyclic gas mixture adsorption at 40-45 ºC revealed that samples 2- and 3-PEI@MCM41 have an adsorption two times higher than samples from ref. [38].

Table 4.6 CO_2 adsorption data compiled from the literature for products involving PEI loaded into diverse porous supports.

Substrate	Sample	ρ_N[1] [mmol g^{-1}]	Pure CO_2[2]@100 kPa@T_{ads} [mmol g^{-1}]@[ºC]	Gas mixture[3]@T_{ads} [mmol g^{-1}]@[ºC]	Ref
MCM-41	1-PEI@MCM41	4.6	1.5@25ºC 0.91@75ºC	-	This work
	2-PEI@MCM41	6	1.2@25ºC 0.58@50ºC	0.57@45ºC	This work
	3-PEI@MCM41	8	1.0@25ºC 1.34@50ºC 1.45@75ºC	0.57@45ºC	This work
MCM-41	MCM-41-PEI-15	~3.5	0.44@75ºC	-	[39]
	MCM-41-PEI-30	~7	1.56@75ºC	-	
	MCM-41-PEI-50	~11.5	2.5@75ºC 1.0@50ºC	-	
MCM-41	MCM-41-PEI-10	~2.3	-	0.11@45ºC	[38]
	MCM-41-PEI-40	~9.3	-	0.22@40ºC	
	MCM-41-PEI-60	~14	-	0.20@40ºC	
SBA-15	S-70C-4-24h	9.7	-	0.43@25ºC	[40]
	AS-50C-4-24h	7.5	-	0.70@25ºC	
	S-70C-1-24h	6.2	-	0.69@25ºC	

[1]PEI loading values from TGA and EA. Refs. and [39] do not report this values.[2]Values of pure CO_2 adsorption obtained from isotherms (this work) and TGA measurements. [3]CO_2 atmospheric adsorption form a mixture of 10-15 v% of CO_2 in N_2/Ar

4.6 COMPARISON OF THE CO_2 ADSORPTION BETWEEN THE AMINOPOLYMER AND AMINOSILANE SAMPLES

The adsorption of CO_2 by the aminopolymer is fundamentally different to that of MAP aminosilane. For the aminosilane, the carbamate formation is not possible if amine groups are not close enough, hence being the adsorption closely related to the density of amines per surface area. This was discussed in section 4.3.1 for low loading SG_{40} and MCM-41 samples and in section 4.3.2, where simulations showed the minimum distance of two nitrogen molecules to interact with a CO_2 molecule. The adsorption of PEI samples is different as the polymer plays the role of a network where amines are close enough to

interact with CO_2 even at low densities. The adsorption is dependent on the amount of polymer per gram of substrate.

4.6.1 Relationship between the adsorption of N_2 and CO_2 from aminosilane and aminopolymer samples

In this section, a comparison of the N_2 and CO_2 adsorption results for the MAP and PEI materials used in this study is established. The relationship between the adsorption results with N_2 and CO_2 allows us to compare the potential applications of the materials in CO_2 adsorption and separation processes. Materials with a high preference for CO_2 adsorption are more likely to perform well for these processes. Such a relationship can be established by correlating the N_2 adsorption at a given pressure with the CO_2 adsorption at a different pressure. A similar comparison was made by Yang *et al.* [41] for H_2 adsorption at -196 ºC and 25 ºC.

For the samples prepared and simulated in this work, the N_2 adsorption at -196 ºC and 1.0 kPa (relative to saturation pressure, P^{sat}, P/P^{sat} = 0.01) as a function of the CO_2 adsorption at 25 ºC and 70 kPa (P/P^{sat} = 0.01) is plotted in Fig. 4.21. In this representation, the materials with no significant CO_2 chemisorption, which are either the pristine substrates or the products with low MAP loadings, follow a clear trend line, depicted as a dotted line. The trend line also shows that the models are an accurate representation of the experimental materials. In all the MCM-41 and SG_{40} studied samples, the symbols representing the models give similar results and follow the same trend than the experimental materials. Only the raw silica gel has a slightly higher preference for CO_2 adsorption than predicted. The functionalization of SG_{40} samples with MAP does not significantly change the amount of either N_2 or CO_2. MAP@MCM41 samples with low amine loadings decrease both the N_2 and the CO_2 adsorption. Materials with higher MAP show a high preference for CO_2 over N_2 adsorption: the reduction in the N_2 adsorption is below 4 mmol g^{-1} and the increase on the CO_2 adsorption is up to *ca.* 1.3 mmol g^{-1} and as high as 2.0 mmol g^{-1}. The loading of MAP into CC is shown for one of the samples which reduces the adsorbed N_2 up to *ca.* 0.5 mmol g^{-1} and increases the CO_2 adsorption to 1.1 mmol g^{-1}. For PEI@MCM41 samples the decrease in the N_2 adsorption goes from 4 mmol g^{-1} to almost null adsorption. The CO_2 adsorption enhancement is between 1-1.4 mmol g^{-1}.

PEI@MCM41 samples exhibiting the lowest N_2 adsorption values also show the lowest CO_2 adsorption due to the diffusion restrictions for CO_2 molecules occurring at 25 ºC. For PEI@CC samples the decrease in the N_2 adsorption is similar to PEI@MCM41 samples although the increase in the CO_2 adsorption is more moderate. Values for the CO_2 adsorption are found in the range of 0.4 to 1.1 mmol g^{-1}.

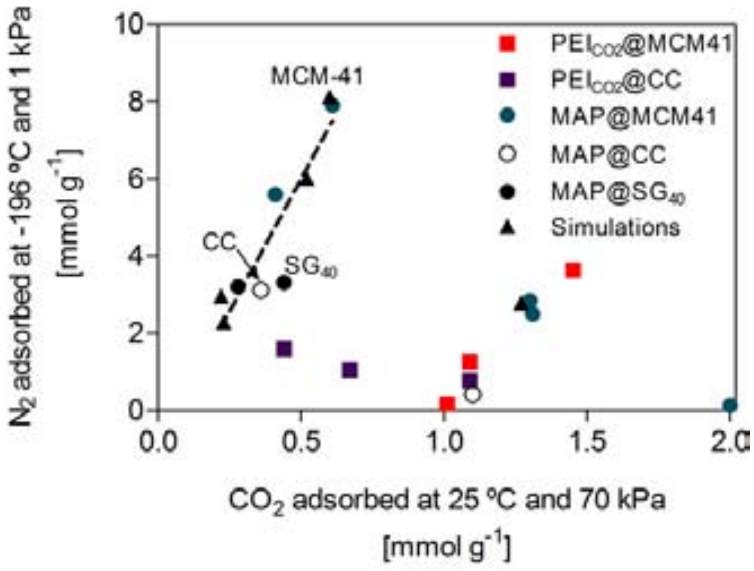

Figure 4.21 N_2 storage capacity at -196 ºC and 1 kPa as a function of the CO_2 storage capacity at 25 ºC and 70 kPa for experimental MAP and PEI@Substrate experimental samples and molecular simulations.

4.6.2 Overall CO_2 adsorption

Figure 4.22 summarizes the CO_2 adsorption values obtained from the isotherms at 10 kPa and at various temperatures (25, 50 and 75 ºC). Samples from each substrate are shown consecutively according to their MAP or PEI loading value (low, medium and high). The figure evidences the enhancement on the adsorption by samples loaded with different amounts of both MAP and PEI with respect to their bare substrates. MAP@SG_{40} is an exception for which MAP loading decreased its CO_2 adsorption. Sample 10-MAP@MCM41 exhibits the highest CO_2 adsorption at 25 ºC in comparison to the rest of the products. The substrate CC with high MAP and PEI loadings of 3.1 and 4.3 mmol g^{-1},

respectively, showed very similar adsorption values of *ca.* 1.0 mmol g^{-1}. For the high loaded PEI sample, the adsorption decreases with the temperature to values *ca.* 0.5 mmol g^{-1}. The MCM-41 substrate loaded with medium values of MAP (1.56 mmol g^{-1}) and PEI (6 mmol g^{-1}) showed similar adsorption values of *ca.*0.8-1.0 mmol g^{-1} at 25 °C. The sample with the highest PEI loading showed an increase in the CO_2 adsorption with the temperature from *ca.* 0.8 to *ca.* 1.4 mmol g^{-1}.

Comparing CC and MCM-41 substrates, in general MCM-41 gives higher CO_2 adsorption values. However, high loaded PEI and MAP in the CC substrate shows relevant CO_2 adsorption at 25 °C which is comparable to the adsorption of PEI@MCM41 products and to medium loaded MAP@MCM41.

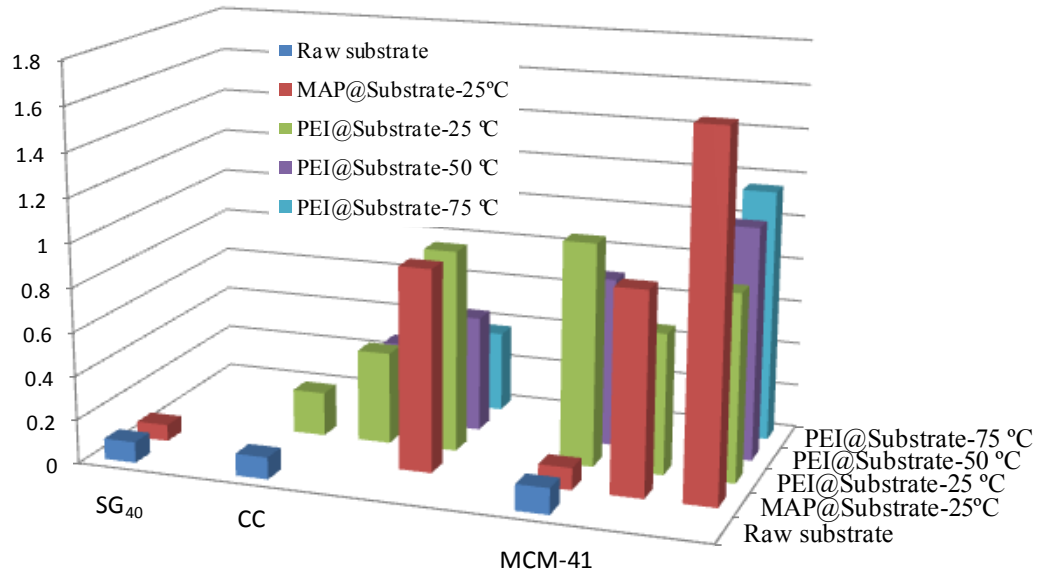

Figure 4.22 Values for the CO_2 adsorption of SG_{40}, CC and MCM-41 samples functionalized with MAP and PEI_{CO2}. Loading MAP and PEI values increase from left to the right for each sample. Values for adsorption are taken from the CO_2 adsorption isotherms at 10 kPa and at 25 ºC. Adsorption values at 50 and 75 ºC are shown for some of the PEI_{CO2} loaded samples.

4.7 CONCLUSIONS

The adsorption properties of the supercritically synthesized sorbents were evaluated in this chapter. For the hydrophobic alkylsilane modified samples the percentage of water uptake was considerably reduced only for mesoporous samples after silanization (*ca.* 50%). The hydrophilicity of the materials was reduced after silanization, but not completely hydrophobic materials were obtained.

The CO_2 adsorption properties of the porous systems modified with amines were evaluated by means of pure CO_2 adsorption isotherms, adsorption/desorption cycles under gas mixtures and with the aid of molecular simulations. For samples SG_{40} and MCM-41 with MAP loadings of less than 1 mmol/g, the adsorption results suggested that carbamates were unable to form and the adsorption occurred *via* physisorption, giving CO_2 adsorption values similar to the ones found for their respective pristine supports. The chemisorption effect was evident only for samples with functionalization degrees of 2 mmol/g. For MAP functionalized MCM-41 and CC substrates the CO_2 adsorption values were in line with the values in the literature. The highest efficiency values for MAP samples were measured for the medium loaded samples 11-MAP@MCM41 and 12-MAP@MCM41 at 25 ºC, and were in the order of 0.4-0.5. Although the efficiency of the reaction is an important factor for optimizing the amount of amine employed for gas separation, this value has to be combined with the total CO_2 adsorption capacity, which indicates the amount of solid material required for the separation. In this context, the supercritically synthesized materials have great potential for industrial use due to their combined high amine loading and above average efficiency of the reaction. Moreover, synthesized hybrid sorbents had a high thermal stability. The performance of the hybrid MAP products was very stable in regard of the CO_2 adsorption capacity after 10 adsorption/desorption cycles.

Simulated and experimental adsorption results for aminosilane functionalized MCM-41 and SG-40 substrates were compared. The phenomenon of chemisorption, occurring only for porous materials with high amine density, was corroborated by molecular simulations, where a distance between amine chains similar to the molecular size of CO_2 was found for the materials with a considerable effect of chemisorption. The proximity of neighbor amine chains is essential to obtain materials with high potential for CO_2 adsorption and separation.

Understanding the adsorption mechanism would help to optimize these materials for maximum economic and environmental benefits. Molecular simulations complemented the experimental work provided an adequate insight of the adsorption behavior of the materials and allowing differentiating between physisorbed and chemisorbed CO_2.

The CO_2 adsorption studied on PEI functionalized supports showed the strong dependence between the aminopolymer density and the temperature at which the CO_2 adsorption is performed. It was established that diffusion of CO_2 molecules on samples with high aminopolymer loadings of 8 mmol g^{-1} was enhanced with the temperature and consequently the overall adsorption. However, chemisorption decreased with the increase of the temperature, diminishing the overall adsorption in the medium and low loaded samples. High adsorption values up to 1.5 mmol g^{-1} and 1.0 mmol g^{-1} were found for PEI@MCM41 and PEI@CC samples at 25 ºC, respectively.

4.8 REFERENCES

1. S.C. Reyes, J.H. Sinfelt, and G.J. Demartin, *Diffusion in Porous Solids: The Parallel Contribution of Gas and Surface Diffusion Processes in Pores Extending from the Mesoporous Region into the Microporous Region.* The Journal of Physical Chemistry B, 2000, 104(24), 5750.
2. S. Lowell and J.E. Shields, *Powder Surface Area and Porosity*1979USA: Powder Technology Series.
3. R.L. Burwell Jr, *SECTION 1 - DEFINITIONS AND TERMINOLOGY*, in *Manual of Symbols and Terminology for Physicochemical Quantities and Units–Appendix II*, R.L. Burwell, Editor,1976, Pergamon. p. 74.
4. P.J.E. Harlick and F.H. Tezel, *An experimental adsorbent screening study for CO2 removal from N2.* Microporous and Mesoporous Materials, 2004, 76(1–3), 71.
5. P. Bankovic, N.R. Demarquette, and M.L.P. Da Silva, *Obtention of selective membranes for water and hydrophobic liquids by plasma enhanced chemical vapor deposition on porous substrates.* Materials Science and Engineering B: Solid-State Materials for Advanced Technology, 2004, 112(2-3 SPEC. ISS.), 165.
6. E.-P. Ng and S. Mintova, *Nanoporous materials with enhanced hydrophilicity and high water sorption capacity.* Microporous and Mesoporous Materials, 2008, 114(1–3), 1.
7. H.J. Herbert and H.C. Moog, *Cation exchange, interlayer spacing, and water content of MX-80 bentonite in high molar saline solutions.* Engineering Geology, 1999, 54(1–2), 55.
8. P.B.R. Schlink, *Water Determination by Karl Fischer Tritation*, ed. Metrohm2006.
9. P. López-Aranguren, S. Builes, J. Fraile, L.F. Vega, and C. Domingo, *Understanding the performance of new amine-functionalized mesoporous silica materials for CO2 adsorption.* Environmental Science and Technology, 2014, Submitted for publication.
10. S. Builes and L.F. Vega, *Understanding CO 2 capture in amine-functionalized MCM-41 by molecular simulation.* Journal of Physical Chemistry C, 2012, 116(4), 3017.
11. K.B. Lee, M.G. Beaver, H.S. Caram, and S. Sircar, *Reversible chemisorbents for carbon dioxide and their potential applications.* Industrial and Engineering Chemistry Research, 2008, 47(21), 8048.
12. M. Selva, P. Tundo, and A. Perosa, *The synthesis of alkyl carbamates from primary aliphatic amines and dialkyl carbonates in supercritical carbon dioxide.* Tetrahedron Letters, 2002, 43(7), 1217.
13. R. Serna-Guerrero, E. Da'na, and A. Sayari, *New insights into the interactions of CO2 with amine-functionalized silica.* Industrial and Engineering Chemistry Research, 2008, 47(23), 9406.
14. R.S. Franchi, P.J.E. Harlick, and A. Sayari, *Applications of pore-expanded mesoporous silica. 2. Development of a high-capacity, water-tolerant adsorbent for CO2.* Industrial and Engineering Chemistry Research, 2005, 44(21), 8007.
15. N. Hiyoshi, K. Yogo, and T. Yashima, *Adsorption characteristics of carbon dioxide on organically functionalized SBA-15.* Microporous and Mesoporous Materials, 2005, 84(1-3), 357.
16. O. Leal, C. Bolívar, C. Ovalles, J.J. García, and Y. Espidel, *Reversible adsorption of carbon dioxide on amine surface-bonded silica gel.* Inorganica Chimica Acta, 1995, 240(1-2), 183.

17. G.P. Knowles, S.W. Delaney, and A.L. Chaffee, *Diethylenetriamine[propyl(silyl)]-Functionalized (DT) Mesoporous Silicas as CO_2 Adsorbents.* Industrial & Engineering Chemistry Research, 2006, 45(8), 2626.
18. Y.G. Ko, H.J. Lee, H.C. Oh, and U.S. Choi, *Amines immobilized double-walled silica nanotubes for CO2 capture.* Journal of Hazardous Materials, 2013, 250-251, 53.
19. R.J. Littel, G.F. Versteeg, and W.P.M. Van Swaaij, *Kinetics of CO2 with primary and secondary amines in aqueous solutions-II. Influence of temperature on zwitterion formation and deprotonation rates.* Chemical Engineering Science, 1992, 47(8), 2037.
20. X. Xu, C. Song, J.M. Andresen, B.G. Miller, and A.W. Scaroni, *Novel polyethylenimine-modified mesoporous molecular sieve of MCM-41 type as high-capacity adsorbent for CO2 capture.* Energy and Fuels, 2002, 16(6), 1463.
21. S. Kim, J. Ida, V.V. Guliants, and J.Y.S. Lin, *Tailoring pore properties of MCM-48 silica for selective adsorption of CO 2.* Journal of Physical Chemistry B, 2005, 109(13), 6287.
22. O.G. Nik, B. Nohair, and S. Kaliaguine, *Aminosilanes grafting on FAU/EMT zeolite: Effect on CO_2 adsorptive properties.* Microporous and Mesoporous Materials, 2011, 143(1), 221.
23. S. Choi, J.H. Drese, and C.W. Jones, *Adsorbent materials for carbon dioxide capture from large anthropogenic point sources.* ChemSusChem, 2009, 2(9), 796.
24. P. López-Aranguren, J. Fraile, L.F. Vega, and C. Domingo, *Regenerable solid CO_2 sorbents prepared by supercritical grafting of aminoalkoxysilane onto low-cost mesoporous silica.* Journal of Supercritical Fluids, 2013, Accepted
25. G.P. Knowles, J.V. Graham, S.W. Delaney, and A.L. Chaffee, *Aminopropyl-functionalized mesoporous silicas as CO2 adsorbents.* Fuel Processing Technology, 2005, 86(14-15), 1435.
26. H.Y. Huang, R.T. Yang, D. Chinn, and C.L. Munson, *Amine-Grafted MCM-48 and Silica Xerogel as Superior Sorbents for Acidic Gas Removal from Natural Gas.* Industrial & Engineering Chemistry Research, 2002, 42(12), 2427.
27. Z.N. Bacsik, R. Atluri, A.E. Garcia-Bennett, and N. Hedin, *Temperature-Induced Uptake of CO2 and Formation of Carbamates in Mesocaged Silica Modified with n-Propylamines.* Langmuir, 2010, 26(12), 10013.
28. B. Aziz, G. Zhao, and N. Hedin, *Carbon Dioxide Sorbents with Propylamine Groups−Silica Functionalized with a Fractional Factorial Design Approach.* Langmuir, 2011, 27(7), 3822.
29. O. Leal, C. Bolívar, C. Ovalles, J.J. García, and Y. Espidel, *Reversible adsorption of carbon dioxide on amine surface-bonded silica gel.* Inorganica Chimica Acta, 1995, 240(1–2), 183.
30. K. Wörmeyer, M. Alnaief, and I. Smirnova, *Amino functionalised Silica-Aerogels for CO_2-adsorption at low partial pressure.* Adsorption, 2012, 18(3-4), 163.
31. V. Zelenak, D. Halamova, L. Gaberova, E. Bloch, and P. Llewellyn, *Amine-modified SBA-12 mesoporous silica for carbon dioxide capture: Effect of amine basicity on sorption properties.* Microporous and Mesoporous Materials, 2008, 116(1–3), 358.

32. M.R. Mello, D. Phanon, G.Q. Silveira, P.L. Llewellyn, and C.M. Ronconi, *Amine-modified MCM-41 mesoporous silica for carbon dioxide capture.* Microporous and Mesoporous Materials, 2011, 143(1), 174.

33. F.Y. Chang, K.J. Chao, H.H. Cheng, and C.S. Tan, *Adsorption of CO2 onto amine-grafted mesoporous silicas.* Separation and Purification Technology, 2009, 70(1), 87.

34. N. Hiyoshi, K. Yogo, and T. Yashima, *Adsorption of carbon dioxide on amine modified SBA-15 in the presence of water vapor.* Chemistry Letters, 2004, 33(5), 510.

35. E.F. Da Silva and H.F. Svendsen, *Ab Initio Study of the Reaction of Carbamate Formation from CO2 and Alkanolamines.* Industrial & Engineering Chemistry Research, 2004, 43(13), 3413.

36. D.B. Dell'amico, F. Calderazzo, L. Labella, F. Marchetti, and G. Pampaloni, *Converting Carbon Dioxide into Carbamato Derivatives†.* Chemical Reviews, 2003, 103(10), 3857.

37. R. Serna-Guerrero, Y. Belmabkhout, and A. Sayari, *Modeling CO2 adsorption on amine-functionalized mesoporous silica: 1. A semi-empirical equilibrium model.* Chemical Engineering Journal, 2010, 161(1–2), 173.

38. M.U. Thi Le, S.-Y. Lee, and S.-J. Park, *Preparation and characterization of PEI-loaded MCM-41 for CO2 capture.* International Journal of Hydrogen Energy, 2014, 39(23), 12340.

39. X. Xu, C. Song, J.M. Andresen, B.G. Miller, and A.W. Scaroni, *Novel Polyethylenimine-Modified Mesoporous Molecular Sieve of MCM-41 Type as High-Capacity Adsorbent for CO2 Capture.* Energy & Fuels, 2002, 16(6), 1463.

40. W. Chaikittisilp, S.A. Didas, H.-J. Kim, and C.W. Jones, *Vapor-Phase Transport as A Novel Route to Hyperbranched Polyamine-Oxide Hybrid Materials.* Chemistry of Materials, 2013, 25(4), 613.

41. S.J. Yang, J.H. Im, H. Nishihara, H. Jung, K. Lee, T. Kyotani, and C.R. Park, *General Relationship between Hydrogen Adsorption Capacities at 77 and 298 K and Pore Characteristics of the Porous Adsorbents.* The Journal of Physical Chemistry C, 2012, 116(19), 10529.

CHAPTER V

GENERAL CONCLUSIONS AND FUTURE WORK

1. $ScCO_2$ is a convenient technology for the functionalization with organic molecules of meso- and microporous materials. The characteristics properties of $scCO_2$, such as the tunable density, the high diffusivity and the null surface tension, were advantageous for technology development. Processes were performed at low temperatures (45-130 ºC) and pressures (6-20 MPa) during short processing times (10-300 min). The innovative components of this work rely not only on the improved characteristics of the processing method, but also on the superior characteristics of the obtained products, particularly those related to thermal stability.

2. The $scCO_2$ technology is particularly adequated for the functionalization with silanes, including alkyl- (octyltriethoxysilane) and amino- (methylamino)propyltrimethoxysilane) silanes, yielding high grafting densities (0.5-5.4 mmol g^{-1}). In the particular case of aminosilanes, it was demonstrated that by controlling the operating conditions of pressure and temperature the formation of carbamates by reaction between the amine and the CO_2 can be avoided, thus, attaining enough solubility of the aminosilane in $scCO_2$ to successfully perform the supercritical functionalization.

3. A new procedure was described to produce hyperbranched PEI by the ring-opening polymerization of aziridine using compressed CO_2 simultaneously as the solvent and the catalyst. An exceptionally fast method, with processing times in the order of minutes, was designed, giving remarkably high amine contents (3-8 mmol g^{-1}).

4. Porous sílica modified with alkylsilanes showed increased hydrophobicity with respect to bare materials, although not completely hydrophobic products were obtained. The functionalized materials were used to validate atomistic models for amorphous porous silica created in the framework of this thesis. Further, quantitative predictions of the adsorption were obtained using grand canonical Monte Carlo. This work demonstrates that even though the models of amorphous hybrid materials require simplifications related to the cell size and silane polymerization modes, it is possible to use these models to obtain an adequate insight of what happens in the macroscopic systems. The simulation method

for the covalent functionalization of silica gel described in this work was found to be more realistic than the models found in the literature.

6. The amine modified products had an outstanding CO_2 adsorption capacity at very low pressures (5-10 kPa), hence, indicating a chemisorption phenomenon, contrarialy to bare materials that only present physisorption. The phenomenon of chemisorption, occurring only for porous materials with an amine density higher than 2 mmol g^{-1}, was corroborated by molecular simulations, where a minimum distance between amine chains was calculated for significant CO_2 adsorption and shown to be similar to the size of the CO_2 molecule.

7. The supercritically synthesized aminosilane and PEI materials have great potential for industrial use in the adsorption of CO_2, essentially due to the combined characteristics of high amine loading and above average efficiency of the reaction. The performance of the hybrid products was very stable in regard of the CO_2 cyclic adsorption/desorption behaviour.

8. The PEI modified silica exhibited a higher density of amino groups than the aminosilane modified silica. However, the efficiencies were approximately four times lower for PEI than for aminosilane products, due to the presence of tertiary amines in the PEI polymer. Tertiary amines do not participate on the chemisorption process, as primary and secondary amines do.

9. The potential for the adsorption and separation of CO_2 exhibited by the aminosilica products studied in this work shows a promising route for developing materials that can contribute towards the mitigation of anthropogenic emissions by CO_2 sequestration.

Further investigation on the scale-up of the supercritical functionalization of mesoporous silica and other porous matrices with alkylsilanes and amino functional groups will be necessary for the implementation of the process in a larger scale. Preliminary results have shown that the ring-open polymerization of aziridine in compressed CO2 can be carried out at low pressures (2-4 MPa) and ambient temperatures. Hence, it would be useful to study the optimization of the processes at these mild conditions in order to reduce the process costs. Open lines of research related to the topic of this thesis are the preparation of other complex hybrid materials using supercritical CO_2. The large catalogue of silane molecules with a broad range of functional groups opens the possibility of engineering porous functional materials fitting the requirements of many industrial applications (catalysts, biomedical devices, drug carriers, gas sensors, etc.).